Atomistic model of magnetisation dynamics and equilibrium properties of magnetic tunnel junctions

Andrea Meo

PhD

University of York

Physics

September 2018

Abstract

The next generation of portable devices requires random access memories (RAMs) which are characterised by high performance and at the same time low power consumption. A promising candidate as replacement in this sector is magnetic RAM (MRAM) based on CoFeB/MgO magnetic tunnel junctions, since it retains the fast operational capability while reducing the energy requirements due to its non-volatile nature. Despite such outstanding features, a complete understanding of the device operation has not been achieved yet. This limits the scaling of the device below the next technological node ($< 20\,\text{nm}$). The reduction in the number of atoms constituting these devices is responsible for surface and finite size effects as well as a reduced thermal stability, which affects the dynamic properties. Currently, micromagnetism represents the most used theoretical approach to investigate magnetic materials and their properties. The main limitation of this model is the continuum approach. In this approximation the atomic properties are averaged, which makes it unsuitable to describe interface, surface and finite size effects as well as thermal effects. Do deal with these limitations, in this thesis we use an atomistic spin model to investigate the equilibrium and dynamical properties of CoFeB/MgO-based systems, an approach more appropriate to account for such effects. Our results suggest that CoFeB/MgO systems are characterised by more complex magnetic properties than usually assumed. The reversal mechanism is non-uniform at dimensions and temperatures that are technologically relevant. Moreover, at these time scales thermal effects cause a distribution of the dynamic properties that represent an intrinsic limitation to the device reliability and need to be addressed in order to achieve the desired scaling. The results also show the importance of atomistic models to understand and accurately describe the magnetic properties of devices when they are fabricated on the nano scale.

Table of contents

List of figures

List of tables

Acknowledgements

I would like to thank my supervisors Prof. Roy Chantrell and Dr. Richard Evans without whom this thesis would not have been possible. I would also like to express my gratitude for the many opportunities they gave me and for the never-ending guidance and support throughout all the PhD.

I would like to thank my collaborators Ramón Cuadrado, László Szunyogh, Phanwadee Chureemart, Jessada Chureemart, Pieter Visscher, Oksana Chubykalo-Fesenko, Sue Wang, Roman Chepulskyy and Dmytro Apalkov for the fruitful discussions and guidance.

I would like to thank my friends and colleagues in York Sergiu, Sam, Marta, Zwuei, Cristina, Mara, Natty, Tong, Sarah, David, Oscar, Matt, Tom, Razvan, Roberto, Ewan, Daniel, Akiko, just to name a few of them, for the useful discussions and for the amazing time I had during the PhD.

I would like to thank my brother Sergio and my friends Silvia, Rachele and Simona for their continued friendship and support. A special thanks goes to my family and in particular to my parents, who always believed in me and supported me in all these years.

Declaration

In addition to the individual work of the author, this thesis contains the results of a number of collaborators: the *ab initio* results presented in Chapter 8 have been obtained by R. Cuadrado and L. Szunyogh.

All other work is the original work of the author except where explicitly indicated. All sources are acknowledged as References. This work has not previously been presented for an award at this, or any other, University. Much of the work has been publicly presented by the author and the results presented in Chapter 5 are published in the following article: A. Meo *et al.* "Thermally nucleated magnetic reversal in CoFeB/MgO nanodots" , Scientific Reports 7, 16729 (2017).

Chapter 1

Introduction

1.1 Motivation

In this time dominated by high performance devices and portable devices such as smart phones, tablet computers and mobile gadgets, requirements for high density and low power consumption memories are a driving force for the storage and memory fields. Current silicon-based technology is facing its physical scaling limits and alternative technologies are intensely under research[1–3]. Spin transfer torque magnetic random access memories (STT MRAMs) are one of the most promising candidates. Due to the potential high density, low power consumption, fast read and write operations, infinite endurance and resistance to electromagnetic disturbances, STT MRAMs have been proposed as universal memories [1–3] and the production of STT MRAM devices was launched in 2016.

Despite the huge potential demonstrated by STT MRAMs, improvements in the power consumption and storage are necessary for this technology to find space in the memory market and supplant semiconductor-based competitors. These improvements are possible only if a total understanding of the underlying physics is achieved. Analytic models and computational approaches are often employed to aid research both by providing a basic theory to explain more complex phenomena and by guiding experiments. Micromagnetism, that is the most used approach to model magnetic materials and their properties, is unsuitable for the investigation of such systems due to the small dimensions and the complexity of the magnetic properties of these devices, finite size and thermal effects. Therefore, we characterise the magnetic properties and the switching dynamics of magnetic tunnel junctions, the main components of MRAMs, by means of an atomistic model.

1.2 Magnetic random access memory (MRAM)

A random access memory (RAM) is a device used for data storage and its performances have to abide by certain requirements in order to be produced and commercialised. These are scalability of the dimensions of the device, high data density storage, low power consumption, fast switching and retention of the information and stability. The most common RAM are the static RAM (SRAM) and dynamic RAM (DRAM). They differ for the architecture: transistors are used in SRAMs, while a capacitor coupled to a transistor are employed in DRAMs. SRAMs are faster and relatively lower power consumption, but with the drawback of lower storage density, larger cell size and a higher cost than DRAM. As a consequence, the latter is the most used as computer memory device, while SRAM finds its employment in the central processing units (CPU). Both SRAM and DRAM are volatile as the data is not retained after the power supply is removed. Moreover, DRAMs need to be continuously refreshed as the information is lost as the capacitor discharges. Volatility causes SRAM and DRAM to suffer from high power consumption in addition to the issues mentioned previously. There is also another type of RAM: flash memory. Flash memory is a inexpensive non-volatile technology that is sensibly slower than both the DRAM and SRAM and, like these, suffers of high power requirements.

These silicon-based technologies are approaching their physical scaling limits [1, 4] and the research of alternatives that allow to achieve larger density, smaller dimensions and lower power consumption has been intensively pursued. A promising candidate, alongside resistive RAM (ReRAM) and phase-change RAM (PCRAM), is magnetic random access memory (MRAM). A MRAM device uses magnetism to store the data instead of electrical charges, as it occurs in the current devices. This guarantees non-volatility and near-infinite endurance in both reading and writing [5] processes, other than low power consumption and resistance to electrostatic disturbance. Because of the large potential, MRAMs have been proposed as a universal memory technology able to replace both SRAM and DRAM.

MRAM is based on the magnetoresitive effect (MR), that is the change in the electrical resistance of a magnetic material under the application of an external magnetic field [6], to retrieve the data. The first prototypes of MRAM exploited the fact that in ferromangets the magnetoresitance depends on the orientation between the magnetisation of the ferromagnetic layer with respect to the direction of the current flowing through the material. This effect, called anisotropic MR (AMR), allows to achieve change in the resistance of a few percent [5] in ferromagnetic alloys such as NiFe [7]. In the 1980s higher magnetoresitance was obtained in thin-film multilayer structures composed of a thin non-magnetic metallic layer sandwiched by two ferromagnetic leads (reference and free layer). Since the change in resistance was larger by an order of magnitude, the effect

was called giant MR (GMR) and the multilayer systems employed to obtain GMR are defined spin-valves. GMR up to $\sim 20\%$ was achieved, enough for use as a read head for hard drives, but not able to compete with the existing technology in the memory area.

A step forward in this sense was made with the replacement of the non-magnetic metal with an insulator. Such devices are called magnetic tunnel junctions (MTJs) since the electrons cross the barrier via tunnel effect, in contrast with spin valves where the electron are subjected to diffusive transport, and the magnetoresistive effect is defined tunnel MR (TMR). MTJs exploit the current out-of-plane or perpendicular (CPP) geometry where the flow of electrons is perpendicular to the layers and the contacts are both on the top and bottom of the multilayer structure. TMR occurs due to the spin-filtering effect in MTJs [8], in contrast to GMR where the resistance is determined by spin-dependent scattering [9, 2]. When the magnetisation of the ferromagnetic layers is parallel, the probability of tunnelling of majority electrons is larger than for minority electrons and large flux of spin polarised electrons across the barrier occurs. If the ferromagnetic layers have antiparallel magnetisation, both minority and majority electrons have low probability of tunnelling and the system has a high resistance. The difference in resistance can be expressed as

$$\text{TMR} = \frac{R_{\text{AP}} - R_{\text{P}}}{R_{\text{P}}}, \qquad (1.1)$$

where R_{AP} and R_{P} are the electrical resistance for the anti-parallel (high resistance) and parallel (low resistance) configuration, respectively.

The first MTJs used tunnel barriers made of amorphous materials such as AlO and reached TMR around 70 % at room temperature [10]. Successively, it was predicted and demonstrated that TMR up to 100% or larger could be obtained for MTJs with crystalline MgO(001) as barrier and Fe(001) as leads [11, 12]. When amorphous materials are used as tunnelling barriers, the probability of tunnelling depends on the electronic properties of the ferromagnetic leads. With crystalline materials, such as MgO, the band matching between the ferromagnetic materials and the barrier can provide better spin selectivity and higher TMR [8]. Larger TMR ratios have been predicted [13] for MTJ with electrodes made of Co or CoFe alloys and MgO as tunnelling barrier [14]. Experimentally Parkin *et al.* [15] obtained TMR ratios $\sim 200\%$ at room temperature in CoFeB/MgO/CoFeB MTJs prepared with sputtering and values around 1000% at low temperature have been measured [14].

MRAM is based on a MTJ where in its simplest architecture one electrode has the magnetisation fixed and act as a reference (reference layer or pinned layer, PL), whereas the magnetisation of the second ferromagnet is left free to respond to an external excitation (free layer or storage layer, FL). The information is stored in the form of the magnetisation of the FL, which is granted by the magnetic anisotropy of the free layer.
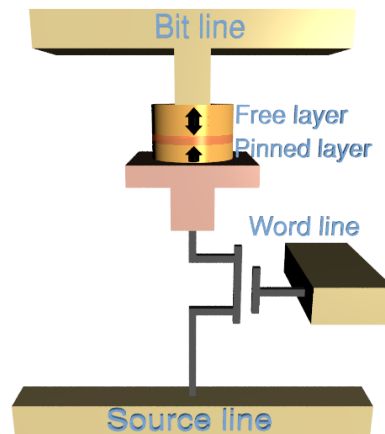
Figure 1.1 Schematic of a generic STT MRAM composed of a MTJ coupled to a transistor.

The reading is based on the magnetoresitance effect: a weak current is passed across the stack and either a large (bit 1) or small (bit 0) electrical resistance is measured depending on the relative orientation of the magnetisation in the pinned and reference layer. The writing process is achieved by reversing the orientation of the magnetisation of the storage layer. Such devices are non-volatile since they do not require power supply to store the information, and hence have low power consumption, are characterised by fast switching of the magnetisation, can be scaled down to small dimensions allowing larger storage density and provide resistance to electrostatic radiations. The writing is obtained by applying a magnetic field on the selected cell in a conventional MRAM. [16]. However, a field-induced switching MRAM is affected by limitations, in particular the high power consumption associated with the down-size scaling. In fact, a large magnetic field is required to switch the magnetisation of the FL and if the cell size is reduced, higher currents are required to generate the field pulse, resulting in high power consumption. To limit the current, this design cannot be scaled down beyond 90 nm [2].

MRAMs that make use of the spin transfer torque effect, called spin transfer torque MRAMs (STT MRAMs), offer the potential to be scaled down to smaller dimensions and to reduce the power consumption. A STT MRAM, sketched in Figure 1.1, gives its name to the spin-transfer-torque effect, a phenomenon predicted and discovered independently in the 1990s as complementary effect to GMR by Berger [17] and Slonczewski [18]. When an electrical current is sent through the pinned layer becomes spin polarised, i.e. minority electrons suffer scattering, whereas the majority electrons cross the layer unaffected. When a spin polarised electron flow crosses the barrier and arrives in the FL, it exerts a torque on the magnetisation of the FL via a transfer of angular momentum,

causing the magnetisation to precess. For low current densities the intrinsic damping of the FL will lead the magnetisation to its equilibrium configuration. If the spin-polarised current density is large enough, the torque can overcome the damping of the FL causing the reversal of the magnetisation direction. Since lower current densities are required to switch the orientation of the magnetisation of the storage layer than to generate a magnetic field pulse, STT MRAMs are better candidates for memory applications than field-induced MRAMs [1–3].

Despite the launch of STT MRAMs by Everspin at the end of 2016, there are features that need to be improved and solved. The switching current is relatively high, which results in large power consumption, compared with silicon-based devices. The fact that in a STT MRAM device the same path is used to read and write poses reliability issues for the tunnelling barrier. If the properties of the oxide layer degrade, both TMR and the lifetime of the MTJ are affected. Moreover, the stability of small elements needs to be improved to avoid that bits switch randomly due to thermal fluctuations, corrupting the stored data. To address such issues a deeper understanding of the fundamental and switching properties of these devices need to be achieved, alongside exploring alternative structures such as spin orbit torque MRAMs (SOT MRAMs) or voltage control magnetic anisotropy MRAMs (VCMA MRAMs) that might overcome these limitations [1, 3, 2].

1.3   Modelling of magnetic materials

The modelling of magnetic materials depends on the length scale and time scale of the problem. *Ab initio* models such as density functional theory (DFT) and Green's functions approaches, e.g. the fully relativistic Korringa–Kohn–Rostoker (KKR) methods [19, 20], use a quantum mechanical formalism that allows to determine the electronic properties starting from the electronic wave functions. One can calculate fundamental properties such as magnetic anisotropy, magnetic moments and exchange coupling energies. These methods come with a high computational cost and therefore *ab initio* simulations are limited to study periodic systems or finite systems with few hundreds of atoms in the cell size at most. Traditional DFT approaches have been developed to determine the ground state properties of a system and, as such, need corrections to deal with excitations and thermal effects. Time-dependent DFT (TDDFT) allows to investigate the properties of a system when in non-equilibrium and goes beyond DFT. However, the computational requirements for TDDFT are higher than for DFT and TDDFT cannot be used to study large systems or long time scales.

To model systems with a number of atoms between 10^4 and 10^9 and up to a hundred of nanoseconds, atomistic approaches are the most suitable [21]. In atomistic descriptions

the fundamental element is the atom and macroscopic quantities, such as the energy of the system, can be obtained by averaging over the individual atomic properties. The Heisenberg model is an example of atomistic spin formalism, where a magnetic moment is associated to each lattice site. Not only the equilibrium properties can be accessed, but also the dynamics of each spin can be studied via the Landau-Lifshitz-Gilbert equation of motion. Additionally, thermal effects can be introduced via a stochastic approach. This makes possible to investigate a variety of phenomena, from ultrafast laser induced magnetisation reversal to the current induced switching in magnetic tunnel junctions, to the study of more exotic systems such as skyrmions.

To study larger systems, from tens of nanometres to micrometres, a continuum approach is usually used. This approximation neglects the details at the atomic level and treats the physical quantities as continuous functions. This condition makes such methods, that go under the more general name of micromagnetism, unable to describe thermal effects accurately as well as sharp magnetisation transitions. Moreover, the computational costs pose limitations on both the length scale and time scale that can be accessed with these approaches. The kinetic Monte Carlo (kMC) method [22] is an approach that allows to reach longer time scales, of the order of hundreds of years, at finite temperatures allowing to go beyond the limitations of micromagnetism, if proper inputs are provided.

Atomistic models, micromagnetism and kMC are techniques that require input parameters, such as the exchange coupling or the transition probability. In atomistic models these can be obtained either from experiments or from *ab initio* calculations. Experimental results and microscopic parameters extracted from atomistic simulations can be input in micromagnetic calculations and the energy barriers between different energy minima in kMC can be supplied by atomistic or micromagnetic simulations. There is an interconnection between the different approaches that can be utilised to access and investigate accurately different time and length scales. Techniques that exploit this methodology are defined multiscale approaches and are gradually attracting more interest.

The nanometre size of magnetic tunnel junctions and the relatively short times of the magnetisation reversal of these systems make the atomistic framework the most adapt for the work discussed in this thesis. Therefore, in this thesis work the simulations are performed using an atomistic spin model, as implemented in the VAMPIRE software package [23], and a multiscale approach is used where possible.

Chapter 2

Atomistic spin model

After a brief introduction of the main quantities required to characterise a magnetic system, the atomistic model is discussed. The generalised Hamiltonian that describes the energy of a magnetic system, including all the energy contributions to the total energy, and the equations determining the magnetisation dynamics are presented.

2.1 Introduction

2.1.1 Magnetic moment

A simple way to introduce the concept of magnetic moment, one of the main quantities in magnetism, is to consider a classical picture of an electron spinning around the nucleus. The electron is a charged particle and as such its motion around the nucleus is equivalent to a current loop [24]. Such a current loop generates a magnetic moment

$$\mu = \int d\mu = I \int dA,$$
(2.1)

where I is the current of the loop and dA is the surface element of the loop whose direction is normal to the loop plane [6]. This is also the direction along which the magnetic moment points. If we consider a current loop with current I, area $A = \pi R^2$, orbital period $2\pi R/v$, where R is the radius of the loop and v the modulus of the speed of the electron of charge $-e$ and mass m_e, the moment can be expressed as:

$$\mu = -\frac{1}{2}evR$$
(2.2)

There is an orbital angular momentum L associated with the revolution of the electron which in classical mechanics is given by $L = m_e Rv$, whilst in quantum mechanics is quantised in units of $\hbar$. Equating these two relations the moment μ can be rewritten

as $\mu = -\mu_B$, where $\mu_B = 9.274 \times 10^{-24}\,\mathrm{Am}^2$ is the Bohr magneton. If each electron contributed μ_B, then the total magnetic moment in solids would be equal to integer multiples of μ_B. This is not what is observed experimentally, where the measured values are often only fractions of μ_B. In order to explain this discrepancy we need to resort to the band theory, discussed in section 2.2.3.

2.1.2 Orbital moment quenching and crystal field theory

Often, the interaction of an atom with its neighbouring atoms in a solid cannot be neglected. The way atomic properties are affected depends on the symmetry of the orbitals of the electrons within the atom, as this will yield a different interaction strength with the electric field generated by the electrostatic interaction with the screen charge of the surrounding atoms, i.e. the positively charged nuclei screened by the negatively charged core electrons, defined as the crystal field [6]. When the spin-orbit coupling is weak with respect to crystal field, as in the case of $3d$ transition metals, the orbitals will be filled depending on the relative strength between the crystal field and the energy required to pair two electrons, known as pairing energy, affecting the moment as well. If the crystal field is stronger than the Coulomb repulsion, the electrons will tend to double fill the lower energy levels initially, while in the opposite condition the electron will fill different levels first. Moreover, it has been shown that for the $3d$ series the moment seems to depend almost only on the spin angular momentum S rather than the total angular momentum $J = S + L$. When the spin-orbit is negligible, the orbital angular momentum does not contribute and it said to be quenched by the interaction with the surrounding [6]. The 4, $5f$ series do not exhibit quenching of the orbital moment since the orbitals are localised deep into the ion and do not feel the crystal environment. Therefore, these orbitals are subjected to a weaker crystal field and are characterised by larger spin-orbit coupling.

2.1.3 Magnetisation

The magnetisation $\vec{M}$ of a body is defined as the magnetic moment per unit volume. $\vec{M}$ is a macroscopic quantity and is experimentally measured by sensing the response of the system to an applied magnetic field given by $\vec{H}_{\mathrm{app}} = \vec{B}_{\mathrm{app}}/\mu_0$, without the sample. $\mu_0 = 4\pi \times 10^{-7}\,\mathrm{Hm}^{-1}$ is the permeability of free space and $\vec{B}$ the magnetic induction or magnetic flux. Once we add the sample, what we measure is the combination of the external applied magnetic field and the internal field caused by the magnetic moments within the magnetic body. The relation between $\vec{H}$ and $\vec{B}$ needs to be modified including

the magnetisation of the sample and becomes:

$$\vec{B} = \mu_0(\vec{M} + \vec{H}) \tag{2.3}$$

and can be used to determine $\vec{M}$. In the case of small fields, $\vec{M}$ varies linearly with the field following the relation $\vec{M} = \chi \vec{H}$. χ is the magnetic susceptibility and gives the response of the system to the external applied field. However, in most cases $\vec{M}$ is not a linear function of $\vec{H}$. To obviate this, the susceptibility can be expressed as $\chi = d\vec{M}/d\vec{H}$ evaluated at $H = 0$, i.e. the slope of $\vec{M}$ as function of $\vec{H}$ when approaching very small fields.

Finally, we note that a body with zero net magnetisation does not imply absence of magnetic moments necessarily, as domains or other sorts of ordering might be present. This will be further discussed in the next sections.

2.2   Exchange interaction

The exchange interaction is responsible for the macroscopic ordering we observe in magnetic materials. In the simple picture of a two electron system, the exchange interaction is caused by Pauli's exclusion principle [24]. This forbids the occupancy of a level by fermions with same set of quantum numbers. As a consequence, the global electronic wave function describing the two-electron system must be antisymmetric with respect to the exchange of particles. Following the description presented by Blundell [6], we can describe the single electronic wave function as a combination of a radial and spin component $\Psi_a(\vec{r}_i)$ and χ_a, respectively, where $\vec{r}_i$ is the position of the electron i in the state a. Given the antisymmetric requirement, the possible two-electron states are a singlet state and a triple state. The former is characterised by a symmetric radial part and an antisymmetric spin component with total spin $S = 0$, whereas the latter has a symmetric spin component and an antisymmetric radial component with total spin $S = 1$. The exchange energy parameter J_{ex} can be defined as function of the singlet and triplet energies E_s, E_t:

$$J_{\text{ex}} = E_s - E_t = \int\int d\vec{r}_1 d\vec{r}_2 \left[\Psi_a^\star(\vec{r}_1)\Psi_b^\star(\vec{r}_2)\mathcal{H}\Psi_a(\vec{r}_2)\Psi_b(\vec{r}_1)\right]. \tag{2.4}$$

$\mathcal{H}$ is the Hamiltonian describing the energy of the two electrons interacting with each other, i.e the Coulomb interaction, and E_s, E_t are given by the expectation value of the Hamiltonian over the singlet and triplet states, respectively. $\mathcal{H}$ can be written separating the energy terms in a spin-independent $\mathcal{H}_{\text{rad}}$ and spin-dependent $\mathcal{H}_{\text{spin}}$ term, and reads:

$$\mathcal{H} = \mathcal{H}_{\text{rad}} + \mathcal{H}_{\text{spin}} = \frac{1}{4}(E_s + 3E_t) - (E_s - E_t)\vec{S}_1 \cdot \vec{S}_2, \tag{2.5}$$

where $\vec{S}_1 \cdot \vec{S}_2$ comes from the expectation value of the total spin operator $\vec{S}$. $\mathcal{H}_{\text{spin}} = [(E_{\text{s}} - E_{\text{t}})\vec{S}_1 \cdot \vec{S}_2]$ and using Equation 2.4 can be expressed as a function of the exchange integral:

$$\mathcal{H}_{\text{spin}} = -J_{\text{ex}}\vec{S}_1 \cdot \vec{S}_2. \tag{2.6}$$

Analysing this equation we see that for positive J_{ex} the energy is lower when the system forms a triplet state ($S = 1$), whilst the singlet state ($S = 0$) is the lowest energy configuration if J_{ex} is negative. Therefore, the spins will align anti-parallel in the singlet case and parallel in the triplet state. This result exemplifies the role of the exchange coupling in determining the magnetic ordering in a system, despite the fact that the considered system is a simple model.

What has been described so far does not represent the situation in real materials. These are in fact composed of billions of atoms and each atoms will have more than one electron. Therefore, the interaction between neighbouring atoms needs to be considered. However, a description able to handle the totality of atoms and electrons is not feasible and approximations are required. An approach that deals with a multi-electron system is an extension of the Heisenberg model, that in the original approach describes the interaction between two electrons. Within the extended Heisenberg approximation, the spin-dependent component of the Hamiltonian can be written as:

$$\mathcal{H}_{\text{spin}} = -\sum_{i<j} J_{ij}\vec{S}_i \cdot \vec{S}_j, \tag{2.7}$$

where the summation is extended on all the electrons of the system avoiding double counting, J_{ij} is the exchange energy between the spin i and j and $\vec{S}_{i,j}$ are the respective spin vectors. This direct exchange cannot justify the magnetic ordering in most materials on its own. In fact, overlap between orbitals is required to have direct exchange, but in materials such as rare-earth elements the $4f$ electrons are very close to the nucleus and do not provide sufficient overlap. In case of transition metals instead, if we account only for the electrons that are unpaired we would obtain results far off from what is measured. To deal with these complications, other theories are needed and they will be object of the Section 2.2.3.

2.2.1 Magnetic ordering

Depending on the internal ordering of the spins within the body, magnetic materials are classified as:

  a) ferromagnetic;

  b) antiferromagnetic;
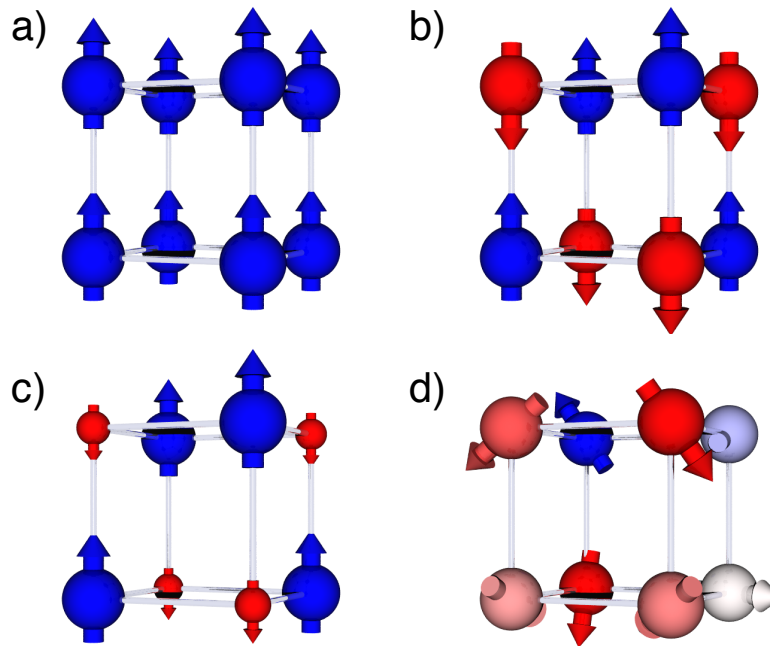
Figure 2.1 Examples of magnetic ordering in the simple case of a simple cubic system. The colour scheme describes the z-component of the magnetisation (blue = +z, white = in-plane and red = -z). Ferromagnetic and antiferromagnetic ordering are presented in a) and b), respectively. c) shows the case of a ferrimanget, where the two sublattices have the spins oriented along opposite directions and different magnitude of the atomic moment, which causes a net magnetisation differently from an antiferromagnet (b)). In d) a paramagnetic systems is shown.

  c) ferrimagnetic;

  d) paramagnetic.

Figure 2.1 shows examples of the different magnetic ordering configurations. A ferromagnetic body has all the spins aligned along a specific direction; an antiferromagnet is generally characterised by the existence of two sub-lattices at the atomic level with opposite magnetisation, which gives rise to a zero net magnetisation. The susceptibility of an antiferromagnet increases until it reaches a maximum at the critical temperature above which the ordering is lost, that is an indication of the fact that antiferromagnetic materials do not respond to an applied magnetic field. A similar class is composed by ferrimagnets. These are materials where the magnetisation of the two sublattices points in opposite direction, but it does not cancel out in magnitude. Therefore, ferrimagnets exhibit a low net magnetic moment. A paramagnet is instead a material where the atomic spins are oriented randomly, yielding zero net magnetisation.

2.2.2   Thermal effects

Magnetic materials exhibit a magnetic ordering below a critical temperature, called the Curie and Néel temperature for a ferromagnet and antiferromagnet, respectively. In the case of a ferromagnet, at low temperature the exchange coupling determines the alignment of the atomic moments, while as the temperature rises, thermal contributions cause disorder within the system resulting a reduction of the magnetisation. At the Curie temperature a phase transition occurs, and the system becomes paramagnetic with zero net magnetisation, as shown by the black dots in Figure 2.3.

2.2.3   Itinerant ferromagnetism

As discussed previously, the fractional magnetic moments of $3d$ metals such as Fe, Co and Ni and the ferromagnetic character cannot be explained with the help of the localised model. In metals, conduction electrons are delocalised and are shared among all the atoms, in contrast with the localised electron picture where an electron spends most of the time orbiting around a specific atomic site. In the case of the Fe-series, both the $4s$ and $3d$ electrons contribute to transport and electronic properties, whereas the magnetic properties arise mainly from the latter. Moreover, the orbital moment of these elements is quenched by the crystal field. In a simple picture, the outer electrons in a metal can be treated as free electrons, i.e. non-interacting, and the crystal field interaction neglected. Within this approach, known as Bloch model [24], the electrons fill the energy levels up to the highest occupied level, defined as Fermi energy (E_F). As in metals the atomic levels hybridise broadening and forming electronic energy bands instead of single atom energies, a more appropriate tool to describe the energetic properties is the density of states $D(E)$. $D(E)dE$ represents the number of electron energy levels per unit volume within the energy range $[E, E+dE]$. The electron density n can then be obtained via the expression $n = \frac{1}{V} \int_{E_{-\infty}}^{E_F} D(E)dE$ [25], where V is the volume. The energy levels are equally occupied by spin-up/spin-down ($\uparrow\downarrow$) electrons up to E_F and the system does not exhibit a magnetic character. However, the application of an external magnetic field can break the spin degeneracy promoting electrons from a spin-polarised band to the other and creating a deficiency of electrons in the same band. This unbalance between $\uparrow$ and $\downarrow$ polarisation induces a weak paramagnetic character, referred to as Pauli paramagnetism. It can be shown [6, 24] that the arising magnetisation is related to the difference in density of spin-up ($n^{\uparrow}$) and spin-down ($n^{\downarrow}$) electrons and to the density of states at E_F ($D(E_F)$).

   This approach works for some metals, but cannot explain the strong ferromagnetism in the Fe-series. Based on Pauli paramagnetism, the spin-splitting must be a spontaneous effect to induce a ferromagnetic character. If we assume a spin-splitting between up and down bands an exchange energy contribution arises. This exchange contribution is

characterised by the intra-atomic Coulomb energy term U, that represents the energy cost of introducing the spin-degeneracy. As shown by Blundell [6] and Skomski [24], this configuration becomes favourable when the Coulomb repulsion is comparable with the kinetic energy. This can be expressed via the Stoner criterion $U \frac{1}{2} D(E_F) > 1$, where $\frac{1}{2} D(E_F)$ is the spin-polarised density of states. Such condition requires a large Coulomb term and a large density of states close to E_F. If the condition is not met, but the element has a large density of states close to E_F and a large number of $3d$ electrons as in Pt and Pd, it can be easily spin-polarised when in proximity of magnetic elements and a large induced magnetic moment can occur. Even though the delocalised approach is required to explain the magnetic moment and the occurrence of ferromagnetism in the Fe-series, the large inter-atomic distances in $3d$ transition metals yield narrow bands and small hopping. Because of these factors, the delocalised $3d$ electrons of Fe, Co and Ni can often be approximated using the independent or localised electron approach [24], as it will be done in the simulations presented in the following.

2.3   Magnetic anisotropy

In materials that exhibit a magnetic character, be it ferromagnetism, antiferromagnetism or ferrimagnetism, the magnetic properties depend on the direction they are measured, i.e. they are anisotropic. The magnetic anisotropy can be classified in different categories, each one characterised by a different origin. One of the most common and important kinds of magnetic anisotropy is the magneto-crystalline anisotropy. This anisotropy arises due to the spin-orbit coupling between orbital and spin angular momentum of the electrons and depends on the crystal symmetry. In rare-earth $4f$ materials the spin-orbit coupling is strong compared with the crystal field and the orbital moment is largely unquenched, giving rise to high anisotropy energies of the order of $1 \, \mathrm{MJm}^{-3}$ [24]. When the crystal field contribution is large with respect to the spin-orbit interaction and the orbital moment is quenched, the resultant uniaxial anisotropy is weak. This is the case of $3d$ transition metals. The magneto-crystalline anisotropy favours the alignment of the magnetisation along a certain specific crystallographic direction, defined as easy-axis. An example of material that exhibits uniaxial anisotropy is Co[0001], where the magnetisation points along the out-of-plane axis and the anisotropy is of the order $0.5 \, \mathrm{MJm}^{-3}$. The uniaxial anisotropy energy density per unit volume for a magnet whose symmetry axis does not vary spatially, limiting the expression of the energy to low order terms in $\sin(\vartheta)$, can be expressed as [26, 24]:

$$E_a^u = K_1^u \sin^2(\vartheta) + K_2^u \sin^4(\vartheta) + \ldots \ . \tag{2.8}$$

ϑ is the angle between the symmetry axis and the body magnetisation, K_1^u and K_2^u are second order and fourth order anisotropy energy densities in the magnetisation, respectively. K_2^u is order of magnitude smaller than K_1^u for most bulk magnets and it is often ignored [26, 24]. If we neglect K_2^u, the anisotropy is governed by K_1^u and, depending on its sign, the easy-axis lies parallel ($K_1^u > 0$) or orthogonal ($K_1^u < 0$) to the symmetry axis. Figure 2.2(a) and Figure 2.2(b) present the energy landscape corresponding to these cases.
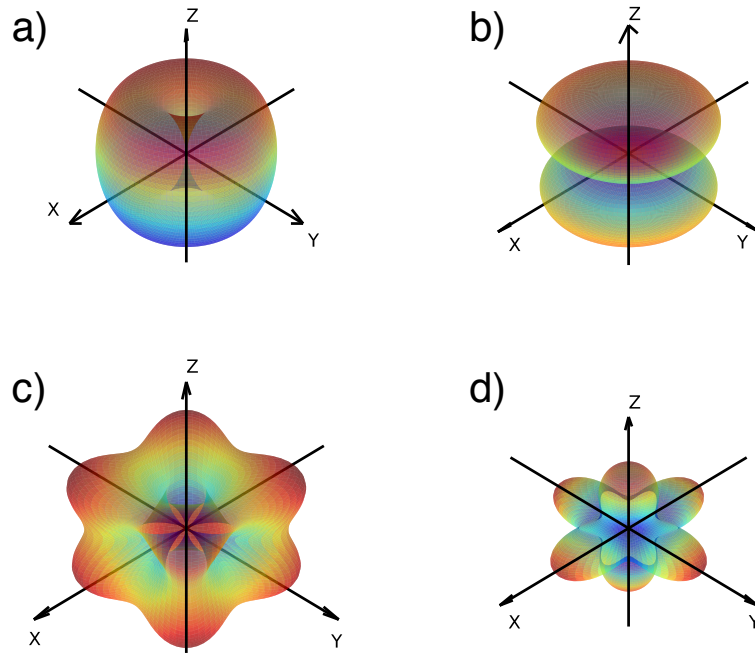
Figure 2.2 Energy surfaces for a uniaxial system with negligible K_2^u and $K_1^u > 0$ (a) and $K_1^u < 0$ (b). c)-d) show the energy surface for a system with cubic anisotropy with $K_1^u > 0$ and $K_1^u < 0$, respectively. In all the plots, the energy increases going from blue (minimum) to red (maximum) as well as the distance from the origin.

Not all materials are characterised by uniaxial anisotropy. Depending on the crystal environment, more than one symmetry axis may exist. An example is presented by cubic crystals where there are three or four equivalent easy-axes depending on the sign of the lowest order cubic anisotropy constant, as in the case of Fe and Ni. For a cubic system whose easy-axes are aligned along xyz-axes, the anisotropy energy up to the lowest order is given by [26]:

$$E_a^c = K_1^c \left(m_x^2 m_y^2 + m_x^2 m_z^2 + m_y^2 m_z^2 \right) + \dots, \tag{2.9}$$

where $m_{x,y,z}$ are the component of the reduced magnetisation unit vector $\vec{M}/|\vec{M}|$ and K_1^c is the cubic anisotropy energy constant.

MRAMs are bi-stable devices characterised by uniaxial anisotropy and the height of this magnetic energy provides the energy barrier between the two energy minima of the system against unwanted transitions caused by the thermal contribution. The anisotropy energy, similarly to what occurs with the magnetisation, depends on temperature and typically shows a decrease as the temperature increases. The decrease of the energy barrier with temperature is an important factor to be taken into account when miniaturising a device. H. B. Callen and E. Callen [27] investigated the temperature dependence of the magneto-crystalline energy. They derived an expression that allows to write the latter as function of the temperature dependence of the magnetisation, with $K(T) \propto M(T)^3$ and $K(T) \propto M(T)^{10}$ for uniaxial and cubic anisotropy, respectively. The anisotropy decreases faster than the magnetisation at higher temperatures, a feature that can be exploited in technologies such as heat assisted magnetic recording (HAMR) media [28]. An example of the different temperature dependence of the magnetisation and anisotropy for a uniaxial and cubic system is presented in Figure 2.3 (blue and yellow points).
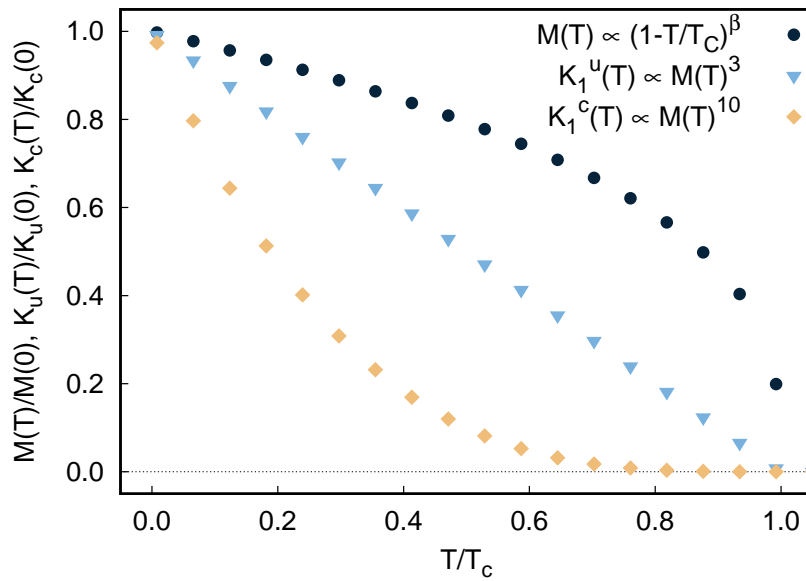
Figure 2.3 Example of temperature scaling of magnetisation (black dots) and anisotropy following Callen-Callen model. The temperature dependence of the magnetisation follows $(1 - T/T_c)^\beta$ with $\beta = 0.3$.

The magnetostatic interaction between all the magnetic moments within a body is responsible for another kind of magnetic anisotropy [26], defined shape anisotropy (see also Section 2.4). This contribution can be dominant in the case of polycrystalline materials, where the symmetry axes are randomly oriented within the sample resulting in either zero or weak magneto-crystalline anisotropy. Shape anisotropy depends on the

shape of the magnetic body, as the name suggests, and favours magnetic configurations that minimise free magnetic charges.

The magnetic anisotropies described so far depend on the bulk properties of the system. However, most of the current technological applications involves complex structures composed of few atomic layers, such as in recording media and storage devices or thin films. The presence of interfaces and surfaces breaks the bulk symmetry allowing for higher anisotropy contributions that can compete with the bulk magneto-crystalline anisotropy, yielding complex energy landscapes. Such contributions are limited to the atomic layers in proximity of the surface or interface and can be described by the following phenomenological relation [24]:

$$K_{\text{tot}} = K_{\text{b}} + \frac{K_{\text{s}}}{t}. \tag{2.10}$$

K_{b} is the bulk uniaxial anisotropy that accounts for the bulk magneto-crystalline anisotropy K_1 and the magnetostatic shape anisotropy, t the film or layer thickness and K_{s} the surface or interfacial anisotropy.

2.4 Dipolar energy

The magnetic dipolar energy E_{dip}, also referred to as demagnetising or demagnetisation or magnetostatic energy, describes the interaction between two magnetic moments μ_i, μ_j separated by a distance $\vec{r}_{ij} = \vec{r}_i - \vec{r}_j$. In the dipolar approximation, E_{dip} is given by (in SI units):

$$E_{\text{dip}}^{ij} = -\frac{\mu_0}{4\pi|\vec{r}_{ij}|^3} \left[\frac{3(\vec{\mu}_i \cdot \vec{r}_{ij})(\vec{\mu}_j \cdot \vec{r}_{ij}) - (\vec{\mu}_i \cdot \vec{\mu}_j)|\vec{r}_{ij}|^2}{|\vec{r}_{ij}|^2} \right]. \tag{2.11}$$

E_{dip} depends on the mutual orientation of the magnetic moments and its magnitude decreases with distance as $1/|\vec{r}_{ij}|^3$. Moreover, the calculation of the magnetostatic interactions in a solid needs to be extended including a summation over all the pairs of magnetic moments within the body. The demagnetising contribution is also seen as a shape anisotropy, as the long ranged nature of this interaction cause a dependence on the overall shape of the body. The dipolar energy calculation will be discussed in more detail in Chapter 3.

2.5 Atomistic spin model

The atomistic spin modelling is analogous to a molecular dynamics approach, where the focus is on the dynamics of the atomic spin moment rather than the atomic displacement. The energetics of the system is described by a Hamiltonian that includes exchange energy,

anisotropy energy, magnetostatic energy and energy due to the application of an external field. The dynamics of the atomic moments is governed by the Landau-Lifshitz-Gilbert (LLG) equation of motion, whereas equilibrium properties can be calculated via a Monte Carlo approach.

2.5.1   Generalised Heisenberg Hamiltonian

In Section 2.2 the Heisenberg Hamiltonian describing the energy of a system of adjacent magnetic moments was presented. A magnetic material is characterised by not only the exchange coupling. The Heisenberg formalism can be extended to take into account these other energy contributions to the magnetic behaviour of the system:

$$\mathcal{H} = -\sum_{i<j} J_{ij}\vec{S}_i \cdot \vec{S}_j - \sum_i k_u^i(\vec{S}_i \cdot \hat{e})^2 - \mu_0 \sum_i \mu_s^i \vec{S}_i \cdot \vec{H}_{app} + \mathcal{H}_{demag}, \qquad (2.12)$$

where J_{ij} is the exchange coupling constant for the interaction between the spins on site i and j, k_u^i is the on-site uniaxial energy constant on site i along the axis $\hat{e}$, μ_s^i is the atomic spin moment on the atomic site i in units of μ_B and μ_0 is the permeability constant. These parameters can be obtained either by experiments and converted to atomistic values or by *ab initio* density functional theory (DFT) calculations. For instance, J_{ij} is related to the Curie temperature T_c via $J_{ij} = 3k_B T_c/(\varepsilon z)$ [29], where z is the number of nearest neighbours and ε depends on the crystal structure and coordination number, and can be accessed from measurements of T_c. On the other hand, *ab initio* and atomistic spin models can be interfaced as they are both on the atomic scale. Local magnetic moments and on-site anisotropies energies can be calculated by performing calculations with standard DFT codes, while site resolved properties can be calculated by using Green's functions approaches, such as the fully relativistic Korringa–Kohn–Rostoker (KKR) methods [19, 20]. For this reason, multiscale models based on the integration of parameters obtained from first principle calculations as input for an atomistic spin approach are an extremely valuable tool to investigate the electronic and magnetic properties of magnetic materials. The terms on the RHS of Equation 2.12 represent isotropic nearest-neighbours exchange energy, uniaxial magnetic anisotropy energy, the coupling with an external field or Zeeman energy and magnetostatic energy, respectively. The first three terms are short range in the majority of magnetic systems. The dipolar coupling involves the totality of the spins within the systems and for this reason an accurate calculation of this term is computational expensive. Details about how the magnetostatic interaction is computed are given in Chapter 3. A further extension of the Heisenberg model is to consider an exchange coupling beyond the isotropic approximation. The exchange Hamiltonian can be written

as $\mathcal{H}_{\text{ex}} = -\sum_{i<j} \vec{S}_i \bar{\bar{J}}_{ij} \vec{S}_j$ where $\bar{\bar{J}}_{ij}$ is the exchange tensor given by:

$$\bar{\bar{J}}_{ij} = J_{ij}\mathbb{1} + \bar{\bar{J}}_{ij}^S + \bar{\bar{J}}_{ij}^A. \tag{2.13}$$

$\mathbb{1}$ is the identity matrix of the same rank as $\bar{\bar{J}}_{ij}$ and

$$J_{ij} = \frac{1}{3}\text{Tr}(\bar{\bar{J}}_{ij}), \tag{2.14}$$

$$\bar{\bar{J}}_{ij}^S = \frac{1}{2}\left[\bar{\bar{J}}_{ij} + \bar{\bar{J}}_{ij}^t - J_{ij}\mathbb{1}\right], \tag{2.15}$$

$$\bar{\bar{J}}_{ij}^A = \frac{1}{2}\left[\bar{\bar{J}}_{ij} - \bar{\bar{J}}_{ij}^t\right] \tag{2.16}$$

are the isotropic exchange constant, the symmetric and antisymmetric component of the exchange tensor, respectively. $\bar{\bar{J}}_{ij}^A$ is associated with the Dzyaloshinskii-Moriya interaction [30, 31] and can be responsible for non-collinear spin configurations when not negligible, as it can occur at interfaces where there is symmetry breaking. The exchange tensor $\bar{\bar{J}}_{ij}$ can be obtained by performing simulations with KKR methods.

2.5.2   Landau-Lifshitz-Gilbert (LLG) equation

The dynamics of a magnetic moment can be described by the Landau-Lifshitz-Gilbert (LLG) equation of motion [32]. This represents a similar formulation to that proposed by Landau and Lifshitz (LL) in 1935 [33], which has been the first description of the dynamics of a ferromagnet. The LLG equation gives the rate of change of the atomic spin moment $\vec{S}_i$ and reads:

$$\frac{d\vec{S}_i}{dt} = -\frac{\mu_0 \gamma}{(1+\alpha^2)}\left[\vec{S}_i \times \vec{\text{H}}_{\text{eff}}^i + \alpha \vec{S}_i \times \left(\vec{S}_i \times \vec{\text{H}}_{\text{eff}}^i\right)\right]. \tag{2.17}$$

$\vec{S}_i$ is the normalised unitary spin vector on site i, $\gamma = 1.760{,}86 \times 10^{11}\,\text{s}^{-1}\text{T}^{-1}$ is the gyromagnetic ratio of the electron, $\vec{\text{H}}_{\text{eff}}^i$ is the net effective field acting on the spin i which takes into account all the contributions in the Hamiltonian and is obtained by differentiating the spin Hamiltonian 2.12 with respect to the magnetic moment:

$$\vec{\text{H}}_{\text{eff}}^i(t) = -\frac{1}{\mu_0 \mu_s^i}\frac{\partial \mathcal{H}}{\partial \vec{S}_i}. \tag{2.18}$$

α is a phenomenological Gilbert damping parameter that describes the relaxation of the atomic spins towards the direction of the effective field. In the atomistic framework, the damping term does not necessarily coincide with the macroscopic Gilbert term and couples the spins with a heat bath controlling the energy transfer between them. α
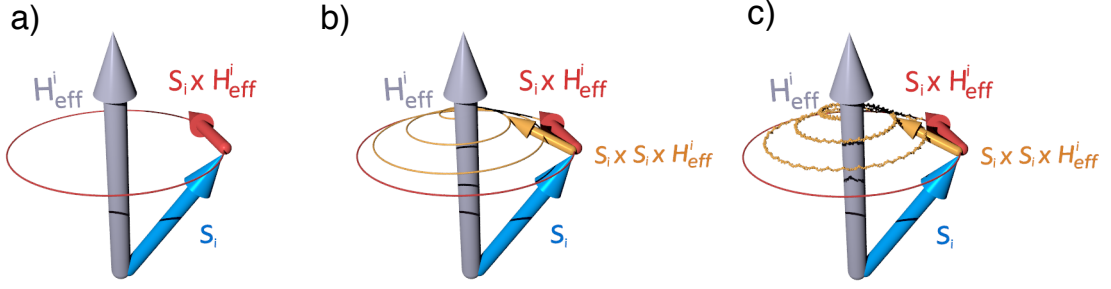
Figure 2.4 Illustration of the atomic magnetic moment $\vec{S}_i$ precession around the effective field $\vec{H}^i_{\text{eff}}$ for a) undamped motion and b) motion with damping. c) shows the effect of the thermal fluctuations on the precession of a spin: the trajectory is now affected by random fluctuations whose amplitude depends on the temperature. In b) and c) the red trajectory, which represents the undamped motion without thermal fluctuations, is shown as a comparison.

also includes the transfer of angular momentum within the same magnetic system via the excitation of propagating deviations in the ordering of the magnetic texture, called spin-waves [34]. The first term on the RHS of Equation 2.17 derives from a quantum mechanical treatment and describes the precession of the spin moment around $\vec{H}_{\text{eff}}$ due to the torque exerted by $\vec{H}_{\text{eff}}$ on the spin moment. The second term has a phenomenological origin and it describes the damped motion of the spin moments towards the effective field. Figure 2.4(a) and Figure 2.4(b) show the undamped motion of the atomic spin around the effective field and the relaxation of the former towards the latter when a damping term is considered, respectively.

2.5.3 Stochastic LLG equation

To describe systems at finite temperature a stochastic field $\vec{\xi}_i$ is included in the effective field:

$$\vec{H}^i_{\text{eff}}(t) = -\frac{1}{\mu_0 \mu^i_{\text{s}}} \frac{\partial \mathcal{H}}{\partial \vec{S}_i} + \vec{\xi}_i(t), \tag{2.19}$$

which couples the spin system with a heat bath. This term takes into account both dissipation effects and exchange of angular momentum. Following Brown's approach [35], usually referred as Langevin dynamics, the thermal field can be described as a white noise term [36, 37]. For such an approximation to be valid, the requirement is that the time correlation between the fluctuations induced by the thermal field is shorter than the spin motion [35]. This is generally the case for magnetisation dynamics that occurs on the nanosecond time-scale or slower, as it happens for the phenomena studied in this work. In this white noise limit, the thermal field is described by a Gaussian distribution in 3 dimensions and the statistical moments of the distribution are found by applying the

fluctuation theorem and the Fokker-Planck equation:

$$\langle \xi_{i\alpha}(t) \rangle = 0, \tag{2.20}$$

$$\langle \xi_{ia}(t) \xi_{jb}(t\prime) \rangle = \frac{2\alpha k_{\mathrm{B}} T}{\mu_{\mathrm{s}} \gamma} \delta_{ij} \delta_{ab} \delta(t-t'), \tag{2.21}$$

where i, j label spins on the respective sites, $a, b = x, y, z$ are the vector component of $\vec{\xi}$ in Cartesian coordinates, t, t' are the time at which the Gaussian fluctuations are evaluated, T is the temperature, δ_{ij} and δ_{ab} are Kronecker delta and $\delta(t-t')$ is the delta function. Equation 2.20 represents the average of the random field, whereas Equation 2.21 gives the second moment of the field, which is a measure of the strength of its fluctuations. Since the magnitude of the fluctuations of the thermal field is directly proportional to the temperature, the effect of this randomising field increases with temperature. Moreover, the damping parameter enters in equation 2.21, coupling the spins with the thermal bath in addition to provide transfer of angular momentum. The randomising effect of the fluctuations induced by the thermal energy is presented in Figure 2.4 (c).

2.6 Conclusions

The main quantities necessary to describe a magnetic system and their origin have been presented in the chapter. A brief introduction of the atomistic spin model and the main equations that characterise it have also been discussed in the chapter.

Chapter 3

Development of dipole-dipole interaction

In magnetic bodies exchange interactions are responsible for the short range magnetic ordering, favouring either parallel or antiparallel alignment of the spins. On the other hand, magnetostatic or dipolar interactions are long-ranged and favour the formation of magnetic domains because this reduces the total magnetisation of the system via flux closure. The long-range nature of such interactions makes the calculation of this contribution dominate the compute time of magnetic properties. Therefore, different approaches and approximations are used in order to balance the accuracy of the calculation with the heaviness of the computation.

In the following a method to compute the magnetostatic interactions within the atomistic spin model is presented. Afterwards, an extension of this approach that allows to improve the accuracy of the calculation, that relies on the atomic position within the magnetic body, is discussed and finally tests relative to the implementation are shown.

3.1   Introduction

Magnetostatic coupling arises in a magnetic system due to the magnetisation distribution of the body itself. An expression for the magnetostatic field can be obtained from Maxwell's equations assuming zero electric current within the system [38, 24]. Under this assumption, the magnetic field can be written as:

$$\vec{H}\left(\vec{r}\right) = \frac{1}{4\pi}\left[\int_{V'} dV' \rho_{\mathrm{M}}\left(\vec{r}'\right)\frac{\vec{r}-\vec{r}'}{|\vec{r}-\vec{r}'|^3} + \int_{S'} dS' \sigma_{\mathrm{M}}\left(\vec{r}'\right)\frac{\vec{r}-\vec{r}'}{|\vec{r}-\vec{r}'|^3}\right],\qquad(3.1)$$

where $\vec{M}$ is the magnetisation of the system, $\rho_{\mathrm{M}}\left(\vec{r}\right) = -\nabla\cdot\vec{M}$ and $\sigma_{\mathrm{M}}\left(\vec{r}\right) = \vec{n}\cdot\vec{M}$ are the volumetric and surface charge densities of the magnetisation, respectively, V and S are

the volume and the surface area of the magnetic system, $\vec{n}$ is a unit vector normal to S and $\vec{r}$ is the distance between two dipoles within the body. Since this expression is not solvable analytically other than for some simple case and is computationally expensive, approximations have been developed in order to calculate the magnetostatic contribution. One of the simplest is the dipole approximation. In micromagnetic software packages, such as OOMMF [39] and MuMax [40], the system is divided into a regular array of cubes and the magnetostatic contribution can be calculated analytically based on the work by Newell *et al.* [41].

In the dipole approximation each magnetic moment is considered as a magnetic dipole. If the magnetisation of the body is uniform, only $\sigma_M(\vec{r}) = \vec{n} \cdot \vec{M}$ contributes in Equation 3.1 and the integral can be expressed in a more simple form. Finally, expanding the term $|\vec{r} - \vec{r}'|^{-1}$ and taking the first non-zero contribution, one arrives at the following expression for the field:

$$\vec{H}(\vec{r}) = \frac{1}{4\pi} \left[\frac{3\vec{r}(\vec{\mu} \cdot \vec{r})}{|\vec{r}|^5} - \frac{\vec{\mu}}{|\vec{r}|^3} \right]. \tag{3.2}$$

$\vec{\mu}$ is the magnetic moment vector aligned along the magnetisation defined as $\vec{\mu} = M_s V \hat{M}$, M_s is the equilibrium magnetisation of the magnetic body and $\hat{M}$ the unit vector pointing in the direction of the magnetisation. This is the lowest order term of the multipole expansion and larger accuracy can be achieved including higher orders at the expense of increasing the computational complexity. Exploiting the fact that the terms inside the brackets in Equation 3.2 depend on the geometry of the system only, Equation 3.2 can be rearranged in a tensorial form:

$$\vec{H}(\vec{r}) = \bar{\bar{D}} \cdot \vec{\mu} \tag{3.3}$$

where $\bar{\bar{D}}$ is the dipolar tensor that contains the geometric information. In Cartesian coordinates, $\bar{\bar{D}}$ is given by:

$$\bar{\bar{D}} = \frac{1}{4\pi r^5} \begin{pmatrix} 3r_x^2 - r^2 & 3r_x r_y & 3r_x r_z \\ 3r_y r_x - r^2 & 3r_y^2 - r^2 & 3r_y r_z \\ 3r_z r_x & 3r_z r_y & 3r_z^2 - r^2 \end{pmatrix}, \tag{3.4}$$

where we have dropped the heavy notation $|\vec{r}|$ to make the expression more readable and r_α with $\alpha = x, y, z$ are the components of $\vec{r}$ along the respective axes. Similarly, $\vec{\mu}$ can be expressed in Cartesian components:

$$\vec{\mu} = \begin{bmatrix} \mu_x \\ \mu_y \\ \mu_z \end{bmatrix}. \tag{3.5}$$

In micromagnetic approaches, to apply the dipole approach the system is generally subdivided into regions of uniform magnetisation. Each of these is considered as a dipole and the magnetostatic field is given by the sum of the contribution of each single dipole. In an atomistic model one could consider each single atomic moment and compute the dipolar interaction for each of the spins. Given the large number of spins even in a relatively small system, such an approach is infeasible due to the memory required to store the dipolar matrix and the large number of calculations involved. On the other hand, magnetostatic interactions affect the system properties on a nanometre scale and should be accounted for. Therefore, in atomistic calculations with more than a few thousands spins, a micromagnetic-like approach where the system is discretised in regions of uniform magnetisation can be adopted [42]. In addition, since for magnetisation processes slower than ultrafast dynamics the global magnetisation varies on a slower time scale than the atomic moments, the calculation of magnetostatic interactions associated with these changes can be updated less frequently. In the following we present the simplest method to calculate the demagnetisation processes which makes use of a macro-cell approach, called the bare macro-cell approach, and afterwards we discuss a more elaborate and accurate method. Finally, we present tests on the accuracy of the developed approach.

3.2 Bare macro-cell approach

The bare macro-cell approach, the method to calculate the magnetostatic contribution initially adopted in VAMPIRE [23, 43], consists of dividing the system in macro-cells of fixed size and shape, as shown in Figure 3.1. The magnetic moment $\vec{m}_{mc}$ in each
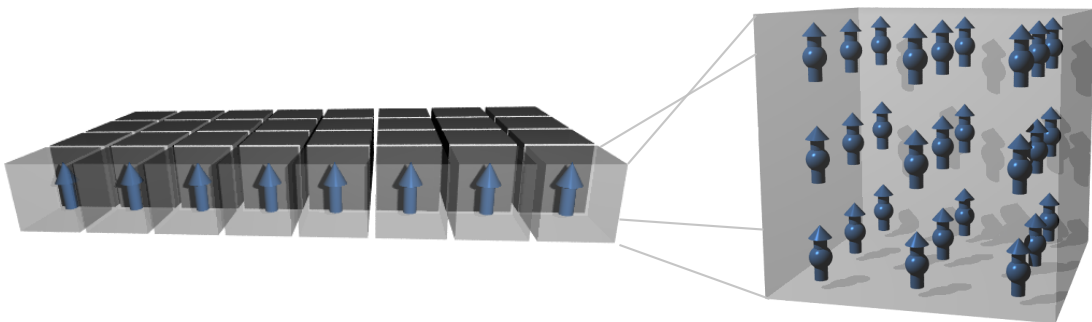
Figure 3.1 Schematic representation of the macro-cell approach used to calculate the demagnetisation field where the system is discretised into cubic macro-cells (left). Each macro-cell, which includes several spins, is characterised by a macro-moment given by the averaged moment of the spins within the cell (right). This approximation relies on the condition that the magnetisation is uniform within the macro-cell.

macro-cell is obtained calculating the vector sum of the atomic spin moments within each

cell as:

$$\vec{m}_{\mathrm{mc}} = \sum_{i}^{n} \mu_{\mathrm{s}}^{i} \vec{S}_{i}, \tag{3.6}$$

where n is the total number of spins within the macro-cell, μ_{s}^{i} is the local atomic spin moment value and $\vec{S}_{i}$ is the reduced unit spin vector for the spin i in the macro-cell. The macro-cell is chosen to be cubic for the sake of simplicity and the size can be selected depending on the accuracy required. It is worth noting that the method requires uniform magnetisation within a macro-cell. Therefore, the macro-cell dimension should be such that is several times smaller than the domain-wall size. This would guarantee a uniform magnetisation within the cell. Moreover, at elevated temperatures the macro-cell moment decreases due to thermal spin fluctuations yielding a reduction of the effect of magnetotstatic interactions. Thus, the use of a small macro-cell size allows to compute the magnitude of the macro-moment in a more accurate way, similarly to stochastic micromagnetic simulations. The magnetisation of each macro-cell is determined as the magnetic moment per volume of the macro-cell. The macro-cell volume V_{mc} depends on the crystal structure of the system and therefore, to estimate it we calculate an effective volume determined by the number of atoms in the macro-cell and the size of the unit cell of the crystal structure. V_{mc} is obtained as:

$$V_{\mathrm{mc}} = n_{\mathrm{mc}} V_{\mathrm{atom}} = n_{\mathrm{mc}} \frac{V_{\mathrm{uc}}}{n_{\mathrm{uc}}}, \tag{3.7}$$

where n_{mc} is the number of atoms in the macro-cell, n_{uc} is the number of atoms in the unit cell and V_{uc} is the volume of the unit cell. We note that for unit cells much smaller than the macro-cell size, Equation 3.7 is a good approximation. However, for a large unit cell with significant free space, for example a nanoparticle in vacuum, the free space contributes to the effective volume, which reduces the effective macrocell volume and the accuracy of the calculation.

Since each macro-cell is treated as a magnetic dipole, the cells are localised at their centre. In order to account for partial occupations of the macro-cell and different atomic spin moments, the position of the centre $\vec{p}_{\mathrm{mc}}$ is corrected by weighting the coordinates by the magnetic moments. $\vec{p}_{\mathrm{mc}}$ can be expressed as:

$$\vec{p}_{\mathrm{mc}} = \frac{\sum_{i}^{n} \mu_{\mathrm{s}}^{i} \vec{p}_{i}}{\sum_{i}^{n} \mu_{\mathrm{s}}^{i}}, \tag{3.8}$$

where $\vec{p}_{i}$ is the position vector of the atomic moment localised on site i and the other quantities are the same as in Equation 3.6. In the case of a non fully occupied macro-cell, such as the edge of a finite size system, Equation 3.8 moves $\vec{p}_{\mathrm{mc}}$ towards the more densely populated region, whereas it shifts $\vec{p}_{\mathrm{mc}}$ closer to spins with larger μ_{s} if more than one

type of magnetic species is present. The approach of displacing the centre of the cell increases the accuracy with respect to a standard calculation where this correction is not accounted for. However, it has the downside that the dipoles are not situated on a regular grid any more and therefore, computational approaches that require an ordered mesh, such as fast Fourier transform (FFT), cannot be applied.

The dipolar field within each macro-cell p is given by:

$$\vec{B}^p_{\text{dip,mc}} = \frac{1}{4\pi} \left[\sum_{p \neq q} \frac{3 \left(\vec{m}^q_{\text{mc}} \cdot \hat{r}_{pq} \right) \hat{r}_{pq} - \vec{m}^q_{\text{mc}}}{r^3_{pq}} \right] + \frac{2}{3} \frac{\vec{m}^p_{\text{mc}}}{V^p_{\text{mc}}}, \tag{3.9}$$

where $\vec{r}_{pq}$ is distance between the macro-cell p and q, $\hat{r}_{pq}$ is the unit vector $\hat{r}_{pq} = \vec{r}_{pq}/r$ and V^p_{mc} is the volume of the macro-cell p with moment $\vec{m}^p_{\text{mc}}$. The first term in Equation 3.9 is the dipole term discussed above arising from the interaction of the cell p with all the other macro-cells in the system. It can be rewritten using the dipolar matrix $\bar{\bar{D}}_{pq}$ presented in Equation 3.4 as:

$$\vec{B}^p_{\text{dip,mc}} = \frac{1}{4\pi} \left[\sum_{p \neq q} \frac{3 \left(\vec{m}^q_{\text{mc}} \cdot \hat{r}_{pq} \right) \hat{r}_{pq} - \vec{m}^q_{\text{mc}}}{r^3_{pq}} \right] = \sum_{p \neq q} \bar{\bar{D}}_{pq} \cdot \vec{m}^q_{\text{mc}}. \tag{3.10}$$

The second term represent the Maxwellian internal field of a sphere and arises from a continuous description. It comes from the contribution to the field of an atomic dipole due to the source of the field itself [38]. In order to achieve agreement with experimental results, the internal field term is applied uniformly to all the spins within the cell as an effective field once the dipolar field is calculated for each macro-cell.

3.3   Inter & intra macro-cell approach

The close proximity of the layers in a MTJ device leads to a significant magnetostatic interaction between the layers and therefore, an accurate description of this contribution is crucial to simulate the properties of these devices. Moreover, if we look at the vertical section of the MTJ stack, we find that the magnetisation is non-uniform when scanning across the different layers. To address these issues, we have modified the previously described bare macro-cell approach for the calculation of the magnetostatic field. The method follows the approach proposed by Bowden *et al.* [44], which allows to calculates the dipole tensor between neighbouring macro-cells with atomistic accuracy and gives an exact representation of the dipole field provided that the atomic magnetic moments within each macro-cell are in perfect alignment. For the systems considered in this

thesis, macro-cell sizes of about $1\,\text{nm}^3$ can reasonably be considered having uniform magnetisation. This method is defined inter & intra macro-cell approach.

The inter & intra macro-cell approach is an extension of the bare macro-cell method and, as such, it is based on discretising the system into regions of uniform magnetisation. Differently from the bare macro-cell method where each macro-cell is approximated as a dipole, in the inter & intra macro-cell approach the dipolar matrix retains the atomic informations in the form of the real-space coordinates. The contribution to the dipole-dipole interaction is separated into two: *a*) one that arises from the interaction of the atomic moments within a macro-cell with the atomic moments in another cell, called inter macro-cell contribution, and *b*) one determined by the interaction among spins within the same macro-cell, defined as the intra macro-cell contribution. Following this method, we can write the dipolar matrix for a macro-cell *p* as summation of the contribution from interactions with magnetic moments in the other macro-cells *q* (inter) and inside the macro-cell *p* (intra). In terms of the field, we can write:

$$\vec{B}^p_{\text{dip,mc}} = \vec{B}^q_{\text{dip}}\,(\text{inter}) + \vec{B}^p_{\text{dip}}\,(\text{intra})$$
$$= \bar{\bar{D}}^{\text{inter}}_{qp} \cdot \vec{m}^q_{\text{mc}} + \bar{\bar{D}}^{\text{intra}}_{pp} \cdot \vec{m}^p_{\text{mc}} \tag{3.11}$$

where $\bar{\bar{D}}^{\text{inter}}_{qp}$ and $\bar{\bar{D}}^{\text{intra}}_{pp}$ are effective dipole-dipole matrices, given by:

$$\bar{\bar{D}}^{\text{inter}}_{qp} = \frac{1}{n_p n_q} \sum_{qj=1}^{n_q} \sum_{pi=1}^{n_p} \bar{\bar{D}}^{\text{inter}}_{qj,pi} \tag{3.12}$$

$$\bar{\bar{D}}^{\text{intra}}_{pp} = \frac{1}{n_p n_q} \sum_{pj \neq pi}^{n_p} \sum_{pi=1}^{n_p} \bar{\bar{D}}^{\text{intra}}_{pj,pi}. \tag{3.13}$$

Here $1 \leqslant pi, pj \leqslant n_p$, $1 \leqslant qj \leqslant n_q$ are the indexes running over the individual atoms within the cells *p* and *q* which enclose n_p and n_q spins, respectively. Despite the fact that $\bar{\bar{D}}^{\text{inter}}_{qp}$ and $\bar{\bar{D}}^{\text{intra}}_{pp}$ do not correspond to real dipole-dipole matrices, their summation is. $\bar{\bar{D}}^{\text{inter}}_{qj,pi}$ and $\bar{\bar{D}}^{\text{intra}}_{qj,pi}$ are dipole-dipole matrices calculated on the real-space atoms coordinates for interactions with other cells and within the same macro-cell, respectively. Since these are dipole-dipole matrices, they have the form of Equation 3.4. Therefore, the dipolar matrix for the interaction between different macro-cells, is given by:

$$\bar{\bar{D}}^{\text{inter}}_{qj,pi} = \frac{1}{4\pi r^3_{piqj}} \begin{pmatrix} 3x^2 - 1 & 3xy & 3xz \\ 3xy & 3y^2 - 1 & 3yz \\ 3xz & 3yz & 3z^2 - 1 \end{pmatrix}, \tag{3.14}$$

where $\vec{r}_{piqj}$ is the distance between the individual dipolar moments at positions $\vec{r}_{pi}$ and $\vec{r}_{qj}$ and (x, y, z) are the unitarian Cartesian components of $\vec{r}_{qj}$. To obtain the intra macro-cell

dipole matrix one just replace qj with pj. In Equation 3.14 we have used the symmetry property of the dipole tensor components according to which the off-diagonal terms are symmetric: $xy = yx$, $xz = zx$ and $yz = zy$. This allows to reduce the independent components of the dipolar tensor from nine to six. We note that an approach to improve the computational efficiency is to scale the distances by the lattice constant of the crystal structure. Moreover, the intra-macro-cell contribution of a cubic lattice is zero if the macro-cell is uniformly magnetised. Because of this, it is possible to improve the efficiency of the calculation provided that the magnetisation is uniform and the moments within the cell are displaced on a cube. Another consequence is that the result differs from the Maxwellian continuum model. Therefore, to recover this limit one should add the self-demagnetisation term discussed in Section 3.2.

This approach works independently of the shape of the macro-cell and the position of the centre of the cell does not affect the calculation because of how the dipole-dipole matrix is calculated. Furthermore, since the dipole-dipole interaction matrix is calculated accounting for the individual atomic positions, the centre of the cells does not need to be shifted. In fact, both the variations in the population of the macro-cell and different atomic moments values are automatically taken into account. It is generally easier to implement an approach where the macro-cell does not change and for most of the systems it does not affect the efficiency of the computation. On the other hand, there are cases where modifying the cubic shape of the macro-cell could result in significant advantages. For instance systems with one of the directions much larger than the others, such as a nanotube. It is worth stressing that the inter & intra macro-cell approach leads to agreement with the dipole-dipole interaction on the atomic scale in case of uniform magnetisation in the macro-cells. Also, it is important to observe that in order to match the criterion of uniform magnetization within a cell, in real systems the macro-cell size should be chosen smaller than the domain wall width.

As noted by Bowden *et al.* [44], both the bare macro-cell model and the inter & intra macro-cell approach yield the same dipolar field for macro-cells whose distance is more than twelve in macro-cell units. This can be exploited in order to simplify the calculation of the magnetostatic interaction. In fact, we can define a cut-off range within which the inter & intra macro-cell method is used, whereas for macro-cells that are outside this range the inter macro-cell term of the dipole-dipole interaction can be replaced by the bare macro-cell calculation. With this approach, thanks to the intra-macro-cell term in particular, it is possible to achieve an accurate description of the dipolar field and dipolar energy for surfaces and irregular shaped regions. Furthermore, given the correctness of the method for uniformly magnetised macro-cells, it would be possible to include this approach as a short-range correction to the magnetostatic field calculation within a

hierarchical scheme, therefore achieving high accuracy and reducing the computational cost of the computation.

3.4 Tests

In order to verify the correct implementation of the calculation of the dipolar interaction according to the inter & intra macro-cell approach, we perform tests against available analytic expressions and the results presented by Bowden *et al.* [44]. Initially, we calculate the atomistic dipole-dipole field for a cubic lattice uniformly magnetised along the *z*-axis. We note that the description would not change if we selected either *x* or *y* as polarisation direction. For a uniformly magnetised cube the sum of the field at the individual sites
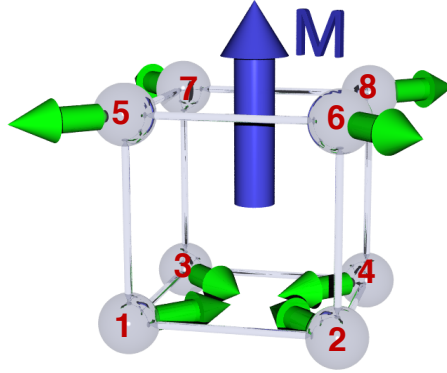
Figure 3.2 Plot of the atomistic dipole-dipole field for a cube on a cubic lattice magnetised along the *z*-axis. The arrow colour palette describes the *z*-component of either the magnetisation, indicated by the central arrow, or the dipolar field (blue for $+z$, red for $-z$, and green for $z = 0$). The atomic sites are described by silver spheres and are indexed by numbers that refer to the dipole matrices below.

yields zero net dipolar field and energy. In Figure 3.2 we plot the dipolar fields (green arrows) for a cube of atomic dipoles that are magnetised along the *z*-axis, shown by the blue arrow at the centre at the system. The total dipole-dipole field of the cube is zero, as one can see by the orientation of the arrows which cancel each other. However, the dipole-dipole field is non-zero at the individual sites. This can be shown by calculating the intra macro-cell term for a cubic system all enclosed in a single macro-cell p. Because $\bar{\bar{D}}_{pp}^{\text{intra}}$ is obtained as the sum of the real-space dipole-dipole $\bar{\bar{D}}_{pj,pi}^{\text{intra}}$ matrices, the individual off-diagonal components cancel out when added to the cell tensor for a cubic lattice. Moreover, the trace of atomic $\bar{\bar{D}}_{pj,pi}^{\text{intra}}$ matrices is zero, and because of the cubic symmetry the diagonal components are isotropic, which result in the trace of $\bar{\bar{D}}_{pp}^{\text{intra}}$ to be zero. The resulting matrices for the cubic atomic sites, where the indexes of the matrices correspond

to those in Figure 3.2, are given in the following:

$$
\sum_{pj \neq pi}^{8} \bar{\bar{D}}_{pj,1}^{\text{intra}} = \sum_{pj \neq pi}^{8} \bar{\bar{D}}_{pj,8}^{\text{intra}} = \frac{1}{4\pi a^3} \begin{pmatrix} 0.0000 & 5.7822 & 5.7822 \\ 5.7822 & 0.0000 & 5.7822 \\ 5.7822 & 5.7822 & 0.0000 \end{pmatrix}
$$

$$
\sum_{pj \neq pi}^{8} \bar{\bar{D}}_{pj,2}^{\text{intra}} = \sum_{pj \neq pi}^{8} \bar{\bar{D}}_{pj,7}^{\text{intra}} = \frac{1}{4\pi a^3} \begin{pmatrix} 0.0000 & 5.7822 & -5.7822 \\ 5.7822 & 0.0000 & -5.7822 \\ -5.7822 & -5.7822 & 0.0000 \end{pmatrix}
$$

$$
\sum_{pj \neq pi}^{8} \bar{\bar{D}}_{pj,3}^{\text{intra}} = \sum_{pj \neq pi}^{8} \bar{\bar{D}}_{pj,6}^{\text{intra}} = \frac{1}{4\pi a^3} \begin{pmatrix} 0.0000 & -5.7822 & 5.7822 \\ -5.7822 & 0.0000 & 5.7822 \\ 5.7822 & 5.7822 & 0.0000 \end{pmatrix}
$$

$$
\sum_{pj \neq pi}^{8} \bar{\bar{D}}_{pj,4}^{\text{intra}} = \sum_{pj \neq pi}^{8} \bar{\bar{D}}_{pj,5}^{\text{intra}} = \frac{1}{4\pi a^3} \begin{pmatrix} 0.0000 & -5.7822 & -5.7822 \\ -5.7822 & 0.0000 & 5.7822 \\ -5.7822 & 5.7822 & 0.0000 \end{pmatrix} \tag{3.15}
$$

and by inspection we can see that the net intra macro-cell $\bar{\bar{D}}_{pp}^{\text{intra}}$ is zero:

$$
\bar{\bar{D}}_{pp}^{\text{intra}} = \frac{1}{4\pi a^3} \begin{pmatrix} 0.0000 & 0.0000 & 0.0000 \\ 0.0000 & 0.0000 & 0.0000 \\ 0.0000 & 0.0000 & 0.0000 \end{pmatrix}. \tag{3.16}
$$

If the magnetisation is uniform, the intra-macro-cell term is always zero for each inter-action due to the cubic symmetry of the system and the contribution to the dipolar field arises from the inter macro-cell terms only. Our results agree with those reported by Bowden *et al.* [44] for an analogous system.

Afterwards, we calculate the dipole-dipole energy dependence on the direction of the magnetisation for a 2D elongated system and we compare it with the results obtained by Bowden *et al.* [44]. The simulated system is plotted in the inset of Figure 3.3, where a group of eight spins (silver balls) is divided in two macro-cells (blue arrows) that enclose four atoms each. Figure 3.3 shows the comparison between ours and Bowden *et al.* [44] results for the variation of the dipolar energy when the spins are coherently rotated from a perpendicular direction, aligned along the *z*-axis and corresponding to the azimuthal angle $\vartheta = 0°$ to the in-plane direction ($\vartheta = 90°$), for two different orientation of the polar angle φ: *a*) along the *zx*-plane ($\varphi = 0°$) and *b*) along the *zy*-plane ($\varphi = 90°$). Because the two directions are not equivalent, the energies will differ. This is also clear from the
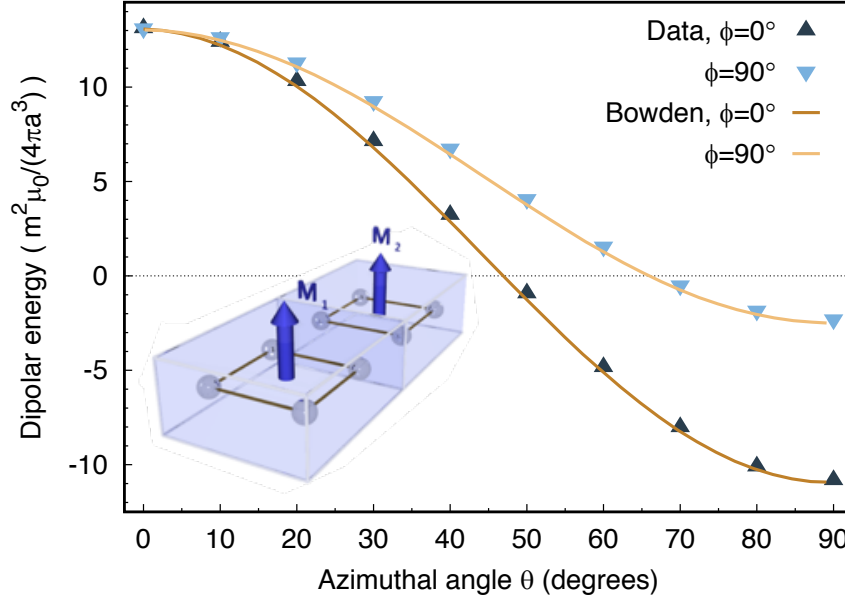
Figure 3.3 Plot of the comparison between our calculations (points) and the results presented by Bowden *et al.* [44] (lines) for the dipolar energy versus the azimuthal angle ϑ for two different orientation of the polar angle $\varphi = 0°$ (blue upwards triangles, brown line) and $\varphi = 90°$ (light-blue downwards triangles, yellow line) for a system of eight magnetic moments on a square lattice, as shown in the inset. The atomic sites are indicated by silver balls and the atoms within a macro cells are connected by brown lines. The two macro-cells are represented by light-blue boxes and their respective macro-moment M_1 and M_2 by two blue arrows at the centre of the cell. The energy is plotted in units of $m^2\mu_0/4\pi a^3$, where m are the individual atomic moments and a is the lattice constant.

intra and inter macro-cell dipolar matrices:

$$\bar{\bar{D}}_{11}^{\text{intra}} = \qquad \bar{\bar{D}}_{22}^{\text{intra}} = \frac{1}{4\pi a^3}\begin{pmatrix} 2.3536 & 0 & 0 \\ 0 & 2.3536 & 0 \\ 0 & 0 & -4.7071 \end{pmatrix}$$

$$\bar{\bar{D}}_{12}^{\text{inter}} = \qquad \bar{\bar{D}}_{21}^{\text{inter}} = \frac{1}{4\pi a^3}\begin{pmatrix} 3.0550 & 0 & 0 \\ 0 & -1.2039 & 0 \\ 0 & 0 & -1.8511 \end{pmatrix}, \qquad (3.17)$$

where we remark that the two macro-cells provide the same contribution. As we can see from Figure 3.3 and from the comparison of the dipolar matrices, our data show an excellent agreement with the results in literature, managing to reproduce the two different trends accurately.

The last test we present is the comparison between the calculated demagnetisation factors of ellipsoids as function of different aspect ratio, i.e. the ratio between the

two major axes, and the analytic expressions derived by Osborn [24]. In a mean field description, an approach that can be applied when the magnetisation of a system is uniform, the magnetostatic field $\vec{H}_{mf}$ of a uniformly magnetised body is assumed to be proportional to the mean magnetisation of the system ($< \vec{M} >$). Hence, we can write:

$$\vec{H}_{mf} = \bar{\bar{N}} < \vec{M} >,$$ (3.18)

where $\bar{\bar{N}}$ is the demagnetisation tensor that in Cartesian coordinates can be expressed as:

$$\bar{\bar{N}} = \begin{pmatrix} N_{xx} & N_{xy} & N_{xz} \\ N_{yx} & N_{yy} & N_{yz} \\ N_{zx} & N_{zy} & N_{zz} \end{pmatrix}.$$ (3.19)

$\bar{\bar{N}}$ depends on the shape and geometry of the sample and for general systems analytic expressions do not exist. Moreover, the components of the tensor can be non-uniform. For the particular case of an ellipsoid of revolution, the magnetostatic field inside the body is uniform and only the diagonal components of $\bar{\bar{N}}$ are non-zero. Osborn derived an analytic description of $\bar{\bar{N}}$ for the case when two of the three semi-axes are identical. For an ellipsoid magnetised along the z-direction, corresponding to the semi-axis c, and the other two semi-axes $a = b$ aligned along the x and y axes, respectively, the component of $\bar{\bar{N}}$ along the magnetisation direction N_{zz} can be expressed as function of the aspect ratio $k_0 = c/a$ as:

$$\begin{aligned} N_{zz} &= \frac{1}{1-k_0^2} \left[1 - \frac{k_0}{\sqrt{1-k_0^2}} \arccos(k_0) \right] && \text{for } k_0 < 1 \\ N_{zz} &= \frac{1}{3} && \text{for } k_0 = 1 \\ N_{zz} &= \frac{1}{k_0^2-1} \left[\frac{k_0}{\sqrt{k_0^2-1}} \operatorname{arcosh}(k_0) - 1 \right] && \text{for } k_0 > 1 \end{aligned}$$ (3.20)

The other two diagonal components of $\bar{\bar{N}}$ can be obtained by the symmetry relation $N_{xx} + N_{yy} + N_{zz} = 1$ in SI.

Since the mean field theory is based on the continuum approach, to compare our results with the analytic model available, we include the self-demagnetisation term discussed in Section 3.2 in our calculations. Figure 3.4(a) presents the comparison between the calculated demagnetisation component N_{zz} (dots) for a uniformly magnetised ellipsoid of revolution with semi-axis $c = 10\,\mathrm{nm}$ and those obtained by Osborn's relations (line) as function of different macro-cell size. The simulated data is in excellent agreement with the analytic expressions, showing that the approach allows to calculate accurately the magnetostatic contribution independently of the macro-cell size as long as the magnetisation inside the body is uniform. We also compare the results obtained using the inter
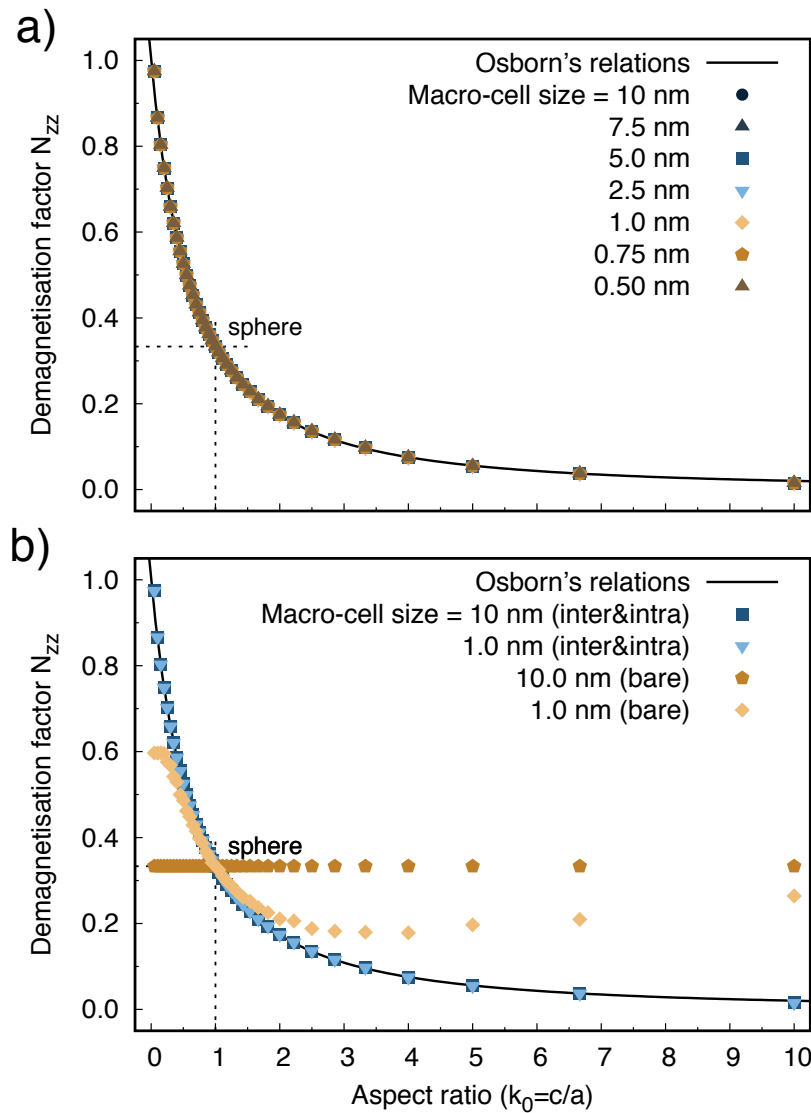
Figure 3.4 (a) Comparison of the computed (points) demagnetization factor N_{zz} of an ellipsoid as function of the aspect ratio for different macro-cell size with the analytics expressions (line) provided by Osborn. (b) Comparison between computed demagnetisation factor N_{zz} with the inter & intra macro-cell approach (blue and light-blue points) and with the bare macro-cell method (brown and yellow points). The line represents Osborn's relations and the point $(1/3)$, value obtained for a sphere, is marked on both plots by the intersection of black dotted lines.

& intra macro-cell approach with simulations performed with a bare macro-cell method for two different macro-cell dimensions, presented in Figure 3.4(b). Whilst the former approach does not depend on the macro-cell size as the magnetisation of the ellipsoid is uniform, the N_{zz} component of $\bar{\bar{N}}$ strongly varies as function of the cell used to discretise the system in the latter. Furthermore, in none of the cases the bare macro-cell method

is able to reproduce the analytic trend. When the macro-cell is as large as the system, the only contribution to the dipolar field arises from the self-demagnetisation term in the bare macro-cell method. This is because the information of how the moments are displaced inside the cell is neglected, except for the calculation of the position of the centre of the cell. Therefore, it is not surprising that N_{zz} is constant and equal to $1/3$, the value for a sphere. As we reduce the size of the macro-cell down to $1\,\mathrm{nm}$, the N_{zz} calculated with the bare macro-cell method approaches the expected values in a range $0.5 < k_0 < 1.5$, as the macro-cell are more densely populated. However, for larger and smaller k_0 the self-demagnetisation term becomes the dominant contribution and N_{zz} approaches a constant value. The tests demonstrate the improvement in the accuracy of the magnetostatic interactions calculation provided by the inter & intra macro-cell approach with respect to the bare macro-cell method. It is worth mentioning that this refinement comes at the cost of a longer computing time and larger memory requirement. In fact, the calculation of the dipolar matrix is performed with atomistic accuracy and the positions of the moments within a macro-cell need to be stored.

The macro-cell approaches present limitations due to the discretisation in macro-cells and the requirement of uniform magnetisation within these. Random thermal fluctuations are a source of non-uniformity for the magnetic configuration, hence small macro-cell dimensions need to be used at finite temperature. Systems with complex crystal structures represent a challenge for the calculation of magnetostatic interactions. A material such as the permanent magnet NeFeB is characterised by a unit cell where hexagonal-like Fe clusters are sandwiched between N and B planes [45] and the lattice constant extends for more than a nanometre. In these materials the different planes do not behave uniformly necessarily. Besides, the macro-cell size should be smaller than the domain wall size, which is around few nanometres for NeFeB systems, to ensure an accurate description of the dipolar interaction. One could use a small macro-cell of few Angstroms, but this would add a large computational cost to the simulations. The requirement of uniform magnetisation is hardly met in magnetic systems that are intrinsically non uniform at the atomic level as antiferromagnets and ferrimagnets. An atomistic dipole-dipole calculation would allow to preserve the detailed information as it accounts for the different orientations and magnitudes of the magnetic moments. However, such simulations are feasible for small systems only. Therefore, more complex and elaborated methods need to be developed to deal with the limitations just described.

3.5   Conclusions

In this chapter we presented the bare macro-cell model to calculate the magnetostatic interactions in an atomistic modelling based on a micromagnetic discretisation of the system in regions of uniform magnetisation (macro-cell). These cells, whose magnetisation is given by the contribution of the atomic spin moments contained inside, are considered as dipoles and the magnetostatic field is calculated as sum of the interactions between these cells. We discussed the implementation of an improved model, called inter & intra macro-cells approach, that accounts for the atomic detail inside each macro-cell. This method is based on the work by Bowden *et al.* [44] and allows to obtain agreement with an atomistic dipole-dipole approach for bodies with uniform magnetisation. We presented tests we performed to verify the correct of implementation of the approach and we showed the improved calculation of the dipolar field with respect to the bare macro-cell approach. Finally, we discussed the main limitation that the macro-cell approaches are subjected to.

Chapter 4

Description of the magnetic properties of CoFeB/MgO systems

In the following, we present the main parameters that characterise the investigated CoFeB/MgO-based MTJs. We first discuss the general properties of these systems, such as the high interfacial anisotropy, low damping and low saturation magnetisation. Afterwards, we present the parametrisation we adopted in our simulations, we discuss the source of our parameters and show that these parameters lead to the desired properties. Finally, we discuss the effect of finite size on the magnetic properties of CoFeB/MgO systems.

4.1   CoFeB/MgO properties

CoFeB/MgO-based MTJs are among the most promising candidates for MRAM devices because of the high thermal stability, low damping and high tunnel magneto resistance [1–3]. For this reason, CoFeB/MgO structures are the choice of materials in this thesis. CoFeB is an alloy of Cobalt and Iron with Boron doping. Even though CoFeB layers grow with an amorphous structure naturally, when annealed the layers crystallise into a bcc (001) texture imposed by the MgO underneath [46]. Co-Fe alloys are characterised by the highest saturation magnetisation, around $2.3 - 2.5\,\mathrm{T}$ [47, 48], as described by the Slater-Pauling curve [49], which gives the atomic magnetic moment per atom as function of the number of $3d$ electrons per atom. Experimental measurements [50] show that when CoFeB/MgO-based films for MTJs are grown, a significant reduction in the magnetisation of the CoFeB layers occurs. The physical origin of the reduced saturation magnetisation is likely due to a combination of effects, such as the presence of non-magnetic Boron, structural defects, dead layers, granularity at the CoFeB/MgO interface [51] and non-collinear interfacial spin structures. Another appealing magnetic property of CoFe(B) is

the low Gilbert damping, required to achieve fast switching and low switching current. CoFe is an alloy of light elements and as such is characterised by a weak spin-orbit coupling. This yields a low Gilbert damping and at the same time a weak in-plane bulk magneto-crystalline anisotropy [50, 52]. Experimental studies [50, 53] reported an increase of the Gilbert damping when the thickness of the CoFeB film is reduced and recent studies confirm an increase close to the interface up to 0.11 due to effects of spin-pumping induced by the tantalum, magnon scattering and increase of spin-orbit coupling at the interface with MgO. In CoFeB/MgO systems the perpendicular anisotropy has an interfacial origin: it arises from the hybridisation of the atomic orbitals between the magnetic layer and the Oxygen orbitals at the ferromagnet/non-magnet interface [1, 54, 55]. The total anisotropy K_{tot} is given by the competition of the perpendicular interfacial term, the weak in-plane bulk anisotropy and the in-plane shape anisotropy. To show that CoFeB/MgO thin films have perpendicular anisotropy of interfacial origin, we can rewrite [50] Equation 2.10 to include the contribution $-\mu_0 M_s^2/2$ arising from the shape anisotropy:

$$K_{tot} = K_b - \frac{\mu_0 M_s^2}{2} + \frac{K_i}{t}, \tag{4.1}$$

where K_b is the bulk anisotropy of magneto-crystalline origin only, K_i the interfacial anisotropy, M_s the spontaneous magnetisation and t the ferromagnet thickness. Taking $M_s \sim 1.6\,T$, $K_b \sim$ negligible and $K_i \sim 1.3 \times 10^{-3}\,Jm^{-2}$ from Ikeda *et al.* [50], one can see as CoFeB/MgO has a perpendicular anisotropy for thickness around $1.0 - 1.5\,nm$. This interfacial anisotropy provides the necessary thermal stability, i.e. the energy barrier that separates the two stable low energy states of the system, to store the information.

One of the main reasons MgO was introduced as non-magnetic spacer in MTJ stacks instead of amorphous AlO is the fact that when crystallised with (001) texture it allows to achieve a large TMR ratio. In the case of an amorphous tunnelling barrier, electronic states characterised by different symmetries can incoherently tunnel through the barrier because of the absence of a specific crystal symmetry. Hence, all these states contribute to the net spin-polarisation of the current independently of the initial symmetry. If the spin-polarisations are different, the net spin-polarisation of the current exiting the barrier will be reduced. In the case of a crystalline barrier, the symmetry of the electronic wave function can be preserved during the tunnelling, an effect defined as coherent tunnelling. Therefore, MgO allows to achieve a high spin-polarisation of the current through the junction, which results in high TMR ratio [1, 13, 14, 56, 57].
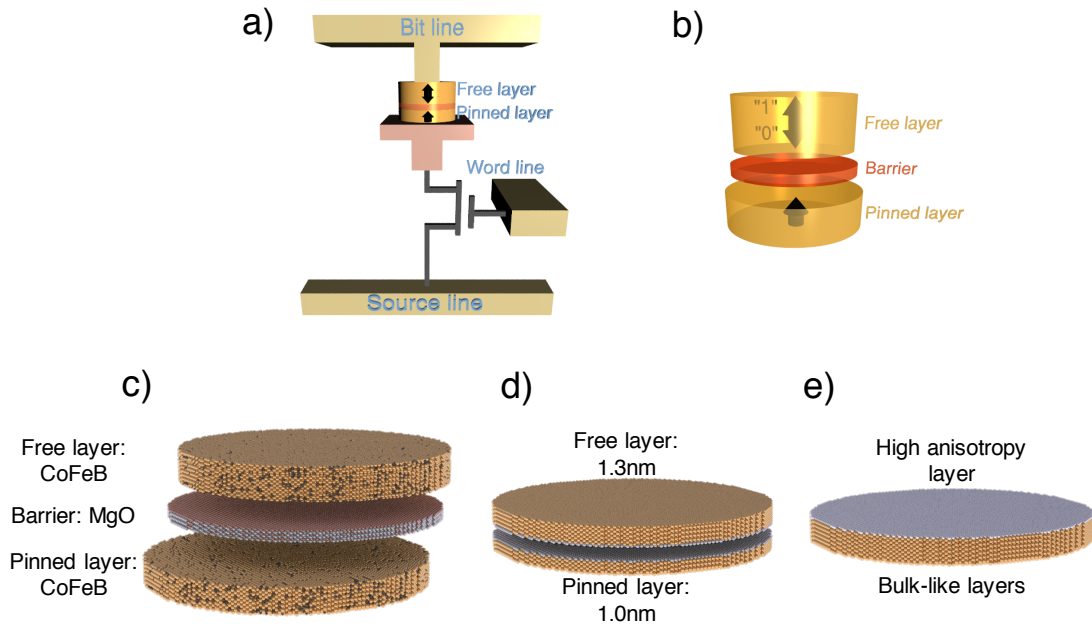
Figure 4.1 Sketch of STT-MRAM (a) and MTJ (b). Schematic of a CoFeB/MgO/CoFeB MTJ is presented in (c), where gold spheres refer to CoFe, Boron impurities are indicated by black spheres and MgO is described by grey and red spheres. In (d) and (e) the schematic of the simulated MTJ and single CoFeB/MgO dot is presented, respectively. The high anisotropy layer is indicated by silver spheres, whereas gold spheres represent the bulk-like CoFeB layer with negligible anisotropy.

4.2 Parametrisation of the system

To simulate CoFeB/MgO/CoFeB MTJs, we consider an idealized model where all of the magnetic anisotropy is provided by a single monolayer of CoFeB in contact with the non-magnetic MgO and the other layers contribute with no anisotropy. The anisotropy is assumed of single-ion uniaxial type, although recent studies suggest the presence of a two-ion contribution [58–60]. The elemental properties of Fe, Co and B are not considered, but treated as an average magnetic material with zero anisotropy since CoFeB is a random alloy, i.e. the lattice sites are randomly occupied by one of the species of the compound. The atomic structure of CoFeB is modelled as a bcc lattice with lattice constant 2.86 Å and the bulk bcc crystal is cut into the shape of a cylinder of thickness 1.0 and 1.3 nm, representing the pinned layer (PL) and free layer (FL) of the MTJ, respectively. Figure 4.1 shows the investigated systems. The two ferromagnets are separated by a thin MgO barrier 0.85 nm thick which is not included in the simulations explicitly as it does not contribute directly to the magnetic behaviour of the system. Since *ab-initio* studies suggest that MgO induces a strong interfacial perpendicular anisotropy at the interface between CoFeB and MgO [61] and that enhances the exchange coupling of Fe and Co sites at the
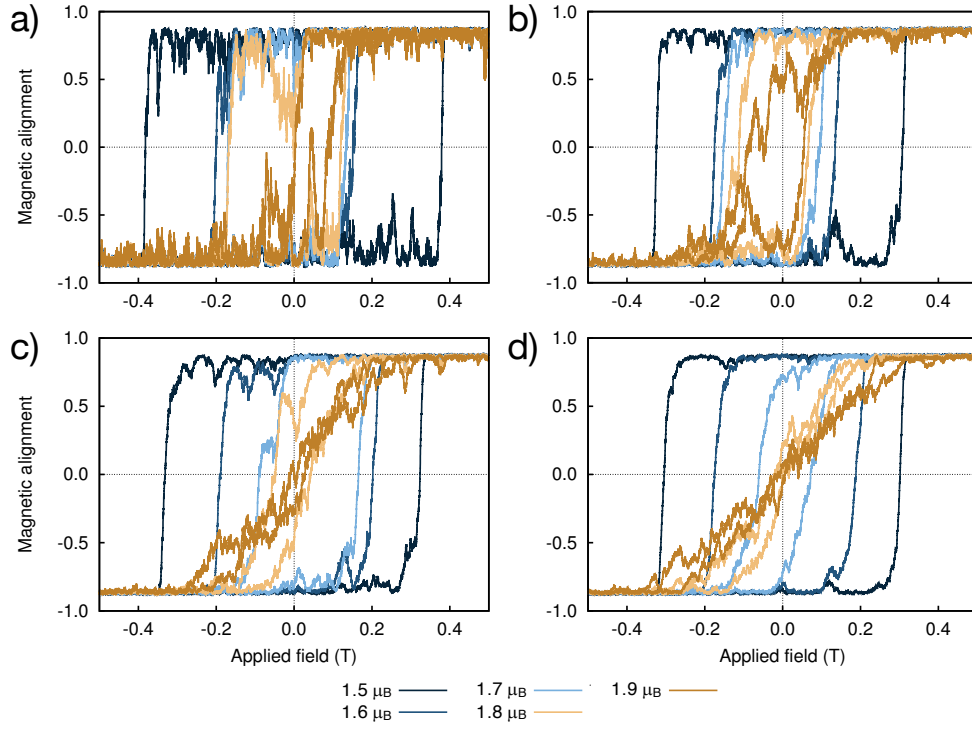
Figure 4.2 Hysteresis loops performed at room temperature for nanodots of thickness 1.3 nm and diameter 10 (a), 20 (b), 30 (c), 40 nm (d) as function of atomic magnetic moment (μ_s), from 1.5 to 1.9 μ_B. Colours refer to different moment values.

same interface [62], we model these properties using effective anisotropy and exchange parameters obtained from direct comparison with experiments [59]. The atomic spin moment used in our simulations is $\mu_s = 1.6 \, \mu_B$ which corresponds to $M_s \sim 1.3 \, \mathrm{MAm}^{-1}$ or $\mu_0 M_s \sim 1.6 \, \mathrm{T}$. This value is obtained from the relation [43]:

$$\mu_s = \frac{M_s a^3}{n_{uc}}, \tag{4.2}$$

where a is the lattice constant and n_{uc} the number of atoms in the unit cell, with $n_{uc} = 2$ for a bcc lattice. This M_s value is close to the value measured by Ikeda *et al.* [50], but significantly lower than expected in bulk [47, 48]. In order to ensure that the system is out-of-plane magnetised for the considered thickness [50, 54, 63–68], we perform hysteresis loop simulations varying the atomic moments, presented in Figure 4.2. The results show that an atomic magnetic moment lower than 2 μ_B is required to achieve perpendicular orientation of the magnetisation. This effect we observe in the simulations is caused by a reduction in the in-plane demagnetisation field for lower moments.

A list of the parameters used to simulate CoFeB/MgO systems is reported in Table 4.1. The exchange energy constants J_{ij} are obtained from a mean-field approximation which

Table 4.1 Simulation parameters for the investigated systems.

	CoFeB(@interface)	CoFeB(bulk)	Unit
J_{ij}	1.547×10^{-20}	7.735×10^{-21}	J link^{-1}
μ_{s}	1.6	1.6	μ_{B}
k_{u}	1.35×10^{-22}	0.0	J atom^{-1}
α[1]	0.11	0.003	

gives:

$$J_{ij} = \frac{3k_{\mathrm{B}}T_{\mathrm{c}}}{\varepsilon z}. \tag{4.3}$$

k_{B} is the Boltzmann constant, T_{c} is the Curie temperature, z the number of nearest neighbours and ε is a correction due to spin waves excitations [43, 29]. The value of T_{c} is obtained from CoFeB/MgO thin films measurements performed by Sato *et al.* [59], $z = 8$ is used to determine the bulk J_{ij}, while $z = 4$ for the interface layer due to the reduced coordination. The anisotropy energy constants k_{u} is derived from experimental measurements of the temperature dependence of the anisotropy energy density K_{u} of CoFeB/MgO thin films by Sato *et al.* [59] via [43]:

$$k_{\mathrm{u}} = \frac{K_{\mathrm{u}}a^3}{n_{\mathrm{uc}}}, \tag{4.4}$$

where the same formalism of Equation 4.2 is used.

4.3 Temperature dependence of the magnetisation

An important property that characterises a magnetic system is the spontaneous magnetisation and its temperature dependence. For a system such the one we are interested in, where the exchange coupling J_{ij} is orders of magnitudes larger than the anisotropy k_{u}, the temperature dependence of $M_{\mathrm{s}}(T)$ is determined by the exchange mainly. Since the magnetisation is a macroscopic equilibrium property, we calculated it using a Hinzke-Nowak Monte Carlo (MC) algorithm [43], which makes use of different trial moves to allow a more efficient relaxation towards thermal equilibrium. Figure 4.3(a) shows the temperature dependence of the reduced spontaneous magnetisation $M_{\mathrm{s}}(T)/M(T = 0\,\mathrm{K})$ of a CoFeB/MgO dot of dimensions $40\,\mathrm{nm} \times 40\,\mathrm{nm} \times 1\,\mathrm{nm}$. Fitting the data with the

---

[1]This value has been used to simulate the magnetisation dynamics in absence of external field or when studying the spin-torque dynamics, while a critical damping has been used in hysteresis loop simulations.
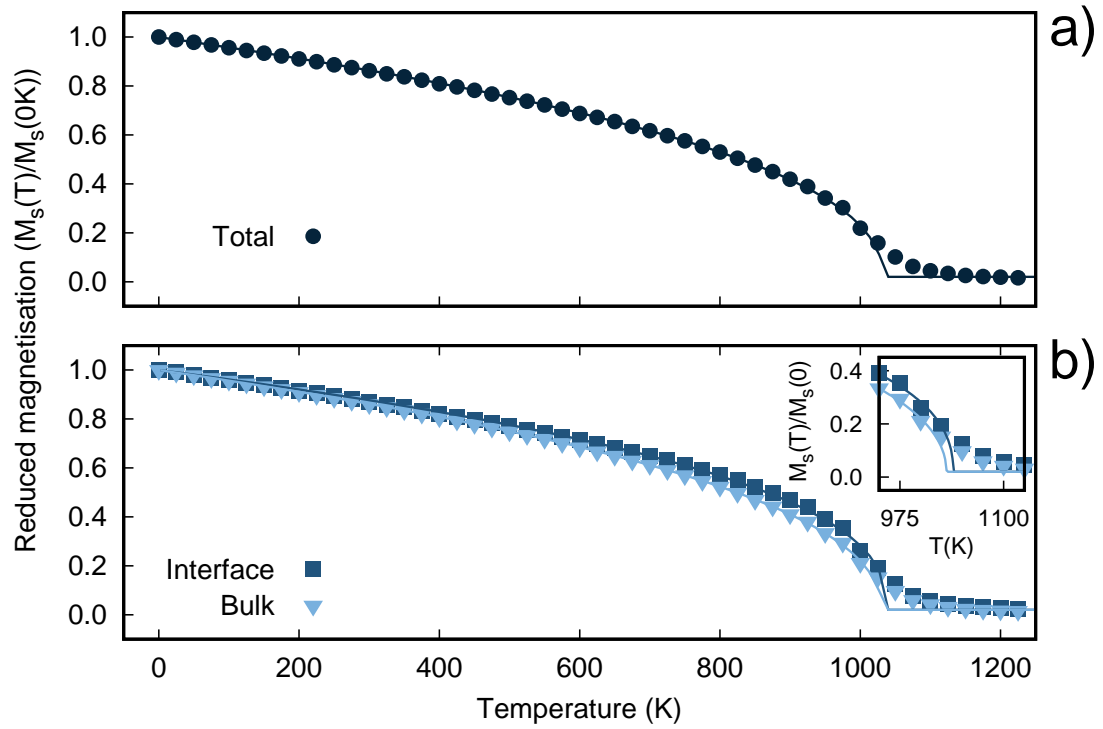
Figure 4.3 Simulated temperature dependence of the reduced saturation magnetisation $M_s(T)/M(T=0\,\mathrm{K})$ for a CoFeB/MgO disc of dimensions $40\,\mathrm{nm} \times 40\,\mathrm{nm} \times 1\,\mathrm{nm}$ for (a) total system and (b) as function of interfacial and bulk components. A zoom of the region $950\,\mathrm{K} < T < 1125\,\mathrm{K}$ is presented in the inset of (b). Lines represent the fit of the data following the equation $(1 - T/T_c)^\beta$, where T_c is the Curie temperature and β a critical exponent.

equation for a classical spin

$$\frac{M_s(T)}{M_s(T=0K)} = \left(1 - \frac{T}{T_c}\right)^\beta ,$$ (4.5)

we find $T_c \sim 1030\,\mathrm{K}$ and the critical exponent $\beta \sim 0.4$. The obtained T_c is lower than in bulk CoFe, whereas the gradient of the magnetisation is larger than expected for a classical spin system. At the interface the loss of coordination yields larger fluctuations of the magnetisation, which can affect the temperature dependence of the anisotropy as this has interfacial origin in the system. On the other hand, the enhanced exchange coupling of the atoms at the interface leads to a larger T_c and criticality close to T_c. These effects tend to oppose each other [62], as shown in Figure 4.3(b).

4.4   Conclusion

The main properties characterising the investigated CoFeB/MgO-based MTJs as well as the simulated systems have been presented and discussed in the chapter. We described the principal features of the CoFeB/MgO-based systems such as the high interfacial anisotropy, low damping and low saturation magnetisation. We presented the parametrisation of these properties used to perform the simulations. We verified that the chosen parameters yield good agreement with experimental results and we showed how finite size and surface effects can affect the magnetic properties of CoFeB/MgO structures.

Chapter 5

Thermally nucleated field-driven switching in CoFeB/MgO systems

The importance of thermal effects on the dynamics of the magnetisation and reversal mechanism in CoFeB/MgO nanodots and MTJs will be discussed in this chapter. Initially, we investigate the thermal effects on the switching mechanism and on the coercive field, then we focus on how these properties vary depending on the size of single CoFeB/MgO systems. Once the properties of the individual layers have been fully characterised, we study the dynamics of the whole MTJ stack.

The magnetisation reversal is incoherent for in-plane dimensions larger than 30 nm and the switching of the magnetisation is thermally driven with edge nucleation and propagation of a domain. Nucleation comports lower coercive fields than in the case of co-herent reversal. Besides, the thermal nature of the switching mechanism poses an intrinsic limitation to the deterministic reversal process and reduces the thermal stability for small devices. The majority of the results discussed in this chapter is presented in reference [69].

5.1   Magnetisation dynamics

The magnetisation dynamics affects the thermal stability of the system, the switching properties under an applied field as well as induced by an electrical current. Therefore, the dynamic properties need to be fully investigated and understood in order to achieve further developments. The most simple approach to describe the dynamics of the mag-netisation is to assume that all the spins within the system behave coherently, i.e. they behave as a macrospin [70]. It turns out that this approach is too simplistic for describing correctly such structures, that are characterised by finite size and surface effects and operate at a finite temperature. Previous experimental [63, 71, 72] and micromagnetic

studies [73–75] have concluded that the reversal mechanism is likely to be incoherent due to the large lateral size of the devices. However, the nature of the reversal mechanism and in particular the effects of the temperature and of the anisotropy arising at the CoFeB/MgO interface are not clear yet. In micromagnetism the smallest cell size which a system can be discretised in is about $1\,nm^3$. Consequently, the simulation of materials and multilayer structures that have a dimension of the same order of the cell size, cannot take into account the atomic variation of the properties, as it occurs for the anisotropy in CoFeB/MgO multilayer stacks that is localised at the interface between CoFeB and MgO. Micromagnetism tends to underestimate the reduced coordination and loss of exchange bonds occurring at surfaces and interfaces which cause a lower exchange than in bulk. Moreover, finite temperature effects are poorly described because atomic spin fluctuations are neglected and finite size effects cannot be properly captured. Not to be constrained by micromagnetic limitations, we investigate the dynamics of CoFeB/MgO nanodots and MTJs using an atomistic spin model.

5.2   Hysteresis loop simulation parameters

In hysteresis loop calculations, the damping is set to its maximum value of one, referred to as critical damping value. This allows a faster relaxation of the magnetisation than it would occur if the simulations were performed with the natural low damping of CoFeB. The field is applied along the perpendicular direction to the disc and it is swept back and forth at a rate of $0.3\,Tns^{-1}$. The complete hysteresis cycle lasts over $20\,ns$, which allows to reduce the effects of enhanced coercivity caused by fast field sweep rates. It is worth noting that the rate is still faster than experimental measurements. Because of this, our results are characterised by larger coercive field values than observed in experiments.

5.3   Thermal effects

We first consider the effects of temperature on the typical hysteresis properties of a nanodot with a diameter of $50\,nm$, as shown in Figure 5.1(a). The first observation is that increasing the temperature leads to a large reduction of the coercivity: from $1.1\,T$ at $5\,K$ to $0.6\,T$ at $300\,K$. The temperature variation of intrinsic properties such as the saturation magnetisation and magnetic anisotropy arises naturally from the atomistic simulations and are calculated using Monte Carlo methods as outlined in Chapter 2 and Chapter 4. This leads to an expected 20% reduction of H_K between zero and $300\,K$. However, we observe a 45% reduction of the coercivity. This is partially due
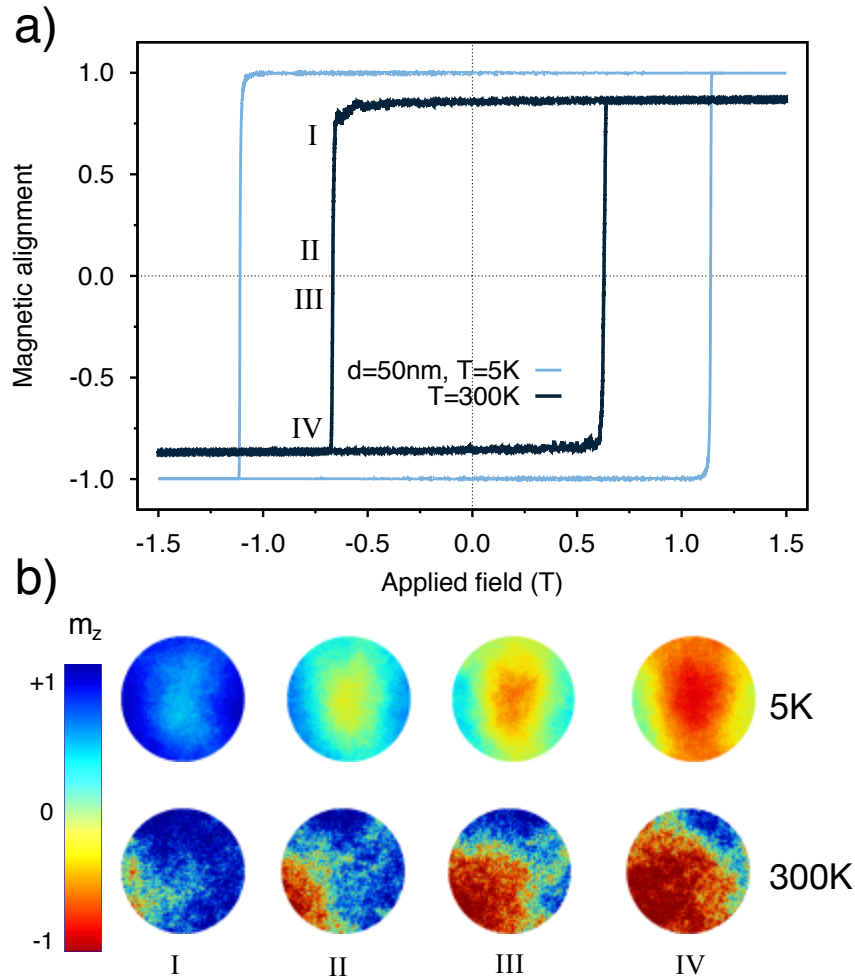
Figure 5.1 (a) Typical simulated easy-axis hysteresis loop for 1 nm thick, 50 nm diameter nanodot at temperatures of 5 K and 300K. The data show a large reduction of the coercivity for elevated temperatures due to increased thermal fluctuations, indicating a change in the magnetic reversal mechanism. (b) Snapshots of magnetisation reversal presented in (a). I and IV refer to the top and bottom shoulder of M/M_s vs applied field curve, respectively. II and III are configurations just before and after the switching, respectively. The colour scheme represents the magnetisation along the easy axis direction (z).

to the thermally activated transitions over the energy barrier, but it may also reflect a change in the magnetic reversal mechanism due to the stronger thermal fluctuations. To investigate the reversal mechanisms we have generated snapshots of the atomic spin configuration during the hysteresis loop for different temperatures, as shown in Figure 5.1(b). At a temperature of 5 K the reversal is nucleated at the centre of the nanodot due to the larger magnetostatic field and the weak thermal contribution. This highlights the importance of an accurate calculation of the magnetostatic coupling. At 300 K the reversal is initiated by the nucleation of a small reversed domain at the edge of

the nanodot caused by thermally driven spin fluctuations. At the edge, loss of exchange bonds leads to larger edge spin fluctuations compared with the spins in the middle of the dot. These larger spin fluctuations provide a natural nucleation region at the edges of the nanodot and allow a different reversal mechanism compared to the centre nucleated reversal at low temperatures. Interestingly, the small size of the system means that the thermal fluctuations are more important than the variation in the magnetostatic field across the dot diameter. This stresses the importance of including thermal fluctuations and surface effects in the model, which represents a limitation for non-stochastic continuum micromagnetic simulations. Due to the two different nucleation processes at low and high temperatures, the time that is required to reverse the magnetisation varies in the two temperature limits. The switching results faster at 5 K since the reversal proceeds almost coherently in regions around the central nucleation site.

We note that the thermally nucleated switching we describe here is different from the Sharrock approach [76]. Sharrock considers a fixed (coherent) reversal mechanism with a time dependence of the magnetisation due thermally induced transitions over the energy barrier. In the case of CoFeB/MgO dots, thermal fluctuations lead to a large reduction of the coercivity due to the ability to access a different thermally driven reversal mode. Slower hysteresis loops will likely lead to a further reduction in the coercivity similarly to Sharrock due to the increased number of nucleation attempts, but such simulations are currently beyond the time-scales accessible with atomistic models. Another interesting feature of the hysteresis loop at 300 K in Figure 5.1(a) is a slight asymmetry in the coercivity of the ascending and descending branches of the loop. This is due to the thermally nucleated nature of the reversal, which leads to an uncertainty in the exact coercivity value due to the randomness of the nucleation attempts. Therefore, there is an intrinsic *thermal* switching field distribution which is independent of defects and variations in the intrinsic properties, but arises solely due to random thermal fluctuations. For larger systems and long time-scales the thermal switching field distribution is not apparent. Nonetheless, for nanoscale MTJs switching in the nanosecond time domain it is a real and important effect and represents the thermodynamic limit of the switching field distribution, which cannot be overcome.

5.4   Size effects

To investigate the effects of nanodot size and temperature on the coercivity and thermal switching field distribution we perform a systematic study of the hysteretic properties for 1 nm and 1.3 nm thick nanodots, shown in Figure 5.2. The size dependence of the coercivity is obtained by averaging over a minimum of 30 independent loops for each

size, temperature and thickness. The mean coercivity shows a complex temperature and
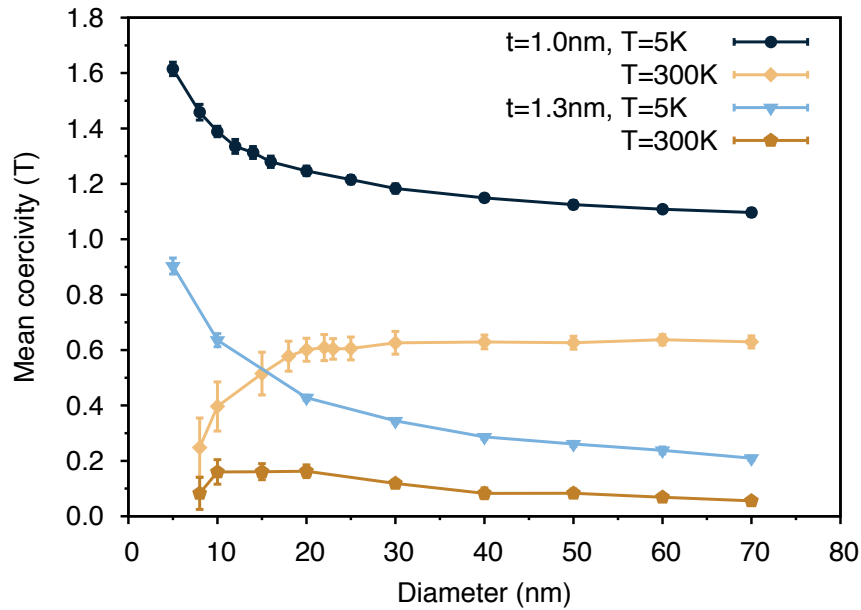
Figure 5.2 Mean coercivity of CoFeB/MgO nanodots as function of disk diameter for thicknesses of 1.0 nm and 1.3 nm at 5 K and 300 K. Error bars show the standard deviation of the statistical distribution. The data show a constant size dependence for diameters larger than 30 nm because of domain nucleation as reversal mechanism. For smaller diameters, the system becomes thermally unstable and the coercivity reduces at room temperature, while low temperature results in larger stability.

size dependence which is due to different reversal mechanisms and finite size effects. First, we consider the 1 nm thick nanodots. The coercivity reaches an asymptotic limit for nanodot diameters larger than 20 nm, that is indicative of a nucleation reversal mode at 300 K. The snapshots of the atomic spin configurations support the earlier conclusion of different reversal modes at low and room temperature. At 5 K the nucleation is driven by the variation of the magnetostatic field across the nanodot. This effect increases with the nanodot diameter and leads to a slow convergence towards a constant nucleation field, which is seen for larger nanodot diameters. Conversely, at 300 K the coercivity reaches an asymptotic limit at around 20 nm diameter as the thermal nucleation volume is much smaller and independent of the dot size. The behaviour of both the temperature regimes can be identified in Figure 5.3, where the diameter dependence of the average coercivity for 1 nm systems at 5 K and 300 K obtained up to a diameter of 100 nm is presented. For dots with a diameter smaller than 20 nm, the temperature has a dramatic effect on the coercivity. We observe a large increase at 5 K and decrease at 300 K. For low temperatures the increase in the coercivity with decreasing diameter indicates a transition to coherent reversal. The magnetostatic field no longer dominates the reversal process and
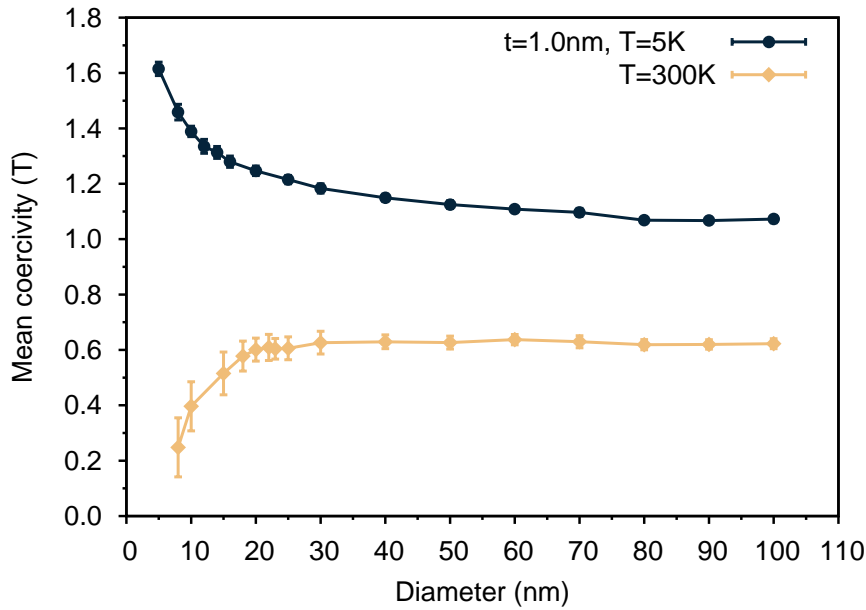
Figure 5.3 Mean coercivity as function of disk diameter for nanodots of thickness of 1 nm at 5 K (black dots) and 300 K (yellow diamonds). Error bars show the standard deviation of the statistical distribution.

the nanodot size approaches the single domain limit $\delta_w = \pi \sqrt{A_s/K_{eff}} \sim 15\,\text{nm}$, where A_s is the exchange stiffness and K_{eff} the effective anisotropy energy density. Figure 5.4 (a) shows the hysteresis loops at 5 K and 300 K for 10 nm dots. A net reduction of the coercivity at room temperature emerges compared with 50 nm dots. We also find a larger thermal contribution, which results in a pronounced asymmetry of the two branches and increase in the noise. As observed in the case of larger dots, the hysteresis loops obtained at 5 K are symmetric and the thermal fluctuations of the magnetisation are negligible. At room temperature the reduction of the coercivity is due to superparamagnetic fluctuations of the magnetisation which, due to the small volume, lead to switching at fields lower than the intrinsic coercivity. This random character can be observed in the bottom row of Figure 5.4 (b), where the z-component of the atomic spin moments does not exhibit the symmetry expected for a coherent reversal, as it is found at low temperature instead, shown in the top row of the figure. Sato *et al.* [71] and Piotrowski *et al.* [77] find a similar size dependence of the coercive field, although Piotrowski *et al.* investigate systems with lower effective anisotropy and therefore larger diameters are considered. The nanodots with thickness 1.3 nm show a similar qualitative behaviour of the coercivity as function of size to the 1 nm thick systems, although the coercivity is significantly reduced. An increase in the thickness (t) yields a decrease of the magnetocrystalline anisotropy energy due to the $1/t$ dependence. It also affects the magnetostatic energy at the same time and the combination of these effects reduces the switching field, hence the coercivity.
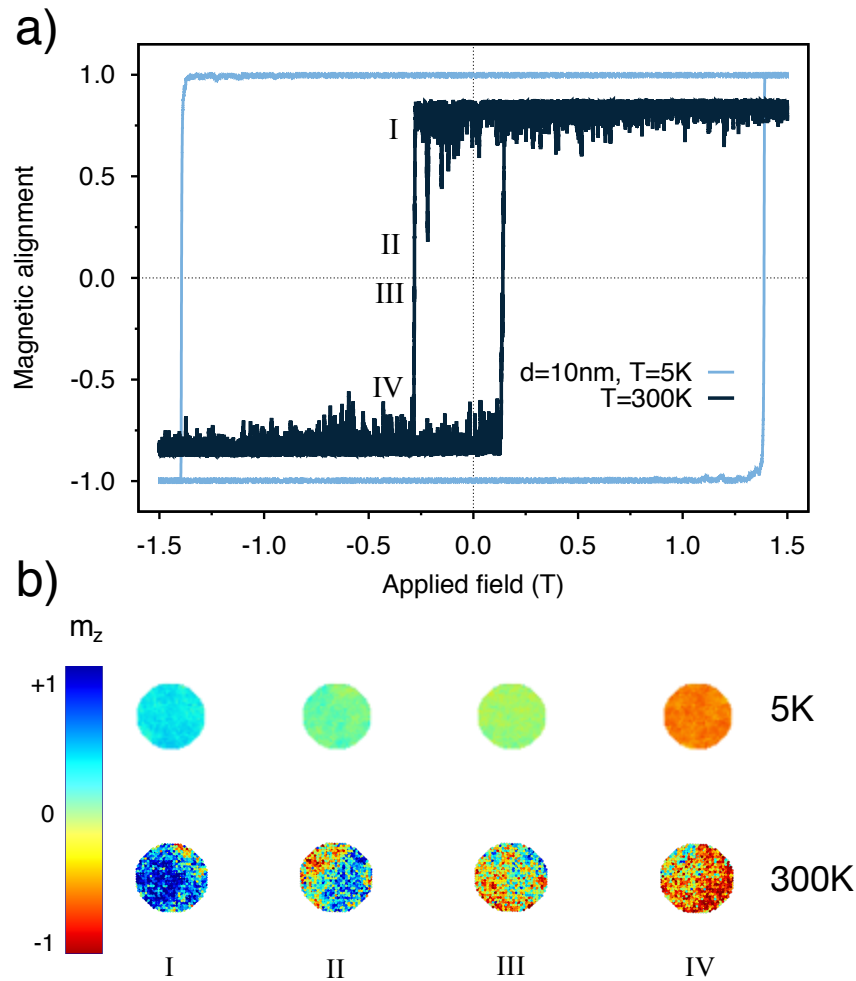
Figure 5.4 (a) Typical simulated easy-axis hysteresis loop for 1.0 nm thick, 10 nm diameter nanodot at temperatures of 5 K and 300 K. The data show a large reduction of the coercivity for elevated temperatures due to increased thermal fluctuations, indicating a change in the magnetic reversal mechanism. (b) Snapshots of magnetisation reversal at 5 K (top) and 300 K (bottom) for a disk of diameter 10 nm and thickness 1.0 nm. I and IV refer to the top and bottom shoulder of M/M_s vs H curve, whereas II and III are configurations just before and after the switching, respectively. At $T = 5$ K the snapshots reveal a coherent reversal of the magnetisation. The reversal is dominated by the strong thermal fluctuations at $T = 300$ K and the snapshots show traces of non uniform switching of the magnetisation. The colour scheme represents the magnetisation along the easy axis direction (z).

The statistical distribution of the coercivity for different nanodot sizes and temperatures is also strongly size dependent. The extracted switching field distributions (SFD) at room temperature for diameters of 10 nm and 50 nm and thickness of 1.0 nm are presented in Figure 5.5. The reduced stability of small elements at elevated temperatures results in much larger distributions of the switching field than obtained for large dots. The simula-
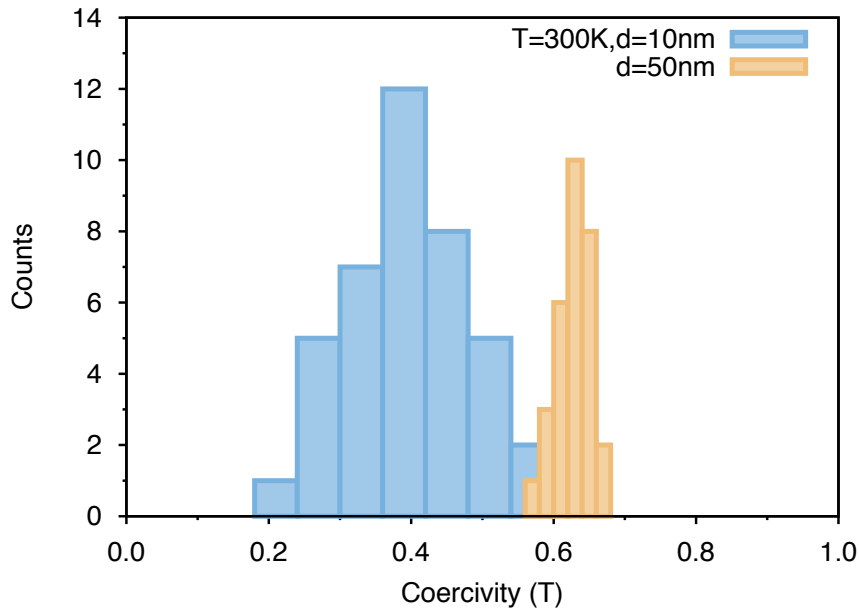
Figure 5.5 Calculated switching field distributions at 300 K for 10 and 50 nm nanodots. The data show that reduced nanodot diameters lead to a larger thermal switching field distribution affecting the stability of the magnetization.

tions are performed using a different pseudorandom number sequence representing the random nature of the thermal noise in the simulations, whereas each nanodot of a given size is identical in terms of the number of atoms and magnetic parameters. Therefore, the origin of this distribution must be the random thermal fluctuations during the reversal process and hence the distribution is the *thermal* switching field distribution (TSFD) [78]. At the switching field the time scale of the reversal is determined by these random thermal fluctuations, leading to a natural TSFD for a switching process on the time-scale of a few nanoseconds. The calculated SFD resembles a skewed normal distribution in agreement with the work of Kurkijärvi [79]. However, a more quantitative analysis of this asymmetry in the distribution is limited by the reduced statistical sample considered in our work due to the long time required to perform the simulations. We note that the TSFD is also thickness dependent, being narrower for thicker films due to the reduced thermal fluctuations associated with the larger volume. It is worth observing that the TSFD intrinsically limits the ability to reliably reverse a nanodot at a given field and time-scale, resulting in a natural distribution of switching probability for a finite time and strength of an applied field pulse [77].

5.5 MTJ field-induced switching

We have investigated the field induced magnetisation dynamics of CoFeB MTJs with structure (1.0nm)[PL]/ MgO(0.85nm)/ CoFeB(1.3nm)[FL], where the number in parenthesis indicates the thickness of the layers. Figure 4.1(c,d) shows a schematic view of the simulated MTJ stacks. Due to the strong magnetostatic coupling between the ferromag-
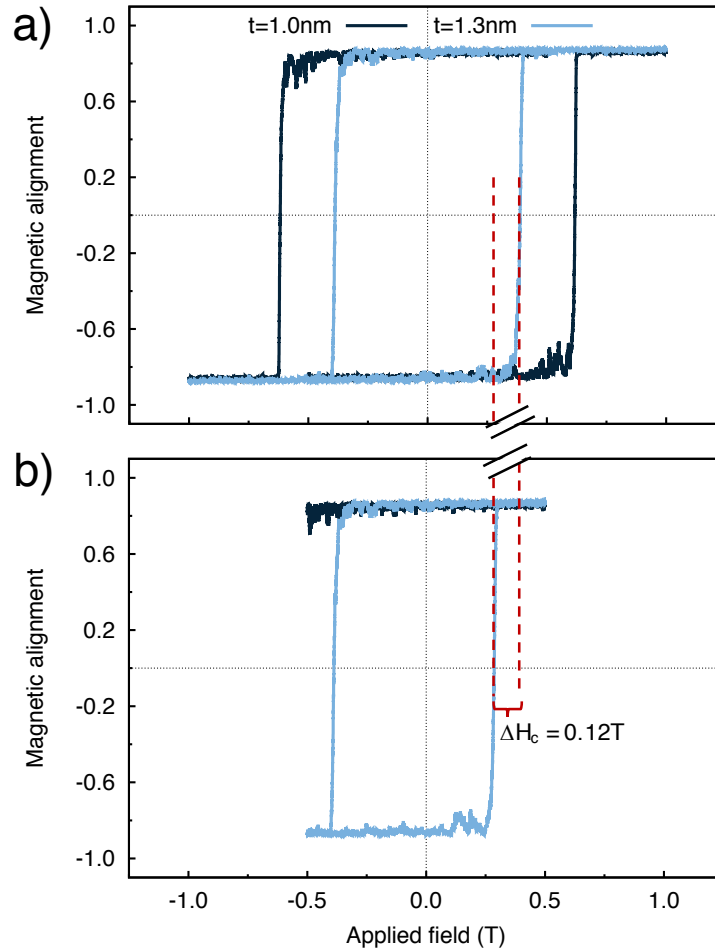
Figure 5.6 Major (a) and minor (b) hysteresis loops for a MTJ of diameter 30 nm at 300 K, the dotted lines mark the coercivity of FL. The major loop shows a large enhancement of both layer coercivities due to the coupling to the stray field. The minor loop exhibits a shift of the hysteresis loop due to the asymmetric effect of the pinned layer stray field for descending and ascending branches ΔH_c of 0.12 T, which is larger than the distribution of coercivity of FL.

netic layers in a MTJ, we have modified the usual macrocell approach for the calculation of the magnetostatic field following the approach proposed by Bowden [44]. This method allows to obtain exact agreement with the atomic scale dipole-dipole interaction assuming a uniform magnetisation in each cell as discussed in more detail in Chapter 3. Despite the

change in the method, we adopt the same $1\,\text{nm}^3$ macro-cell size as used in the simulations of the individual CoFeB/MgO layers.

5.5.1   Switching dynamics

We have calculated major and minor (only the free layer is switched) hysteresis loops for the MTJ at room temperature, as shown in Figure 5.6(a) and Figure 5.6(b), respectively. We compare the coercivity values obtained simulating the isolated CoFeB/MgO layers
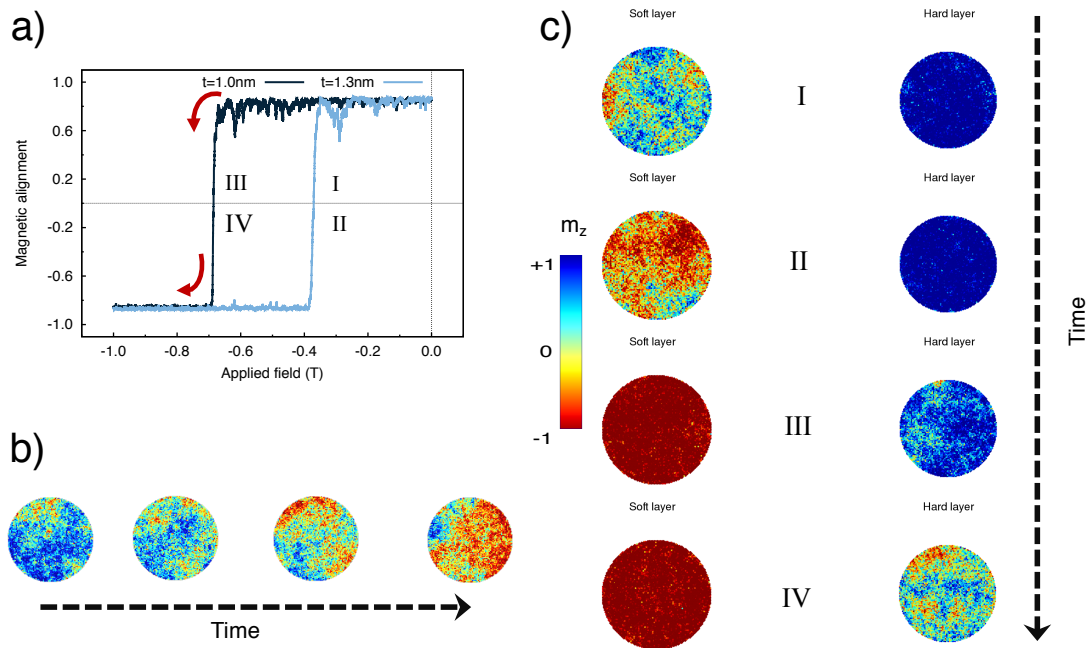
Figure 5.7 (a) Part of major loop from which the snapshots are taken. Roman numbers sign the field points at which the snapshots are taken. (b) Snapshots of magnetisation reversal at 300 K for a nanodot of diameter 20 nm and thickness 1.0 nm. (c) Snapshots of magnetisation reversal at 300 K for a MTJ of diameter 20 nm during a major loop. Left and right dots represent the free and pinned layer, respectively and Roman numbers refer to the field points in (a). The reversal is incoherent, although there is no clear edge nucleation as the diameter is comparable with the single domain size, and free and pinned layer switch independently. The colour scheme represents the magnetisation along the easy axis direction (orthogonal to the dot).

with the values obtained performing a major loop for the whole MTJ stack. We find that the magnetostatic coupling in the multilayer tends to stabilise the magnetic structure and enhances the coercivity of both the free and pinned layers. The coercive fields of pinned and free layer exhibit an increase of about 0.1 T and 0.2 T, respectively. In the minor loop, shown in Figure 5.6(b), a bias due to the stabilising (destabilising) effect of the magnetostatic field from the pinned layer for the descending (ascending) branches is

observed for the free layer. Free and pinned layers switch independently via thermally
nucleated switching dynamics, as observed for the individual layers. Figure 5.7(a) shows
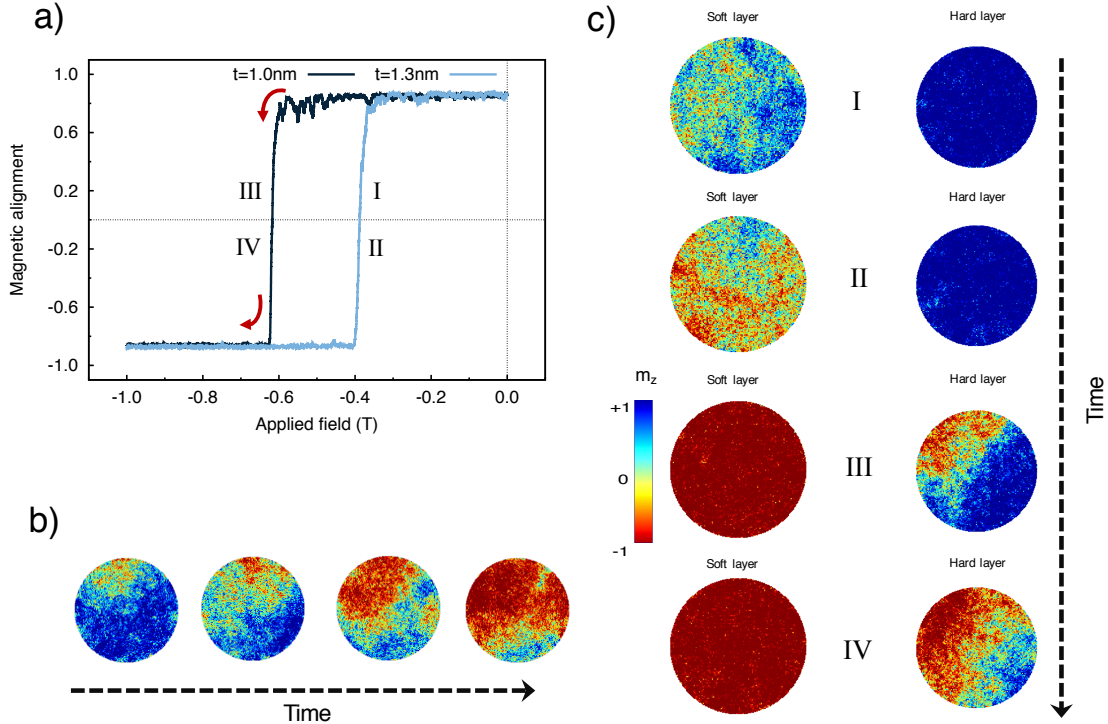
Figure 5.8 (a) Part of major loop from which the snapshots are taken. Roman numbers
represent the field points at which the snapshots are taken. (b) Snapshots of magnetisation
reversal at 300 K for a nanodot of diameter 30 nm and thickness 1.0 nm. (c) Snapshots
of magnetisation reversal at 300 K for a MTJ of diameter 30 nm during a major loop.
Left and right dots represent the free and pinned layer, respectively and Roman numbers
refer to the field points in (a). The snapshots show that free and pinned layer switch
independently and edge nucleation occurs. Interestingly, as the soft layer is characterised
by a larger single domain size, the nucleation is more evident in the pinned (hard) layer
than in the free (soft) layer. The colour scheme represents the magnetisation along the
easy axis direction (z).

a branch of the major hysteresis loop of a 20 nm MTJ, where both the free (soft) and
pinned (hard) layers switch their magnetisation. The reversal modes of both layers are
characterised by thermal activation and reverse independently. In Figure 5.8(a) similar
results obtained for a MTJ of diameter 30 nm are presented. Differently from the previous
case, we clearly observe edge nucleation, in agreement with the analysis proposed for
the single layers at room temperature. Interestingly, the nucleation is more evident in
the pinned (hard) layer than in the free (soft) layer since the free layer is characterised
by a larger single domain size and the same reason can be applied to for the 20 nm MTJ.
Furthermore, one can see from Figure 5.7(a) and Figure 5.8(a) that the magnetisation

exhibits less fluctuations for larger MTJ diameters due to a volume effect, in particular close to the nucleation field.
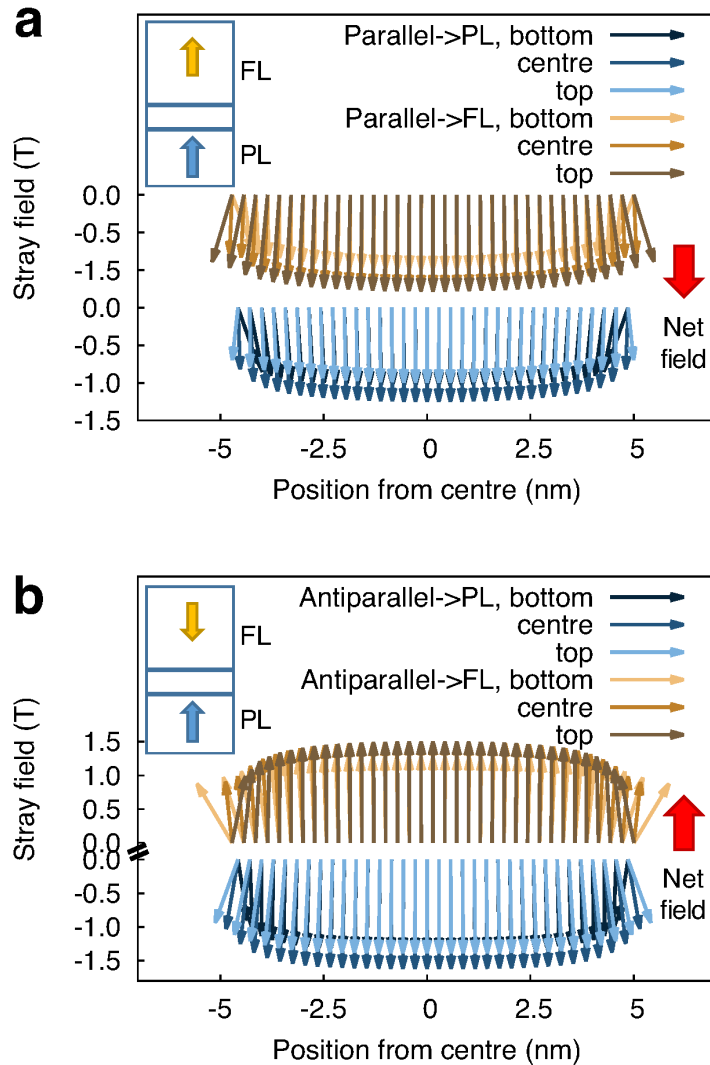
Figure 5.9 Stray field generated by three atomic layers in PL (black and blue arrows) and FL (yellow and brown arrows) of a 10 nm MTJ in parallel (a) and anti-parallel (b) configuration as function of position from the centre of the disk. The magnetisation of the MTJ is uniform and no relaxation of the spin configuration from the configuration where all the spins are aligned is performed. The insets show a schematic of the layer magnetisation and the net average stray field. Bottom, centre, and top refer to the base, central region and top region of each magnetic layer (PL and FL), respectively.

A calculation of the magnetostatic field in the pinned and free layer for uniform parallel and anti-parallel relative orientation of the magnetisation is presented in Figure 5.9 (a) and Figure 5.9 (b), respectively. As one expects, when both the free and pinned layer are magnetised along the same direction the stray field acts as a stabilising field, whereas

the net dipolar field tends to align the magnetisation of both layers along the same direction when the MTJ is in an anti-parallel state. Interestingly, the largest edge non-uniformities of the total stray field occur in the parallel configuration, since the components of the field almost cancel out in the anti-parallel configuration at the edges. As a consequence, edge nucleation processes are more likely when free and pinned layer are parallel. On the other hand, in anti-parallel configuration the magnetostatic field tends to destabilise the system. In the case of MTJ devices we find that the strong coupling of the magnetic layers can lead to a complex change in the magnetic properties such as the coercivity, with the magnetostatic interaction that aids or hamper the magnetisation reversal depending on the relative orientation of the ferromagnetic layers.

It is worth noting that there is a large difference between the coercivities obtained for the soft layer in our simulation of a perfect nanodot or MTJ and those measured experimentally, where coercivities are typically less than 0.1 T [50, 72, 77]. This large discrepancy can be explained considering that in our model we have used material parameters derived from experimental measurements of continuous thin films and the system does not present any structural defects or degradation of the magnetic properties. Generally, realistic devices are affected by edge damage and defects which can lead to a reduction of the coercivity with respect to the ideal case. We performed hysteresis loop simulations for MTJ shaped as trapezoid rather than as perfect cylinders mimicking the fabrication processes, to investigate the effect of the magnetostatic interaction when free and pinned layer have different shapes. The results show a weak reduction of the coercivity, suggesting that shape defects caused by the fabrication process are not the main factors responsible for the difference between experiments and simulations, as sometimes assumed experimentally. We also stress that the sweep rate of the external field used in our simulation is order of magnitude faster than in experiments, and this could explain in part the larger coercive field values.

5.6 Conclusions

In this chapter we presented the systematic investigation of the reversal mechanism of the magnetisation in CoFeB/MgO nanodots using an atomistic spin model where thermal effects and magnetostatic coupling are taken into account. An initial study on the full MTJ stack whose components are the single nanodots is also discussed. The magnetisation reversal in CoFeB/MgO nanodots and MTJs can be described as thermally nucleated and incoherent at temperatures relevant to device operation. This results in a large reduction of the coercivity of the system compared to a coherent reversal mechanism. Such a reduction represents an issue on a device level that needs to be addressed in order to achieve a further

scaling of the device dimension. Moreover, the existence of an intrinsic thermal switching field distribution on the sub-nanosecond time-scale is a signature of these systems and limits how accurately the magnetisation reversal can be controlled. In addition to the properties exhibited by the individual ferromagnetic layers, the magnetostatic interaction between these layers in the MTJ geometry leads to a stabilising/destabilising effect on the magnetisation of the layers depending on the relative orientation of their magnetisation and causes a shift of the minor hysteresis loop. Our results highlight the importance of considering finite size effects, interfacial effects and thermal fluctuations when modelling such small scale magnetic devices, as these can have a dominant effect on their reversal mechanisms and physical properties.

Chapter 6

Energy barrier to magnetisation reversal in CoFeB/MgO nanodots

The study of the temperature and size dependence of the energy barrier of CoFeB/MgO nanodots will be the focus of the chapter. One of the most relevant parameters in storage device and recording media technology is the thermal stability. It determines the retention time of the stored information, which is required to last longer than ten years. The Arrhenius-Néel law [24] gives the probability that a single domain particle subjected to thermal fluctuation switches:

$$f = f_0 \exp\left(-\frac{K_u V}{k_B T}\right).$$ (6.1)

where f_0 is the attempt frequency, usually assumed around 1×10^9 Hz-1×10^{11} Hz for magnetic systems, K_u and V are the anisotropy energy and the volume of the system, $k_B = 1.381 \times 10^{-23}$ JK^{-1} is Boltzmann constant and T the absolute temperature. The product $K_u V$ is the energy barrier to the magnetisation reversal and the ratio with the thermal energy $k_B T$ determines the thermal stability of the system. In a bistable magnetic device such as a MTJ, the energy barrier is mainly determined by the magnetic anisotropy of the device, which in CoFeB-based MTJs arises due to hybridisation of the atomic orbitals of the magnetic layer with the oxygen at the MgO interface [1, 54, 55]. In CoFeB/MgO this interfacial anisotropy is sufficient to provide thermal stability and to support an out-of-plane magnetisation of the system up to thicknesses of the ferromagnetic layer of 1.3 nm.

6.1   Introduction

The dependence of the energy barrier on size and temperature and the transition mechanism across the barrier between stable configurations are key issues in determining the stability in bi-stable systems such as MRAMs. For non-uniform reversal, that can occur when the system size is larger than the critical domain size, the energy barrier is reduced with respect to a collinear mechanism. This comports that larger elements are required to guarantee a lifetime of the stored data of about ten years.

Experimental studies have investigated the energy barrier of MTJ systems, the core of a MRAM, as function of size [63, 71, 72, 80–82]. Gajek *et al.* [82] determine the energy barrier via measurements of the switching current as function of the switching frequency and find that the energy barrier scales quadratically with the diameter of the device, therefore suggesting that the spins behave as a macrospin. A sharp change in the size dependence of the energy barrier that resembles a linear trend for diameters larger than 30 nm can be observed in Figure 3 of the same work. Moreover, the average coercivity of the whole MTJ junction flattens for larger dimensions. Sato *et al.* [71, 72, 80], Sun *et al.* [81], Takeuchi *et al.* [63] found lower values than expected from a macrospin model for system larger than the estimated single domain size. This suggests domain nucleation and a crossover towards a uniform reversal for smaller dimensions. In a recent work, Enobio *et al.* [83] extract the energy barrier for MTJs similar to those investigated by [63] performing retention time measurements and suggest that a more complex magnetisation dynamics might occur. Despite the numerous experimental studies, a definitive understanding of the reversal mechanism is yet to be found, also taking into account the dependence of the results on the employed measurement technique. Furthermore, the effect of temperature has been experimentally investigated only by Takeuchi *et al.* [63].

Performing micromagnetic simulations, Munira and Visscher [84] find that non-collinear modes can occur in MRAM elements and Chaves-O'Flynn *et al.* [85, 86] show that a transition from uniform to nucleation magnetisation reversal energy barrier occurs as the size is increased. The theoretical analysis performed so far is based on micromagnetic modelling. The continuum approach, on which the standard micromagnetism is developed, fails with the miniaturisation of devices down to few nanometres in thickness and the inclusion of thermal effects. Therefore, atomistic spin models become necessary to accurately describe the properties in nanomagnets.

First, we introduce the constrained Monte Carlo method, i.e. the computational approach used to extract the energy barrier. We present the angular and temperature dependence of the energy barrier for CoFeB/MgO nanodots with different diameter. We derive the effective anisotropy and the energy barrier and find that at finite temperature

the energy barrier is characterised by a size dependence that scales quadratically for small diameters and becomes linear for larger dimensions. The former trend can be attributed to a coherent reversal, whereas the latter can be explained by a domain wall mediated switching process. The transition between the two regimes it is not well defined and there are not available analytic approaches that describe it, despite the fact that it falls in a diameter range of technological interest. Finally, we compare our results with experimental measurements performed on similar systems and we find an excellent agreement with our simulations.

6.2 Constrained Monte Carlo algorithm

A standard Monte Carlo (MC) algorithm allows to determine the magnetic properties at thermal equilibrium. In such a condition one can calculate the magnetisation of the system, but not the magnetic anisotropy since the magnetisation aligns along the easy axis direction at equilibrium. To circumvent this, one can keep the system in a quasi-equilibrium state. Such an approach has been exploited in the constrained Monte Carlo (cMC) algorithm. cMC is a Monte Carlo method developed by Dr. P. Asselin, Dr. R. F. L. Evans and Prof. Roy W. Chantrell [87] which acts on two spins at the same time rather than on a single spin as in standard MC algorithms, and constrains two spatial components of the system magnetisation to be zero, while allowing the other component to vary in magnitude. In this algorithm two spins, which are not necessarily neighbours, are randomly selected per cMC move. Initially, the first spin is displaced as in a MC method and the move is accepted without evaluating the change in energy. The second spin is then displaced with the requirement that the sum of the new components of the two spins perpendicular to the constraint direction, let us assume along the z–axis, yields $M_x = M_y = 0$ for the total magnetisation. This grants that the total magnetisation remains constrained. Once the second spin is displaced, the change in energy due to both the two spins displacement is evaluated and the global move is accepted following a MC approach, where the probability is corrected to account for the fact that two spins are considered. If the move is rejected, both spins are discarded and a whole new set of spins is selected. A detailed description of the algorithm can be found in [87]. This approach enables the direction of the global magnetisation to be constrained during the simulation along specific directions, whilst allows individual spins $\vec{S}_i$ to reach thermal equilibrium. Since the system is not in equilibrium, the total internal torque acting on the

magnetisation $\vec{M}$ [87]

$$\vec{\tau} = \left\langle \sum_i \vec{S}_i \times \vec{H}_{\text{eff}}^i \right\rangle = \vec{M} \times \frac{\partial \mathcal{F}\left(\vec{M}\right)}{\partial \vec{M}} \qquad (6.2)$$

does not vanish. Here $\langle \rangle$ denotes the thermodynamic average, $\vec{H}_{\text{eff}}^i$ is the effective field acting on each $\vec{S}_i$ and $\mathcal{F}(\vec{M})$ is the Helmholtz free energy of the system. $\mathcal{F}$ measures the amount of work that can be obtained in a physical system at constant temperature and volume. The work done on the system at constant temperature is equivalent to the magnitude of the torque $|\vec{\tau}|$ acting on the system and is given by:

$$|\vec{\tau}| = -\frac{\partial \mathcal{F}}{\partial \vartheta}, \qquad (6.3)$$

where ϑ is the constraining direction. The anisotropy energy is obtained as the variation of the free energy by:

$$\Delta \mathcal{F} = -\int d\vartheta \, |\vec{\tau}|. \qquad (6.4)$$

Calculating $\Delta \mathcal{F}$ at different temperatures allows to obtain the temperature dependence of the anisotropy. The global magnetisation at a specific constrained angle and temperature is also computed at the same time. If the dependence of the anisotropy energy and magnetisation on the temperature are calculated, it is possible to investigate the scaling with the temperature of these quantities, as they can provide very useful insights. The obtained results can be compared with Callen-Callen theory [27], which provides the temperature scaling for uniaxial and cubic systems.

6.3   Total torque calculation

We use the cMC algorithm to calculate the angular dependence of the restoring torque acting on the magnetisation via the constraint of the total magnetisation away from the easy-axis direction. Such simulations are performed at different temperatures and for different dot diameters. Figure 6.1 shows the angular dependence of the torque for discs of diameter 10 nm (a) and 30 nm (b) at 25 K and 300 K. As expected, there is a decrease of the torque from 25 K to 300 K due to thermal fluctuations in both (a) and (b). Whilst the torque of the 10 nm disc shows a $\sin(2\vartheta)$ character, the torque is significantly reduced for the larger disc for angles smaller than 135°, where ϑ is the angle formed by magnetisation and easy axis. In this case the torque does not follow the simple $\sin(2\vartheta)$ relation and this effect becomes more pronounced at higher temperature. For small diameters the system is in a single domain state and the transition over the energy barrier occurs via coherent
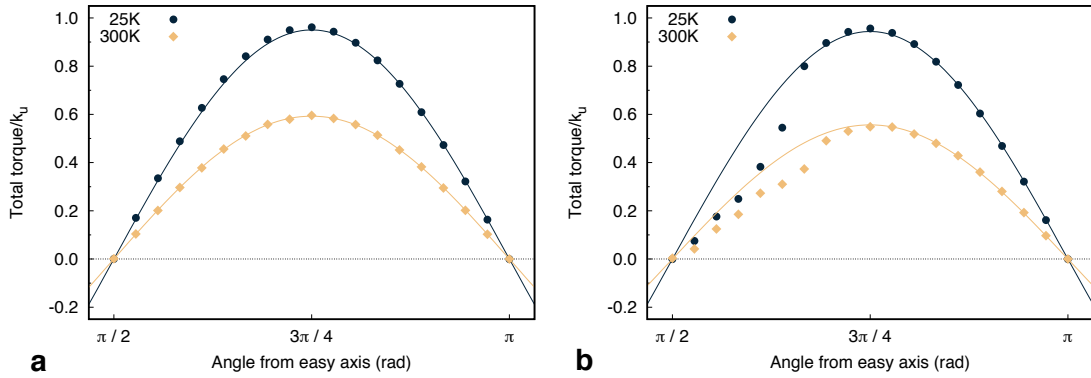
Figure 6.1 Angular dependence of the scaled total torque for (a) 10 nm and (b) 30 nm CoFeB/MgO dots at 25 K and 300 K. The torque curves are scaled by the uniaxial energy constant at 0 K k_u. In the plots dots represent the data and lines the fit of the data in the range $[4/5\pi : \pi]$ with a $\sin(2\vartheta)$ function.

rotation of the magnetisation. The critical domain size, i.e. the largest system size above which the formation of a domain is energetically favourable, can be estimated by the Bloch-wall width $\delta_B = \pi\sqrt{A_s/K_u}$ [24]. In δ_B expression A_s is the exchange stiffness and K_u is the magnetocrystalline anisotropy energy density of the material. If the system is larger, domains can form [88]. From the expression above, we estimate $\delta_B \sim 15$ nm for our dots. This suggests that for a diameter of 10 nm the dot is in a single domain state, whereas domains can be introduced into the system during the magnetisation reversal process for larger lateral dimensions.

6.4   Energy barrier calculation

The energy barrier separating the two stable states of the magnetisation can be accessed by integrating the total torque over the angular distribution. Figure 6.2 presents the angular dependence of the free energy for a 10 nm (a) and 30 nm (b) disc for different temperatures. Similarly to what we observed for the torque, the 10 nm dot follows the trend characteristic of coherent reversal. For coherent reversal in a uniaxial system the energy is expected to exhibit a $\sin(\vartheta)^2$ behaviour, where ϑ is the angle formed by magnetisation and easy axis. Snapshots of the out-of-plane spin configuration confirm the coherent nature of the reversal, even though thermal effects cause large fluctuations at small system dimensions such as 10 nm and the switching is not completely coherent. The free energy of the 30 nm disc deviates from the expected uniform reversal trend. It flattens for angles close to $\pi/2$ where the maximum of the energy is located, a behaviour consistent with a nucleation-type reversal. The analysis of the spin configurations in the inset of Figure 6.2(b) shows that the crossing over the energy barrier occurs via
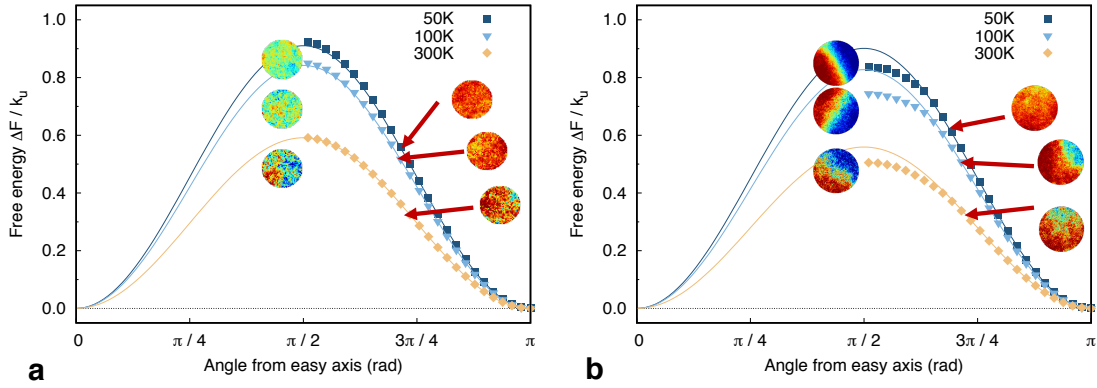
Figure 6.2 Angular dependence of scaled the energy barrier scaled by the uniaxial energy constant at $0\,\mathrm{K}$ for a $10\,\mathrm{nm}$ (a) and $30\,\mathrm{nm}$ (b) dot. The insets describe snapshots of the out-of-plane component of the magnetisation (red = spin-down, green = in-plane, blue = spin-up) at $50\,\mathrm{K}$, $100\,\mathrm{K}$ and $300\,\mathrm{K}$ for constraint angle of the magnetisation of $\pi/2$ and $2/3\pi$. The transition over the energy barrier is uniform for disc of $10\,\mathrm{nm}$ diameter and the energy barrier follows the expected $\sin(2\vartheta)$ behaviour. For larger diameters the reversal is incoherent and the energy barrier is lower with respect to the uniform case. Lines are the fit of the data in the region $[4/5\pi : \pi]$ with a $\sin(\vartheta)^2$ function.

nucleation and not by coherent rotation, in agreement with a lower threshold for the magnetisation reversal. This reduction of the energy barrier in case of nucleation poses issues for technological applications, as it yields a lower thermal stability than predicted using a macrospin model.

One of the most relevant parameters for applications is the stability factor Δ, defined as the energy barrier normalised by the thermal energy $k_{\mathrm{B}}T$, where $k_{\mathrm{B}} = 1.381 \times 10^{-23}\,\mathrm{JK}^{-1}$ is Boltzmann constant and T the absolute temperature. For technological applications, such as storage devices, a stability factor larger than 60 or 70 at room temperature is required in order to guarantee a 10 years data retention. We evaluate Δ of the discs as function of diameter at different temperatures and Figure 6.3 (yellow line and symbols) presents the size dependence at room temperature. Δ is quadratic for dots smaller than $25\,\mathrm{nm}$, whereas it starts deviating towards a linear trend for larger dots. The different behaviours of Δ as function of the dot size can be understood in terms of the reversal mechanism of the magnetisation. If the reversal is coherent, E_{b} follows the macrospin behaviour and the energy is given by the analytic expression $E_{\mathrm{b}} = K_{\mathrm{u}}V$ [24], where K_{u} is the magnetocrystalline energy density and $V = \pi t d^2/4$ is the disc volume. In the case of nucleation, E_{b} can be analytically obtained by the product σw, where $\sigma = 4\sqrt{A_{\mathrm{s}}/K_{\mathrm{u}}}$ is the domain wall surface energy density, A_{s} the exchange stiffness, K_{u} the magnetic anisotropy energy and $w = dt$ is the surface of the disc [24]. The expression for σ is derived assuming that a narrow domain wall in the centre of the system separating two
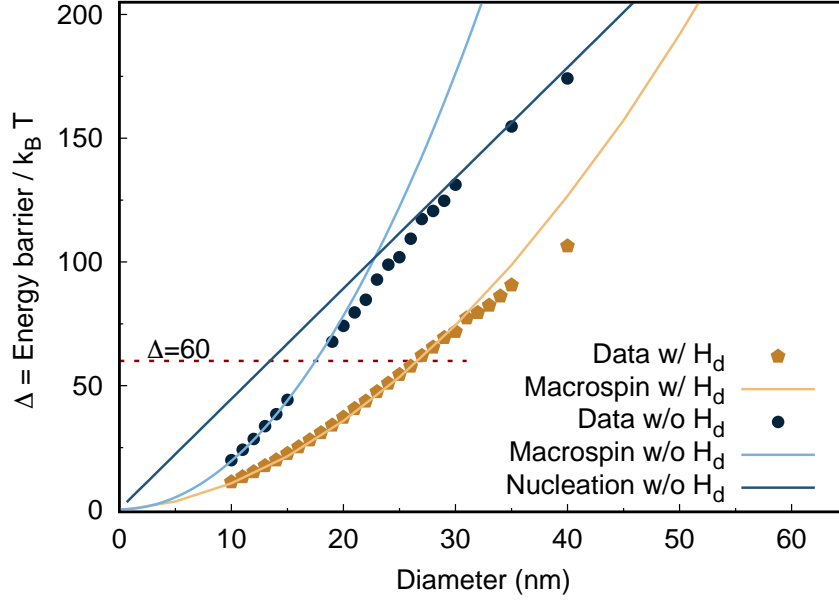
Figure 6.3 Stability factor (Energy barrier/$k_B T$) as function of diameter for CoFeB/MgO dots at 300 K. Black dots and light brown diamonds represent the calculated stability factors obtained performing simulations without and with magnetostatic interactions (H_d), respectively. Light and dark blue lines are the analytic models for the macrospin and nucleation models, respectively. The red dashed line marks $\Delta = 60$, which is the minimum stability requirement for real devices at room temperature.

domains corresponds to the highest energy configuration, and this consideration allows to use the domain wall energy in place of the domain energy. It follows that E_b is quadratic in the diameter for a macrospin-like system and linear in case of nucleation.

So far we have neglected the magnetostatic contribution in the analytic approach, but for finite size systems such as cylinders, the effect of long-range dipole-dipole interactions should be taken into account when evaluating δ_B. If we do so, we obtain an effective anisotropy energy K_{eff} that contains these shape effects. For a uniformly magnetised cylinder the magnetostatic contribution can be written in terms of the demagnetisation tensor and K_{eff} becomes:

$$K_{eff} = K_u - \frac{1}{2}\mu_0 M_s^2 \frac{(N_{zz}-1)}{2}. \tag{6.5}$$

Here M_s is the saturation magnetisation and N_{zz} is the zz component of the demagnetisation tensor. The second term on the RHS of Equation(6.5) is the demagnetising energy for a cylinder which is magnetised along the easy axis direction z and $(N_{zz}-1)$ comes from symmetry considerations for a cylindrical system and from the fact that the demagnetisation tensor has unitarian trace $(N_{xx}+N_{yy}+N_{zz})$ in SI units. This contribution yields a smaller out-of-plane anisotropy energy for thin cylinders, causing a broadening

of δ_B and a reduction in the energy barrier compared with the case where this term is neglected. For a non-uniform magnetisation configuration, the contribution arising from the magnetostatic coupling cannot be obtained following the same approach because the demagnetisation tensor is a macroscopic quantity defined for a system that has uniform magnetisation and depends on the shape only. In fact, even in the most simple case of system divided in two domains of opposite magnetisation with an infinitesimally thin wall separating the two regions, an analytic formulation is not easily accessible. For this reason, we also compute the torque acting on the magnetisation as well as the energy barrier neglecting the magnetostatic contribution. If we do not consider this term, the macroscopic anisotropy energy is given by the magnetocrystalline anisotropy K_u only and the results can be tested against the available models.

6.4.1 Energy barrier dependence on size in zero field

We compare our data obtained with and without the inclusion of magnetostatic interactions with the analytic expression for a macrospin model, where where the macroscopic parameters A_s ($\sim 20 \times 10^{-12}\,\mathrm{Jm}^{-1}$) and K_u ($\sim 1 \times 10^6\,\mathrm{Jm}^{-3}$) are derived from the parameters we used in the atomistic simulations. The results for the size dependence of the stability factor are plotted in Figure 6.3 (black dots and blue lines). An excellent agreement between simulated data and analytic expression for the macrospin model is found up to diameters $\sim 30\,\mathrm{nm}$ and $20\,\mathrm{nm}$ for calculations with and without magnetostatic interactions, respectively. The data deviate from the above mentioned trend and seem to lie in an intermediate regime as larger diameters are considered, regime for which there are not available analytic expressions to compare with. As the diameter is increased further, E_b follows a linear trend which is well fit by the nucleation theory if there are not magnetotstatic interactions. For simulations performed accounting for the magnetostatic contribution, a similar trend is observed. This suggests a domain wall mediated nature of the reversal mechanism, although a direct comparison with theoretical expressions is not possible.

A similar analysis has been performed by Chaves-O'Flynn *et al.* [86]. Chaves-O'Flynn and collaborators use a zero temperature micromagnetic approach and rescale the MTJ parameters and size to that of a permalloy disc. Chaves-O'Flynn *et al.* [86] achieve a good agreement with the analytic expressions for both the macrospin-like and nucleation regime. Nonetheless, we point out that the use of K_{eff} calculated using the demagnetisation coefficients in case of nucleation it is not appropriate as it leads to an overestimation of the domain wall energy. We attribute the good agreement between the data and the theory in this regime to a combination of effects between the scaling of the magnetic properties of the system and micromagnetic simulations.

The red dashed line in Figure 6.3 identifies $\Delta = 60$, which is the minimum stability requirement for real devices at room temperature. It marks the smallest size which guarantees the minimum required thermal stability, which is about 28 nm for our simulations performed including the magnetostatic contribution. New devices are aimed to be produced below the 20 nm technological node. Consequently, the CoFeB/MgO systems investigated in this thesis would not satisfy the requirement for thermal stability at such a node. This shows the need for improvement in the magnetic properties in order to match the required stability. A possibility is to increase the complexity of the stack, as in MTJs with the free layer composed of a double MgO [71, 89] barrier. Such a design yields a better crystallisation, reduces the effect of the stray field and is characterised by a larger interfacial anisotropy due to the increased number of CoFeB/MgO interfaces. Recently, Watanabe *et al.* [52] proposed a MTJ structure with an elongated FeB free layer where the shape anisotropy provides the required thermal stability for elements smaller then 10 nm in diameter. Despite the very promising features, the dynamic properties of such a stack need to be fully investigated and understood yet.

6.4.2 Effect of an applied field on the size dependence of the energy barrier

An applied field acting on the reference layer of a MTJ induces variations in the energy landscape of the same layer. For instance, if the field is perpendicular to the stack it raises one minimum and lowers the other. For simple MTJ geometries such as a single free
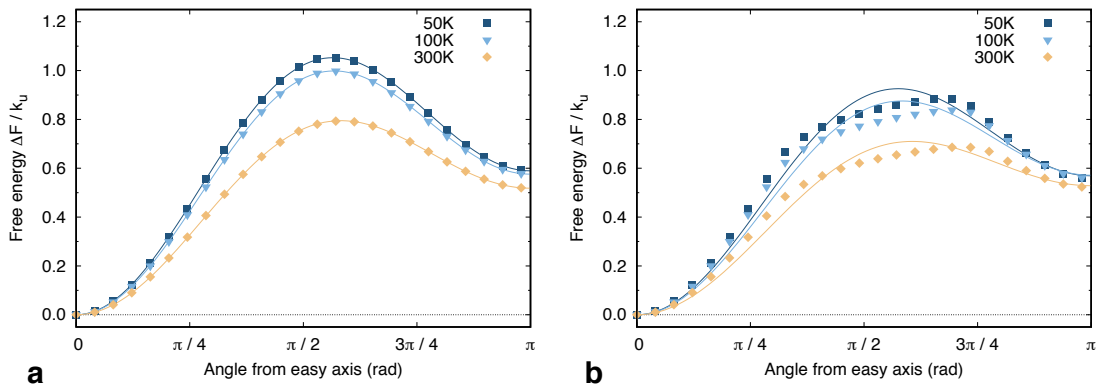
Figure 6.4 Energy barrier normalised by the maximum of torque as function of angle between the magnetisation and the easy axis for CoFeB/MgO dots of diameter 10 and 30 nm at $T = 50$ K, 100 K and 300 K for an out-of-plain applied magnetic field of 0.5 T along positive *z*-direction. Lines are fit of the data in the small angles region $[0 : 1/5\pi]$.

layer MTJ [50, 71, 83], the recording layer is subjected to the stray field coming from the reference layer. This may result in the shift of hysteresis loops, as we observed in [69]. To

understand the effect of such a coupling on the thermal stability, we perform simulations at 300 K applying an external field $H_a = 0.5\,\text{T}$ along the positive z-direction, perpendicular to the dot. Figure 6.4 shows the plot of the free energy as a function of the angle between the total magnetisation and the easy axis for dots of diameter 10 nm and 30 nm at $T = 50\,\text{K}$, 100 K and 300 K. The external field decreases the energy of the minimum corresponding to the field and initial magnetisation pointing in the same direction, whereas it lifts the other minimum. This makes the energy barrier between the two stable configurations inequivalent, a feature that is reflected in the parallel magnetisation configuration to be more stable than the antiparallel state in a MTJ.

To fit the angular dependence of the energy barrier we add to $K_u \sin^2(\vartheta)$ a term proportional to the applied field: $-2H_a \cos(\vartheta_0 - \vartheta)$. Here H_a is the magnitude of the applied field and ϑ_0 is the angle between the easy axis and the applied field. This expression is derived assuming a single domain particle and in our case the expression follows a $\cos(-\vartheta)$ dependence since H_a and the easy axis are parallel. Similarly to what is observed in Figure 6.2, when the reversal is uniform the data and the fit show a good agreement. For diameters larger than the single domain size, the system is characterised by a non-uniform reversal and the fit cannot reproduce the data correctly. A net flattening of the free energy can be observed for a dot diameter of 30 nm due to nucleation processes, as in the case of simulations performed in zero field. We extract the two energy barriers from the angular dependence of the torque and we plot the stability factor Δ as function of particle diameter at 300 K in Figure 6.5. The stability factors for the more (less) stable configuration Δ_+ (Δ_-) are described using light brown diamonds (dark brown triangles) and the rest of the symbols are the same as in Figure 6.3. As expected, Δ_+ is larger than Δ, confirming that the effect is to increase the thermal stability of the system, and it exhibits a quadratic dependence on the diameter. On the other hand, $\Delta_- < \Delta$ since the energy barrier is lowered by the applied field. Δ_- shows a trend that is not well defined for the range of diameters simulated. For discs smaller than 25 nm the size dependence exhibits a quadratic behaviour consistent with the coherent transition over the barrier. For larger diameters, a change in the trend seems to occur. However, we cannot assess the size dependence of Δ_- due to the fewer data points for large lateral dimensions.

An available analytic approach that describes the effect of an external field on the energy barrier, if magnetostatic interactions are neglected, is provided by the droplet theory [90–92]:

$$E_b^{\text{drop}}(R) = \sigma t \vartheta_d r - 2\mu_0 M_s H_a t \frac{R^2(\vartheta - \sin(\vartheta)) + r^2(\vartheta_d - \sin(\vartheta_d))}{2}, \qquad (6.6)$$

where R, r, ϑ, ϑ_d refer to Figure 6.6, σ is the domain wall energy assuming a domain wall at the centre of the system, M_s the saturation magnetisation of the system and
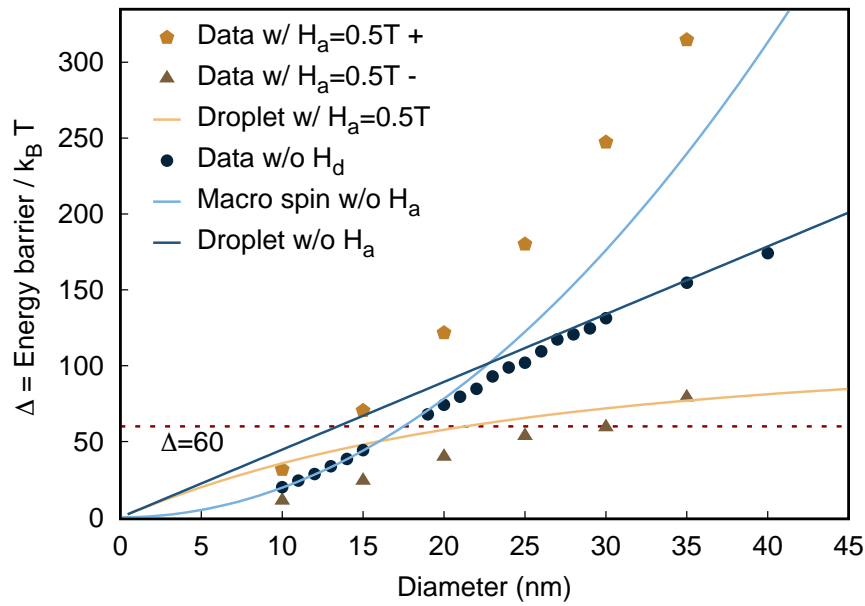
Figure 6.5 Stability factor (Energy barrier/k_BT) as function of diameter for CoFeB/MgO dots without considering magnetostatic interactions at 300 K for an out-of-plain applied magnetic field $H_a = 0.5\,\text{T}$ along the positive z-direction. Black dots represent the calculated stability factors in zero applied field, while the stability factors for the more (less) stable configuration Δ_+ (Δ_-) with the applied field are described using light brown diamonds (dark brown triangles). Dark blue and yellow lines are the analytic models of the droplet theory in zero field and when the field is present, respectively. The light blue line is the macrospin model and the red dashed line marks $\Delta = 60$, which is the minimum stability requirement for real devices at room temperature.

H_a is the magnitude of the external applied field. It is easy to show that Equation 6.6
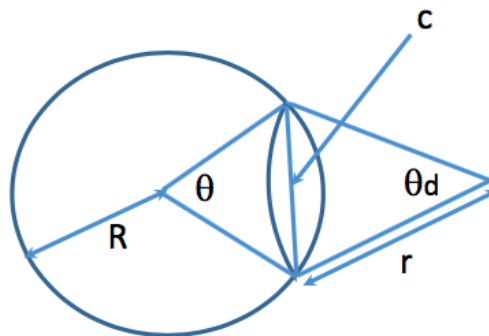
Figure 6.6 Sketch showing the parameters used in the calculation of the energy barrier in the droplet model.

reduces to the nucleation model described above, if there is not an external applied field. The result from the droplet theory for the same H_a is represented by the yellow line in

Figure 6.5. The model predicts an asymptotic behaviour of Δ as function of increasing diameters for a sufficiently strong magnitude of the external field. In a similar study, Chaves-O'Flynn *et al.* [86] investigate the effect of an external field on the stability of the disc, such as the stray field acting on the free layer of a MTJ coming from the reference layer. The approach used to describe the effect of the applied field in the work of Chaves-O'Flynn and co-workers [86] yields a similar expression to the droplet model, predicting a saturation of the energy barrier as larger diameters are considered and large external field are applied. The results obtained by Chaves-O'Flynn *et al.* [86] are in good agreement with the droplet theory when the system does not behave as a macrospin, showing saturation of the energy barrier with the diameter of the disc for large enough applied fields. A comparison between our simulations and the micromagnetic results by Chaves-O'Flynn *et al.* [86] is possible only in the uniform reversal regime, where both show a quadric-like size dependence. For larger diameters we cannot achieve a clear understanding of our results due to the limited range of diameters simulated. Further studies are necessary, in particular for larger dimensions and including shape effects. Nonetheless, we can expect that in absence of magnetostatic interactions our simulations agree at least partially with the droplet theory, based on the results in zero field. We stress that in our simulations the magnetostatic field was not included to allow a direct comparison with the theoretical model, as an analytic description of this term for non-uniform magnetisation configurations is not available yet. Also, as mentioned in the analysis of the zero field case, Chaves-O'Flynn *et al.* [86] include the magnetostatic interactions via the demagnetisation factors. While this approach is suitable for a coherent-like reversal, it is a not appropriate when the magnetisation is in a non-uniform state. It should be also noted that we have considered the simple case of a uniform external field. More complex configurations could lead to larger changes in the energy landscape and require further investigation.

6.5 Temperature dependence of the effective anisotropy

We extract the effective anisotropy energy density K_{eff} from the calculation of the energy barrier. We obtain the temperature dependence of K_{eff} for both the simulations performed with and without including the magnetostatic contribution. Figures 6.7(a,b) show the temperature dependence of K_{eff} in both cases. At low temperature the system requires long time to reach equilibrium and this time increases for larger diameters. Because of this, not all the calculations are converged with respect to the total energy and torque. The empty symbols in Figures 6.7(a,b) represent points that are not fully converged and it is clear that the convergence issue is a function of the disc size. Two main features
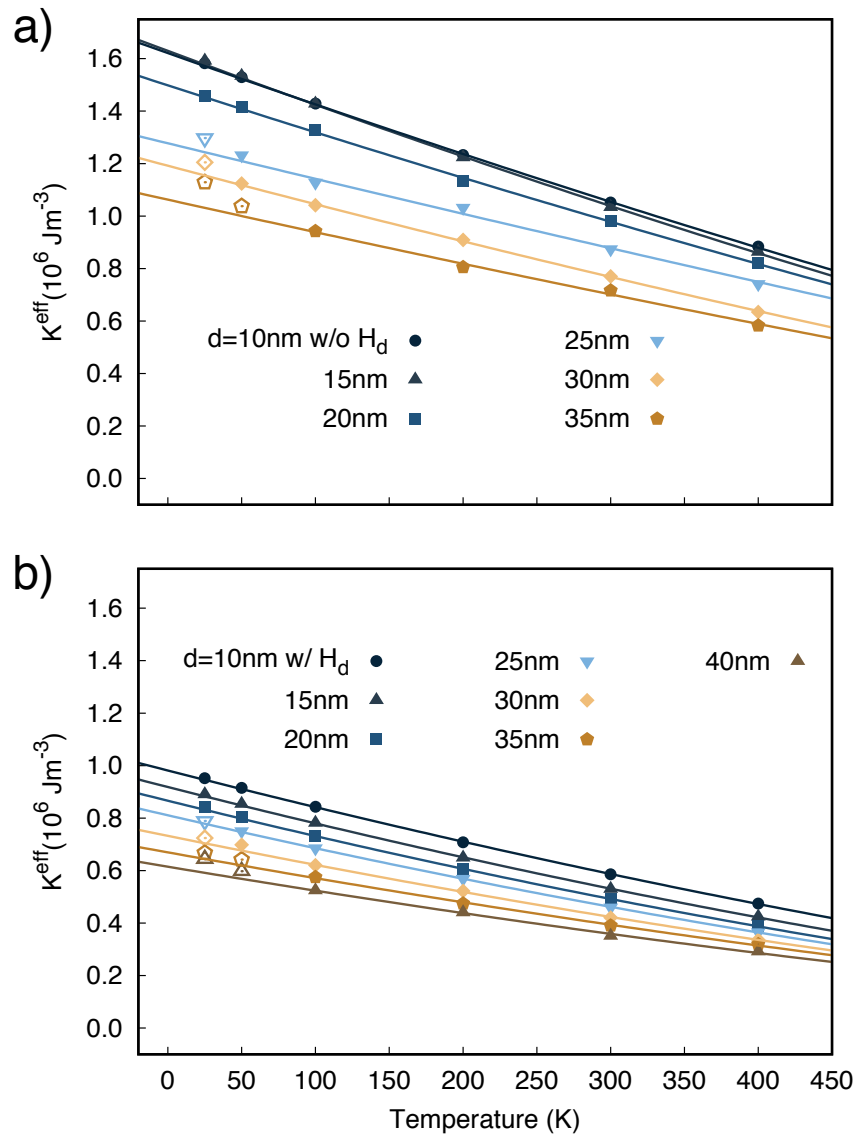
Figure 6.7 Calculated temperature dependence of the effective anisotropy energy density K_{eff} for different disc diameters without (a) and with (b) inclusion of the magnetostatic contribution (H_{d}). Empty symbols represent non-converged points at low temperature of the respective filled points due to the time requirements that increase with the size, and as such are excluded from the fit. Lines are fit of the data following eq. 6.7 in the range 100 K to 400 K.

can be observed by comparing the two plots: first, as expected the in-plane contribution arising from the shape anisotropy yields a reduction of K_{eff} with respect to the case where this is not taken into account. A consequence is the narrower domain wall width in the simulations without magnetostatic interactions since this is proportional to $1/\sqrt{K_{\text{eff}}}$. Second, the temperature dependence as function of diameter differs in the two cases, with a larger reduction of K_{eff} in absence of magnetostatic interactions. To compare the
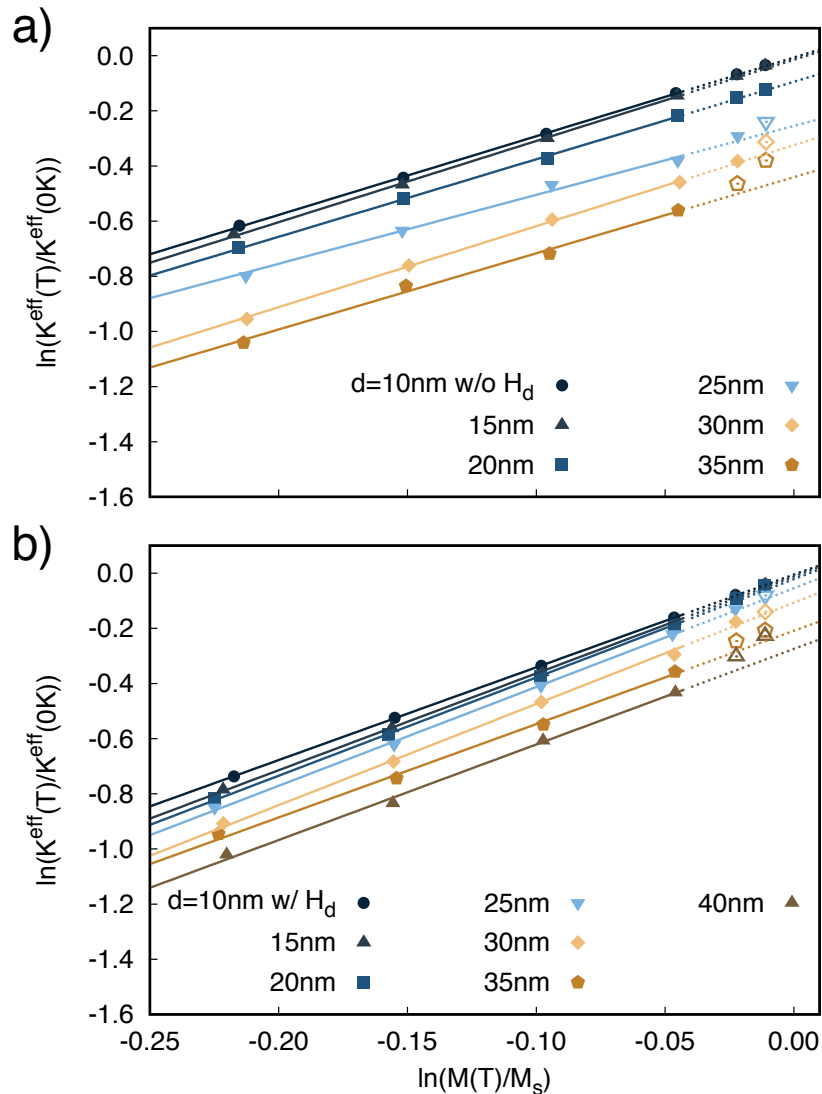
Figure 6.8 Scaling of the effective anisotropy K_{eff} with the system magnetisation $M(T)$ for different disc diameters without (a) and with (b) inclusion of the magnetostatic contribution (H_{d}). Empty symbols represent non-converged points at low temperature of the respective filled points due to the time requirements that increase with the size, and as such are excluded from the fit. Solid lines are fit of the data following eq. 6.7 in the range $100\,\text{K}$ to $400\,\text{K}$, whilst dotted lines represent the fit for $T < 100\,\text{K}$.

trends, we extract the scaling exponent of the effective anisotropy with the magnetisation as function of temperature for different disc diameters from the plot of the former versus the latter. The plots are presented in Figure 6.8(a) and Figure 6.8(b) for simulations with and without the inclusion of the magnetostatic contribution. The fit is performed in the temperature range $100\,\text{K}$ to $400\,\text{K}$ in order to exclude the points that are not fully

converged, and the fit is performed according to:

$$\frac{K_{\text{eff}}(T)}{K_{\text{eff}}(0\,\text{K})} = \left(\frac{M(T)}{M_{\text{s}}}\right)^{n},$$

(6.7)

where n gives the scaling of the anisotropy with the magnetisation. The extracted scaling exponents differ from $n = 3$, expected for a uniaxial system [27, 87], in both the investigated cases. Interestingly, Figure 6.9 shows that for simulations without magnetotstatic contribution the average scaling exponent is lower than for the uniaxial system, around 2.8. On the other hand, the inclusion of the demagnetising field yields an exponent close to 3.4, which might be interpreted as the system has a cubic anisotropy component due to shape effects. A possible explanation for the non-uniaxial character is the variation of the anisotropy over the thickness within the simulated system. The interfacial layer posses a strong uniaxial anisotropy induced by MgO, whilst the rest of the CoFe has no anisotropy. In both cases we observe a sudden change in the trend (Figure 6.7, Figure 6.8) and decrease in the exponent (Figure 6.9). The diameters at which
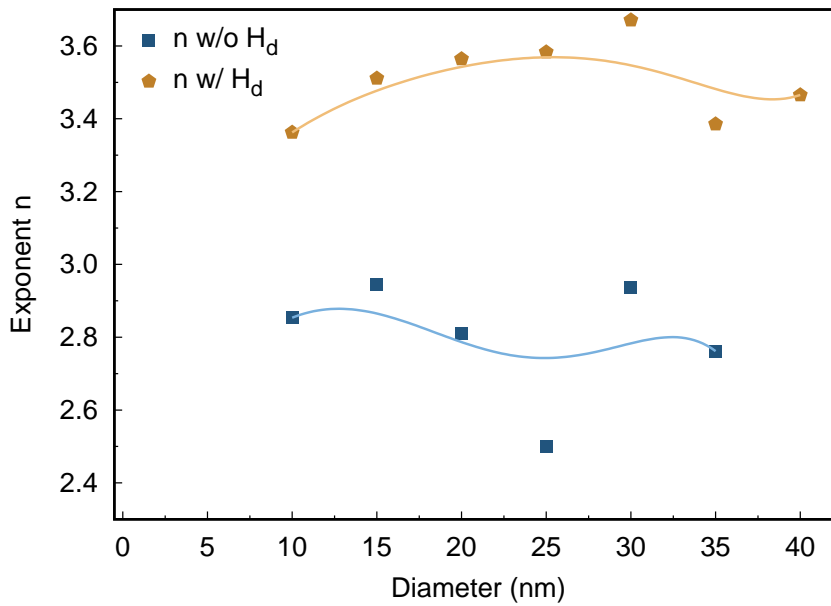
Figure 6.9 Disc diameter dependence of the scaling exponent n determined by fitting the relationship 6.7. Lines describe a trend and serve as guide for the eyes.

we observe this transition, 25 nm and 35 nm without and with magnetostatic, respectively, correspond to the transition of reversal mechanism from coherent to domain nucleation, as it can be seen in Figure 6.3. The analysis of the temperature dependence of the energy barrier and K_{eff} endorses the interpretation of a change in the reversal mechanism from coherent to nucleation as the disc size increases. Similar conclusions are drawn by Sato *et al.* [71], Takeuchi *et al.* [63]. In these works they assume a uniform reversal for small

in-plane dimensions and nucleation for larger diameters. Enobio *et al.* [83] assume a different reversal mechanism to overcome the energy barrier other than nucleation. Enobio and co-workers infer the nature of the switching from the linear dependence of the energy barrier with the diameter, despite such trend is usually assumed a fingerprint of nucleation. Enobio *et al.* [83] extract the temperature dependence of the energy barrier from which they derive that of the effective anisotropy, and obtain the scaling exponents between the magnetisation and K_{eff}. The exponents obtained in the work from Enobio *et al.* [83] agree with our results when the magnetostatic contribution is included in the simulations, showing values larger than expected for uniaxial materials. The reason for these values is unclear and Enobio and co-workers [83] attribute it to edge effects caused by the fabrication process. The results for the temperature dependence of K_{eff} show that the miniaturisation of the system dimensions, required to progress technologically, involves more complex properties than in bulk and requires an appropriate modelling as it goes beyond macroscopic approaches.

6.6 Comparison with experimental size dependence of the energy barrier

We compare our simulated data for the size dependence of the energy barrier at room temperature with experimental results from Sato *et al.* [71], Takeuchi *et al.* [63], Enobio *et al.* [83]. The comparison is shown in Figure 6.10, where red dots represent the simulated data, blue squares (Sato-1) and light-blue downwards triangles (Sato-2) refer to series1 and series2 of [71], respectively. Takeuchi (orange diamonds) and Eunobio (brown upwards triangles) are obtained from [63, 83], respectively. Takeuchi *et al.* [63] and Enobio *et al.* [83] investigate MTJs composed of a single CoFeB/MgO free layer with $K_{\text{eff}} \sim 1.5 \times 10^5\,\text{Jm}^{-3}$, $M_{\text{s}} \sim 1.3\,\text{T}$ and $A_{\text{s}} \sim 20 \times 10^{-12}\,\text{Jm}^{-1}$ and $K_{\text{eff}} \sim 1.9 \times 10^5\,\text{Jm}^{-3}$, $M_{\text{s}} \sim 1.3\,\text{T}$ and $A_{\text{s}} \sim 30 \times 10^{-12}\,\text{Jm}^{-1}$, respectively. The MTJs with MgO/CoFeB/Ta/CoFeB/MgO as recording layer studied by Sato *et al.* [71] are characterised by a free layer with $K_{\text{eff}} \sim 1.5 \times 10^5\,\text{Jm}^{-3}$, $M_{\text{s}} \sim 1\,\text{T}$ and $A_{\text{s}} \sim 19 \times 10^{-12}\,\text{Jm}^{-1}$ and have higher thermal stability. The stability factor obtained from our simulations is in good agreement with the results from Sato *et al.* [71], in particular for diameters smaller than 35 nm, whereas the data obtained by Takeuchi *et al.* [63] and Enobio *et al.* [83] are obtained for larger diameters and exhibit a lower stability. It is worth noting that we perform simulations for a single CoFeB/MgO layer of thickness 1.0 nm, which corresponds to the hard ferromagnetic layer in a MTJ. We have simulated neither the free layer nor the whole MTJ stack for the sake of computational efficiency, due to the long time required by cMC simulations. While we do not expect qualitative difference between
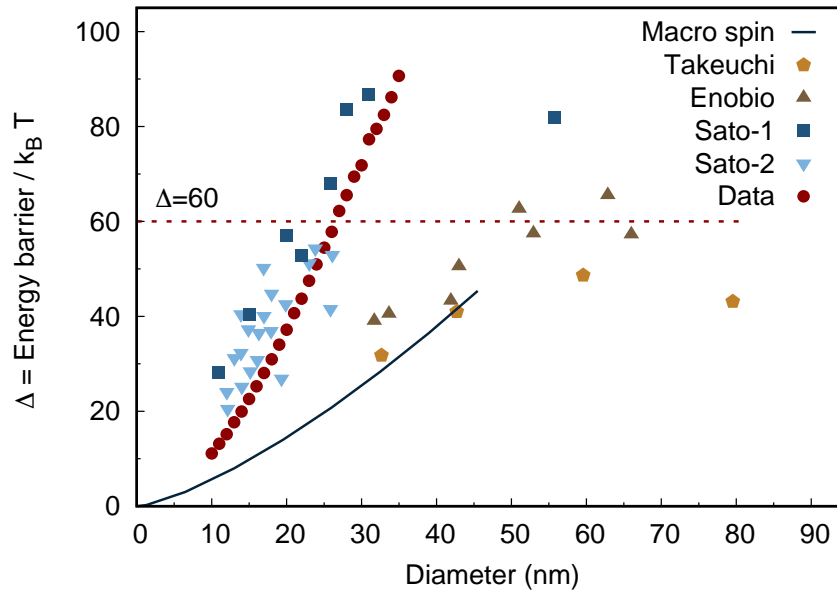
Figure 6.10 Comparison among simulated (red dots) stability factor (Energy barrier/k_BT) as function of diameter for CoFeB/MgO dots at 300 K and experimental results from references [71, 63, 83]. Sato-1 (blue squares) and Sato-2 (light-blue downwards triangles) refer to series1 and series2 of [71], respectively. Takeuchi (orange diamonds) and Eunobio (brown upwards triangles) are obtained from [63, 83], respectively. The dark solid line represents the macrospin model for the 1.3 nm CoFeB/MgO layer and the red dashed line marks the minimum stability requirement for storage devices at room temperature, $\Delta = 60$.

the presented results and simulations performed on the softer 1.3 nm layer, the 1.0 nm CoFeB/MgO is more thermally stable due to a stronger uniaxial anisotropy. To confirm it, we calculate the expected diameter dependence of the stability factor for thickness of 1.3 nm. The solid line in Figure 6.10 shows the stability factor calculated using the macrospin model where the anisotropy energy density is derived from the atomistic parameters. The estimated single domain size from our parameter is around 35 nm-40 nm. The experimental data seem to agree with the model describing a 1.3 nm CoFeB/MgO system. Moreover, we observe a change in the size dependence of the experimental stability factors in correspondence of the expected single domain size. Therefore, we can reasonably assume that simulations performed on a thicker CoFeB/MgO structure or on the whole MTJ stack would yield a good agreement with the experimental measurements of Takeuchi *et al.* and Enobio *et al.*. It is worth noting that a double MgO free layer MTJ has a larger magnetocrystalline anisotropy than a single free layer system due to the doubling of the CoFeB/MgO interface. In these structures the free layer is also less sensitive to the stray field arising from the pinned layer. Therefore, the excellent agreement between experiments performed on a MTJ with double MgO recording layer and

our simulations of a single CoFeB/MgO disc can be understood if we take into account that we simulated a system whose properties are closer to those of a double MgO free layer MTJ.

These results demonstrate how the use of an atomistic spin model allows the calculation of the energy barrier for realistic size of MTJs and similar structures at technologically relevant temperatures. The values obtained from the simulations are close to experiments, even in the nucleation regime where the magnetostatic contribution needs to be accurately accounted for. Nonetheless, further studies are required to achieve a complete understanding of an important parameter such as the energy barrier.

6.7   Conclusions

We investigated the size and temperature dependence of the energy barrier in CoFeB/MgO-based nano discs via an atomistic spin model. A transition from coherent to domain wall mediated reversal occurs around the single domain wall size causing a reduction in the energy barrier. At finite temperature this transition is not sharp. An analytic description able to characterise this region which is of great technological interest is not available and, therefore, further modelling efforts are necessary. Besides, an approach to include magnetostatic interactions in case of non-uniform magnetisation is required to correctly estimate the shape anisotropy, since the use of the macroscopic demagnetisation factors leads to an inaccurate estimation of this contribution. Despite these difficulties, the atomistic spin model is a useful and effective tool to calculate the effective anisotropy and energy barrier at finite temperatures. It allows to achieve a good agreement with experimental measurements for similar systems which are at the state of the art. It can also provide guidance to experiments identifying suitable materials and MTJ stacks with the desired thermal stability. In this work we also studied the effect of a weak applied field along one of the stable directions of the magnetisation on the energy barrier of the system. In the size range investigated, the field does not seem to affect the nature of the reversal significantly, although was not possible to access a clear agreement or disagreement with the available analytic expressions. The dependence of the energy barrier on the relative orientation between applied field, easy axis and magnetisation for non-uniform reversal is of interest for numerous applications as it determines the switching field of the system. The investigation of this aspect will be the object of future work.

Chapter 7

Spin transfer torque switching dynamics in CoFeB/MgO MTJ

STT MRAM is based on the spin transfer torque mechanism in order to write the bit, stored as the polarisation of the free layer, and the magnetisation reversal determines the switching properties of such devices. Therefore, an understanding at the fundamental level of the mechanism via which the magnetisation is reversed under the application of a spin-polarised current is of great interest. The available models developed to describe the spin torque phenomenon rely on micromagnetic modelling. Micromagnetism is limited due to the reduced dimensions of the investigated systems, which brake the assumption of a continuous description, and the necessity to study finite temperature effects. These factors call for the use of an atomistic approach to describe accurately the spin torque phenomenon. We model the spin polarised induced switching dynamics based on Slonczewski's approach [18] parametrised using the spin accumulation model of Zhang *et al.* [93], and we adapt it to an atomistic level. In the following the fundamentals of the spin transfer torque are presented together with the computational approach used to model this phenomenon. After this introduction, the main results related to the switching dynamics in MTJ systems due to spin polarised current are discussed.

7.1 Spin transfer torque

Spin transfer torque (STT) is a phenomenon predicted independently by Berger [17] and Slonczewski [18] in magnetic multilayer structures that allows to switch the magnetisation of one of the layers via injection of an electrical current. In the following, Slonczewski's approach and the spin accumulation model are presented. Afterwards, the computational approaches used to investigate the dynamics of the magnetisation induced by a spin polarised current are described.

7.1.1   Slonczewski's model

In general, when a flux of electrons crosses a ferromagnetic material, a transfer of angular momentum from the conduction electrons to the local magnetisation occurs due to the $s-d$ exchange interaction between s (conduction electrons) and d (electrons responsible for the magnetic behaviour in transition metals) electrons. This transfer of angular momentum causes a torque to be exerted on the local magnetisation and a restoring torque on the conduction electrons. Slonczewski considered a trilayer stack composed of two ferromagnets separated by a thin non-magnetic metal [18, 94]. If we assume that the magnetisation of one of the ferromagnets is pinned (FM1), i.e. its magnetisation is fixed along a specific direction, when a current perpendicular to the stack is injected in FM1 and the electrons cross the layer, their spin aligns along the direction of the magnetisation and the current becomes spin polarised. The current flows through the non-magnetic spacer and enters the second ferromagnetic layer (FM2), whose magnetisation is pointing along a different direction with respect to that of FM1. A torque is exerted on the local magnetic moments within FM2 to obey the requirement of conservation of angular momentum, via the $s-d$ exchange interaction. This torque can induce a reorientation of the local magnetic moments along the direction of FM1 polarisation, resulting in the switching of the magnetisation.

7.1.2   Spin accumulation model

Zhang *et al.* [93] developed a model of the spin transfer torque in multilayer magnetic structures where the spin torque is described in terms of an interaction between the local magnetisation of a magnetic material and spin accumulation, which is a local deviation of the spin density from equilibrium. In this approach [93, 95] based on the drift-diffusion model, a spin polarised current builds a spin accumulation when it crosses a ferromagnetic material. This spin build up continues until the spin current reaches a steady state, which takes about 1×10^{-12} s. There are two main length scales involved with the spin diffusion process: the spin diffusion length (λ_{sdl}) and the exchange length (λ_{J}). λ_{sdl} is the average distance that an electron travels before flipping its spin, and it is of the order of 60 nm in Co and larger in non-magnetic metals. λ_{J} is related to the transfer of angular momentum between the incident spin polarised electrons and the local magnetic moments via the $s-d$ exchange, and it is of the order of few nanometres. Two components of the spin accumulation can be distinguished: a longitudinal component that is parallel to the local magnetisation and a perpendicular spin accumulation orthogonal to the local moments within the ferromagnet. The latter is generated within λ_{J} from the interface due to the non-collinearity between the spin current and the local magnetisation, whilst the former decays on a λ_{sdl} length scale. Within a λ_{J} distance, the transverse spin accumulation

interacts with the local magnetisation exerting a torque on this in order to conserve the angular momentum. For torques large enough, the magnetisation of the ferromagnet can be rotated to be collinear with the spin polarised current, resulting in the switching of the layer polarisation. To be noted that the rotation of the magnetisation occurs on a longer time scale than the relaxation of the spin accumulation, on the order of 1×10^{-9} s and 1×10^{-10} s.

7.1.3   LLG equation with spin transfer torque

The LLG equation of motion that describes the dynamics of the magnetisation in absence of spin transfer torque was presented in Section 2.5.2. To include the spin torque term, we base our formalism on Slonczewski's approach [18] and we follow the work of Zhang *et al.* [93, 95, 96] to parametrise it. We note that the aforementioned approaches are based on the macrospin theory, hence we adapt these to an atomistic formalism considering individual spin moments within the magnetic layers instead of a single macro-moment. We start from the spin accumulation form to show how the individual terms of the spin torque emerge and how they can be parametrised from the spin accumulation model.

Due to the $s - d$ exchange interaction (J_{sd}) between the spin polarised electrons and the local magnetisation, which can be described by an interaction between the spin accumulation $\vec{m}$ and the local magnetisation $\vec{M}$ as

$$\mathcal{H} = -J_{sd}\vec{m} \cdot \vec{M}, \tag{7.1}$$

the equation of motion of the magnetic moments (Equation 2.17) is modified into:

$$\frac{d\vec{S}_i}{dt} = -\frac{\mu_0 \gamma}{(1 + \alpha^2)} \left[\vec{S}_i \times \vec{H}_{eff}^i + \alpha \vec{S}_i \times \left(\vec{S}_i \times \vec{H}_{eff}^i \right) \right] - \frac{\mu_0 \gamma}{(1 + \alpha^2)} \left(\vec{S}_i \times J_{sd}\vec{m} \right) \tag{7.2}$$

where $J_{sd}\vec{m}$ is the effective field due to the coupling between the local magnetic moments ($\vec{S}_i$) and the spin accumulation ($\vec{m}$) and the other terms are as in Equation 2.17. The spin accumulation can be expressed as function of the magnetisation of the layer that polarises the current ($\vec{M}_p$) and the local moments as [93, 95–97]:

$$J_{sd}\vec{m} = -a_{je}\vec{S}_i \times \vec{M}_p - b_{je}\vec{S}_i \times \left(\vec{S}_i \times \vec{M}_p \right), \tag{7.3}$$

where $\vec{M}_p$ is the normalised unit vector describing the magnetisation of the pinned layer, a_{je} and b_{je} are the adiabatic (AST) and non-adiabatic spin torque (NAST) parameters and have units of field. The first term on the RHS of Equation 7.3 is due to the exchange interaction between the spin polarised conduction electrons and the local moments. This
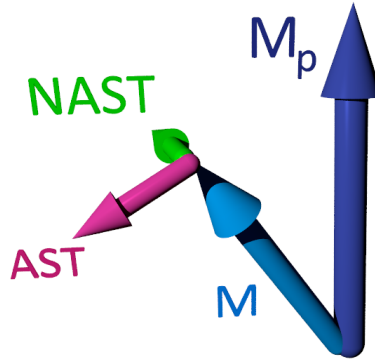
Figure 7.1 Illustration of the contribution of the adiabatic (AST) and non-adiabatic (NAST) spin torque components to the dynamics of the local magnetisation in the free layer $\vec{\mathrm{M}}$. AST orients in the plane defined by $\vec{\mathrm{M}}$ and $\vec{\mathrm{M}}_{\mathrm{p}}$, whereas the direction of NAST or field-like torque is perpendicular to that plane.

interaction tends to align the conduction electrons along the magnetisation direction. The second is associated with the spacial mistracking of the conduction electrons and the local moments [98], spin flip scattering and momentum transfer [99]. However, the origin and the understanding of this term are still subject of study [97]. a_{je} and b_{je} depend on the injected electrical current density and on the structural, geometrical and diffusive properties of the layers, as it will be shown later.

Substituting the expression for $J_{\mathrm{sd}}\vec{m}$ into Equation 7.2, the modified LLG equation reads:

$$\frac{d\vec{S}_i}{dt} = -\frac{\mu_0\gamma}{(1+\alpha^2)}\vec{S}_i \times \vec{\mathrm{H}}_{\mathrm{eff}}^i - \frac{\mu_0\gamma\alpha}{(1+\alpha^2)}\left[\vec{S}_i \times \left(\vec{S}_i \times \vec{\mathrm{H}}_{\mathrm{eff}}^i\right)\right]$$

$$-\frac{\mu_0\gamma b_{\mathrm{je}}}{(1+\alpha^2)}\left(\vec{S}_i \times \vec{\mathrm{M}}_{\mathrm{p}}\right) + \frac{\mu_0\gamma a_{\mathrm{je}}}{(1+\alpha^2)}\left[\vec{S}_i \times \left(\vec{S}_i \times \vec{\mathrm{M}}_{\mathrm{p}}\right)\right] \qquad (7.4)$$

The first two terms on the RHS of Equation 7.4 are the usual precessional and damping terms responsible for the damped precessional motion in the direction of the local field $\vec{\mathrm{H}}_{\mathrm{eff}}^i$. The last two terms describe the effect of the spin torque on the spin motion in the presence of an injected current. These contributions show that the spin torque can act as an extra source of both precession and damping via the third and fourth term, respectively. The former, or non-adiabatic spin torque (NAST), can be seen as the interaction of the background magnetisation with an effective field $b_{\mathrm{je}}\vec{\mathrm{M}}_{\mathrm{p}}$. This can affect the precession induced by $\vec{\mathrm{H}}_{\mathrm{eff}}$ and can be interpreted as the current creating a magnetic field on the local moments. For this reason it is also defined field-like torque. The latter is a damping contribution whose sign depends on the direction of the injected current. If the damping due to the spin torque and the natural damping point along the same direction, the damping

of the system is enhanced and the local magnetisation relaxes towards $\vec{H}_{eff}$. However, when the two damping terms are opposite, the damping of the system decreases and precessional states can be induced. For critical current densities a stable precession of the magnetisation can be excited, and this is the mechanism used in spin torque oscillators [100]. For larger current densities, the reversal of the magnetisation can occur. This contribution is usually referred to as adiabatic spin torque (AST) or Slonczewski torque. Figure 7.1 illustrates the spin torque components within a macrospin formalism for the sake of simplicity and clarity, where $\vec{M}$ and $\vec{M}_p$ denote the magnetisation in the free and pinned layer, respectively. AST orients in the plane defined by $\vec{M}$ and $\vec{M}_p$. Therefore, AST acts on the angle between them either increasing or decreasing it, depending on the injected current. The direction of NAST is perpendicular to such a plane, as clear from Equation 7.4. Because of the orientations of AST and NAST, these terms are also referred to as in-plane and perpendicular torque, respectively. We note that usually the contribution describing the spin torque is added to the implicit form of the LLG equation

$$\frac{d\vec{S}_i}{dt} = -\mu_0\gamma\vec{S}_i \times \vec{H}_{eff}^i + \alpha\vec{S}_i \times \frac{d\vec{S}_i}{dt}. \tag{7.5}$$

Doing so yields the same adiabatic and non-adiabatic terms, but the coefficients in front of $\vec{S}_i \times \vec{M}_p$ and $\vec{S}_i \times \left(\vec{S}_i \times \vec{M}_p\right)$ differ due to the presence of the damping α: $a_{j_e} \rightarrow a_{j_e} + \alpha b_{j_e}$ and $b_{j_e} \rightarrow b_{j_e} - \alpha a_{j_e}$. Since there are not large variations in the values of the coefficients because α is small in the systems we investigate, we have decided to use the form presented in Equation 7.2, despite this is not the most correct formalism.

The spin torque parameters a_{j_e} and b_{j_e} represent the strength of the two components AST and NAST of the torque generated by the interaction of the local magnetisation with the spin polarised current. We follow the approach presented by Zhang *et al.* [93] for a trilayer magnetic system consisting of a pinned ferromagnetic layer, a spacer and a ferromagnetic layer, with current injected perpendicular to the stack to determine a_{j_e} and b_{j_e}. Zhang *et al.* [93], averaging over the thickness of the free layer (t_F), obtain expressions for a_{j_e} and b_{j_e} that are proportional to the current density j_e:

$$a_{j_e} = -\frac{j_e\hbar a_0^3}{\sqrt{2}e\mu_B\lambda_J}\left[\frac{1-\cos(\xi)e^{-\xi}}{\xi}\right] \tag{7.6}$$

$$b_{j_e} = \frac{j_e\hbar a_0^3}{\sqrt{2}e\mu_B\lambda_J}\left[\frac{\sin(\xi)e^{-\xi}}{\xi}\right], \tag{7.7}$$

where $\xi = t_F/\left(\sqrt{2}\lambda_J\right)$, $\hbar = 1.055 \times 10^{-34}$ Js is the reduced Planck constant, a_0 is the lattice constant of the layer, $e = 1.602 \times 10^{-19}$ C is the electric charge and $\mu_B = 9.274 \times 10^{-24}$ Am^2 is the Bohr magneton. $\lambda_J = \sqrt{2\hbar D_0/J_{sd}}$ represents the length scale

over which the spin polarised electrons and the background moments interact, where D_0 is the diffusion constant of the free layer and J_{sd} is the exchange energy between the spin polarised electron and the magnetisation described above. $\lambda_J \approx 3\text{–}4$ nm for CoFeB and a_{j_e} and b_{j_e} vary up to fractions of Tesla for typical free layer thickness used in MTJs. We point out that several assumptions have been made by Zhang *et al.* [93] to determine the magnitude of the coefficients a_{j_e} and b_{j_e}. The magnetic structure is composed of a very thick ferromagnet whose magnetisation is pinned, a barrier infinitely thin so that the polarisation of the current is preserved during the crossing from one ferromagnet to the other since there is not spin-flip scattering in this region, and a thin ferromagnet. The spin-dependent scattering at the interfaces is neglected, ensuring that all the current is absorbed, and the pinned layer is a half metal, which yields full spin-polarisation of the injected current density. To simplify further the calculations the limit $\lambda_{sf} \gg \lambda_J$ is taken, where λ_{sf} is the characteristic length scale over which the conduction electrons relax [93]. This assumption, which holds for CoFeB/MgO systems where $\lambda_J \approx 3$ nm and $\lambda_{sf} \approx 15$ nm [101, 97], ensures that the polarisation is conserved. In addition, the magnetisation is supposed to be uniform within each magnetic layer. This allows to describe each single layer via a single macro spin simplifying the discussion.

If instead of averaging over t_F one considers the contribution of each single atomic layer in the ferromagnets, a_{j_e} and b_{j_e} can be obtained layer resolved:

$$a_{j_e}(x) = \frac{j_e \hbar a_0^3}{\sqrt{2} e \mu_B \lambda_J^2} \frac{1}{t_l} \int_{t_i}^{t_f} dx \lambda_J e^{-\frac{x}{\sqrt{2}\lambda_J}} \left[\cos\left(\frac{x}{\sqrt{2}\lambda_J}\right) + \sin\left(\frac{x}{\sqrt{2}\lambda_J}\right) \right] \tag{7.8}$$

$$b_{j_e}(x) = \frac{j_e \hbar a_0^3}{\sqrt{2} e \mu_B \lambda_J^2} \frac{1}{t_l} \int_{t_i}^{t_f} dx \lambda_J e^{-\frac{x}{\sqrt{2}\lambda_J}} \left[\cos\left(\frac{x}{\sqrt{2}\lambda_J}\right) - \sin\left(\frac{x}{\sqrt{2}\lambda_J}\right) \right]. \tag{7.9}$$

Here t_l is the thickness of a single atomic layer and depends on a_0, whereas t_i and t_f are the vertical coordinates of the atomic layer which the integration is carried over, and x is the integrated thickness. Such approach allows to go beyond the approximation of uniform magnetisation within the ferromagnetic layers, yielding a spin torque which varies within the ferromagnet. This parametrisation is most suitable for an atomistic spin model where the atomic spin moments are taken into account individually and there are not requirements for uniform magnetisation. Figure 7.2 shows the thickness dependence of a_{j_e} and b_{j_e} obtained from Equations 7.8-7.9 for a multilayer structure CoFeB(1.0 nm,PL)/MgO(0.85 nm)/CoFeB(1.3 nm,FL) such as those investigated in section 5.5, where λ_J for CoFeB is used. The average a_{j_e} and b_{j_e} predicted by Equations 7.6-7.7 are plotted with lines as a comparison. Here thickness = 0 marks the interface MgO/CoFeB(FL) and increasing thickness corresponds to go farther away from the interface. The spin torque parameters are normalised with respect to a_{j_e} largest value, which
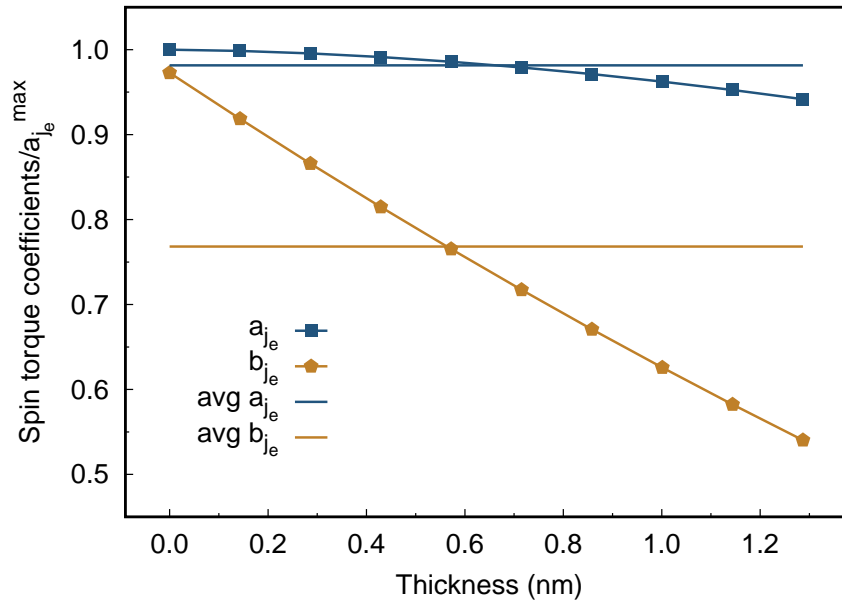
Figure 7.2 Thickness dependence of spin torque coefficients normalised by the largest a_{j_e}, which occurs at the interface and marked by thickness = 0, obtained integrating Equations 7.8-7.9 for CoFeB(1.0 nm,PL)/MgO(0.85 nm)/CoFeB(1.3 nm,FL) magnetic structure. Constant lines mark the average a_{j_e} and b_{j_e} predicted by Equations 7.6-7.7.

occurs at the interface with the barrier. This makes the discussion independent of the current density value. We note that a_{j_e} and b_{j_e} are characterised by different thickness dependences: NAST decreases faster and reaches almost 50% of its initial value, whereas AST remains almost constant within less than 1.5 nm. It is important to observe that the strength of both AST and NAST are comparable close to the interface between the ferromagnet and the barrier. Therefore, even if b_{j_e} decays rapidly within the ferromagnet, the field-like torque should be taken into account in the dynamics of the magnetisation, whilst it is often neglected [1, 73, 74, 102]. Furthermore, taking the average value could lead to a severe underestimation of the effect of NAST, as the torque is mainly originated at the interface.

With the layer resolved spin torque parameters and the inclusion of the field-like term an extra degree of information is added within the model with respect to a simple Slonczewski's approach. Nonetheless, the torque is assumed uniform in each plane. This approximation is not necessarily valid in finite systems, where for instance the magnetostatic interactions would lead to non-uniform magnetic configurations close at the edges of the system. Non-uniform magnetisation can be also caused by finite temperature as this induces random fluctuations of the spin moments. To go beyond this limitation, an approach which derives the spin transfer torque acting on the background magnetisation from calculation of the dynamics of the spin accumulation needs to be

applied. A viable method based on the calculation of the spin accumulation is briefly outlined in the next section.

7.1.4   Calculation of spin torque via spin accumulation

Chureemart *et al.* [103, 97] developed a self-consistent approach to calculate the spin transfer torque acting on the magnetisation when a spin-polarised current is injected into a magnetic system. Because of the different characteristic time scales of the spin accumulation and magnetic moments, the dynamics of these two quantities can be solved separately. Initially, the dynamics of the spin accumulation is solved, where the solution is separated into the longitudinal and perpendicular components. Note that the spin accumulation is calculated in a rotated reference system that is parallel and perpendicular to the local magnetisation for the sake of simplicity. Once the spin accumulation has been solved, the torque acting on the magnetic moments can be calculated via the $s - d$ exchange interaction by means of Equation 7.2. Due to the rotated frame, only the transverse component of the spin accumulation contributes to the torque, as the longitudinal component is parallel to the local magnetisation and does not produce any torque. Details of the methods can be found in [103, 97].

7.2   Analysis of the switching mechanism

In the following we present two techniques for the analysis of the switching mechanism other than the study of the time and current density dependence of the magnetisation components. We then discuss the approach used to investigate the switching time of MTJ systems. After the methods are outlined, in the next section we apply these to our result for the switching of the magnetisation in MTJs induced by spin polarised currents.

7.2.1   Contour integral

To understand the nature of the mechanism which governs the reversal of the magnetisation in MTJs under application of a spin polarised current, we develop an analysis based on performing a contour integration of the magnetisation. The method involves integrating over a 2D slice of the ferromagnet, weighting the integral over the coordinates by the magnetisation. Since the contour integration is performed in the complex space, we consider the complex plane whose real and imaginary axes are the in-plane coordinates of the atomic moments within the layer x and y, respectively. The new complex variable is $c = x + iy$, where i is the imaginary unit. To perform the contour integral P, we can split the calculation in two parts: a line integral around a circular path of radius r and an

integration from zero to the dot diameter along the real axis. Each single point $c = (x, y)$ in the complex plane has associated a perpendicular component of the magnetisation $M(c)$ and we can run the integration weighting c by its $M(c)$ over a finite region. Clearly, this analysis would work for any component. Thus, P can be expressed as:

$$P = \int_r^{r+dr} \oint_\Gamma M(c, r) dc dr, \tag{7.10}$$

where Γ is the closed curve around a circle of radius r in the complex plane.

For simplicity, we consider the case of uniform magnetisation $M(c) = \text{const}$ first. Since $M(c)$ is constant, $M(c)$ can be taken out of the integral and the integral is directly related to the integral around the unit circle in the complex space defined by $x = \Re(c)$ and $y = \Im(c)$. In this simple case we can also neglect the integral $\int_r^{r+dr} dr$ as this corresponds to a multiplication of the integration over Γ by the number of annuli used to calculate P. This new integral F is given by:

$$F = \oint_\Gamma dc. \tag{7.11}$$

The total integral F in Equation 7.11 can be calculated applying the coordinate transformation $x = \cos\vartheta$ and $y = \sin\vartheta$. Doing so F reads:

$$\begin{aligned} F &= \oint_\Gamma dc = \int_0^{2\pi} (dx + i dy) = \int_0^{2\pi} (-\sin\vartheta + i\cos\vartheta) d\vartheta \\ &= \cos\vartheta + i\sin\vartheta. \end{aligned} \tag{7.12}$$

We can now divide the integration range in two: $0 < \vartheta \le \pi$ and $\pi < \vartheta \le 2\pi$, where ϑ is the angle locating each point c. The two new integrals F_- and F_+ associated with the two ranges are:

$$F_- = \int_0^\pi dc, \qquad F_+ = \int_\pi^{2\pi} dc. \tag{7.13}$$

Applying the same approach to F_- and F_+ one obtains $F_- = -2$ and $F_+ = +2$, so that for uniform magnetisation $F = F_- + F_+ = 0$. If we now introduce a domain wall such that the upper half plane has $M(c) = 1$ and the lower half plane has $M(c) = -1$, we obtain $F = F_- - F_+ = -4$. Similarly, if the reversed magnetisation is in the upper half plane, $F = -F_- + F_+ = 4$. Therefore, the effect of the complex notation is to impose a direction on the integration such that the integral over the dot vanishes for the uniform mode. Consequently, non-zero values are indicative of non-uniform magnetisation states. If we now rotate the domain wall separating the two opposite magnetised region in the plane, the value of the integral will oscillate between $+4$ and -4 depending on the position of

the domain wall. The magnitude of the integral indicates the degree of non-uniformity of the magnetisation and the time variation of the phase angle is related to the precession.

This method can also be used to obtain space resolved informations about the reversal mechanism. If a domain is generated at the edge of the system for instance, then value of P will depend, at a specific instant, on which region the integral is calculated over. Hence, we can divide the dot in concentric annuli of constant thickness and calculate the contour integral in each of the regions. Figure 7.3(a) shows the subdivision of a 20 nm
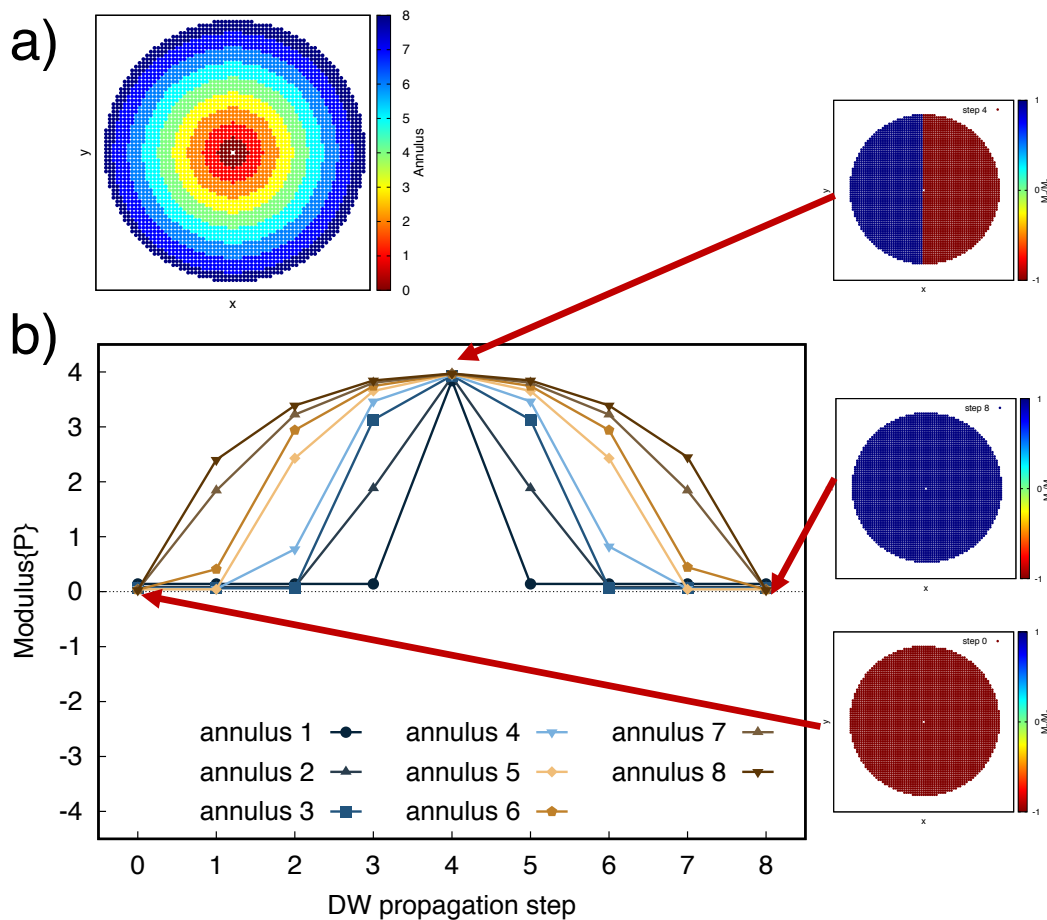
Figure 7.3 (a) Top view of a 20 nm dot showing the division of the system in concentric annuli each with a thickness of about 2.5 nm. The colour palette marks different annuli. (b) Modulus of the contour integral P calculated for the dot shown (a) when a domain with domain wall along the y-direction is introduced into the system and then propagates until the full reversal of the magnetisation is achieved. The insets show the magnetic configuration of the system in the initial and final states and when domain wall is in the centre of the dot. The colour scheme describe the z-component of the magnetisation (red=-1, green=0, blue=+1).

dot in annuli of about 2.5 nm each. We note that the annuli must have a finite width to approximate a continuum description of the magnetisation. In Figure 7.3(b) the modulus

of P resolved by annulus is calculated for a test case: a domain originates at one edge of the system, shown in Figure 7.3(a), and propagates through the system without any rotation of the domain wall. In addition, the domain wall is assumed to be infinitely thin. P is zero for the outer regions when the magnetisation is uniform, i.e. before the domain is introduced into the system and after the magnetisation reverses completely, whereas is non-zero during the propagation of the domain. For the most internal regions, P is non-zero only when the domain wall crosses the centre of the system. This simple case shows how the contour integral approach can provide useful information about the magnetisation configuration and its dynamics.

7.2.2   Excitation modes

Recent studies on the instability mechanism driving the magnetisation reversal in spin transfer torque MRAM systems by Visscher *et al.* [102, 84] based on micromagnetic simulations, attributed the nature of the switching to a "magnetostatic instability", excluding edge nucleation processes. In such a case the magnetisation precesses until a critical tilting angle is reached, then the system switches deterministically. Visscher *et al.* [102, 84] base their analysis on the stability of the lowest energy normal modes, which are small perturbation of the equilibrium magnetic state. Visscher and collaborators classify these modes by the winding number ω, an integer index related to the azimuthal angular momentum quantum number. ω can be understood as the number of times the magnetisation of the disc winds around a symmetry axis perpendicular to the plane of the disc when the disc is revolved once. Because of the radial symmetry of the system, the lowest frequency modes m_ω take the form [102, 84]:

$$m_\omega = \int_\Omega (x - iy)^\omega (s_x + is_y)\, dxdy,\qquad (7.14)$$

where x, y, s_x and s_y are the spacial coordinates and the spin values of the atoms within the system, respectively, $i = \sqrt{-1}$ is the imaginary unit, Ω is the surface of the disc and $d_x d_y$ is the surface element which the integration is carried over. $\omega = 0, 1, -1$ for the lowest energy modes and we can express the three excitations as [102, 84]:

$$
\begin{aligned}
m_0 &= \int_\Omega (s_x + is_y)\, dxdy \\
m_1 &= \int_\Omega \left[(xs_x + ys_y) + i\,(xs_y - ys_x) \right] dxdy \\
m_{-1} &= \int_\Omega \left[(xs_x - ys_y) + i\,(xs_y + ys_x) \right] dxdy.
\end{aligned}
\qquad (7.15)
$$

For $\omega = 0$ the mode does not depend on the spacial coordinates, hence the mode must be uniform. This is the lowest energy mode and is defined as the "coherent mode". The other two modes, which differ for the direction of the rotation around the azimuthal axis, represent the first excitation states and are defined as "vortex" ($\omega = 1$) and "anti-vortex" ($\omega = -1$). The three functions described in Equation 7.15 are sketched in Figure 7.4. A
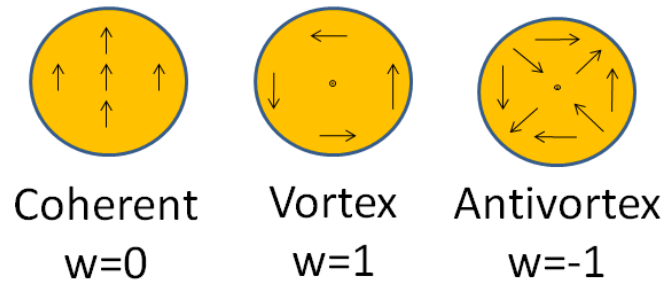
Figure 7.4 Sketch of the lowest three normal modes of the cylinder, labelled by winding number ω, from Visscher *et al.* [102]

similar description of the normal modes in MTJ stacks is discussed in [104]. Naletov *et al.* [104] separate the radial and azimuthal dependences of the modes and find analogous lowest frequency modes.

The contour integral approach discussed in Section 7.2.1 allows to obtain informations about whether the mechanism is coherent and whether there are some spacial dependent non-uniformities. However, it does not provide extra informations regarding the nature of the switching. Accessing the normal modes of the system can shine light on the mechanism, following the works presented in [102, 84, 104]. As the switching process cannot be regarded as a small perturbation of the initial equilibrium state, we rather look at excitation modes which have the same form, but that are not confined to the small excitation regime, as are the real normal modes of the system.

7.2.3 Switching times

The switching time, i.e. the time required to the polarised current to reverse the magnetisation, is one of the most important parameters to characterise a STT MTJ device. Although widely used, in literature it is often not clear how the switching time is defined, which can cause difficulties when discussing and comparing the results. In our work we adopt a definition of the switching time similar to that of Hahn *et al.* [105], where the switching time can be distinguished in two different components: *a*) "transient time" region corresponding to the time required to initiate the reversal and *b*) "reversal time" region where the magnetisation is reversed. We sketch the two switching times in Figure 7.5. The transient time is taken as the time from the start of the simulation until the
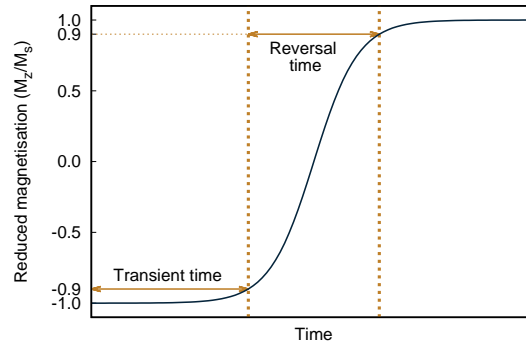
Figure 7.5 Sketch of the *z*-component of the reduced magnetisation as function of time for a switching event. The transient and reversal time regions are indicated on the graph by arrows and dotted lines. The total switching time corresponds to the sum of the transient and reversal times.

z-component of the magnetisation, the component aligned with the anisotropy axis, does not decreases by 10%. The reversal time, that is an intrinsic property of the system at a certain temperature, is considered as the time during which the *z*-component of the magnetisation varies by 80% with respect to its value at the end of the transient time, or equivalently, when the 90% of the magnetisation reverses. Finally, the total switching time is the sum of the transient plus the reversal times.

7.3   Switching dynamics

We study the switching dynamics in MTJs induced by the application of a spin polarised current using the Slonczewski model, described in Section 7.1.3, as function of diameter, applied current and temperature. The system is initialised in an anti-parallel state, with the magnetisation of the pinned layer pointing along the positive *z*-direction and the free layer aligned in the opposite direction. We let the system equilibrate for one nanosecond to allow the magnetisation to reach a relaxed state. Only for simulations performed at $T = 0\,\mathrm{K}$ the free layer magnetisation is misaligned by $1°$ from the *z*-axis to introduce an initial torque acting on the magnetisation. Afterwards, the current is applied to the free layer, where we assume that the electrons acquire spin polarisation when crossing the pinned layer.

7.3.1   Dynamics at zero temperature

Initially, we investigate the magnetisation reversal for diameters of 10, 20, 30 and 40 nm at $T = 0\,\mathrm{K}$ to simplify the analysis without the effect of random thermal fluctuations.

For weak values of the current density applied to the free layer, the reversal occurs in

Figure 7.6 Plot of the simulated switching dynamics of the free layer magnetisation in CoFeB/MgO/CoFeB magnetic tunnel junction stacks at $T = 0\,\mathrm{K}$ for 10 (a), 20 (b), 30 (c), and 40 nm (d) diameters induced by a current density $j_\mathrm{e} = 1 \times 10^{11}\,\mathrm{Am}^{-2}$. Different blue shades represent the x, y and z-components of the magnetisation $\mathrm{M}_{x,y,z}/M_\mathrm{s}$, whereas the reduced magnetisation length $|\vec{\mathrm{M}}|/M_\mathrm{s} = |m|$ is presented in brown.

about a nanosecond. Figure 7.6 shows the time evolution of the reduced magnetisation components of the free layer for $j_\mathrm{e} = 1 \times 10^{11}\,\mathrm{Am}^{-2}$. The in-plane components of the magnetisation exhibit a character typical of uniform precession. Despite the coherent-like behaviour, we observe the appearance of non-uniform features in the magnetisation length for systems larger than 20 nm. The magnetisation length is reduced of almost 25% of the initial value for the 40 nm MTJ and it exhibits oscillations superimposed the main trend. When a larger j_e is applied, the switching is faster and features of non-uniform reversal appear for diameters larger than 10 nm, as shown in Figure 7.7. The magnetisation length decreases of 10% at 20 nm suggesting that the reversal mechanism is affected by the current density, with a transition from coherent to non-uniform switching. When a high current density is applied to the free layer, the in-plane components of the magnetisation exhibit a damped motion until the direction of the magnetisation is reversed. The oscillatory behaviour expected for simple precession is recovered after the
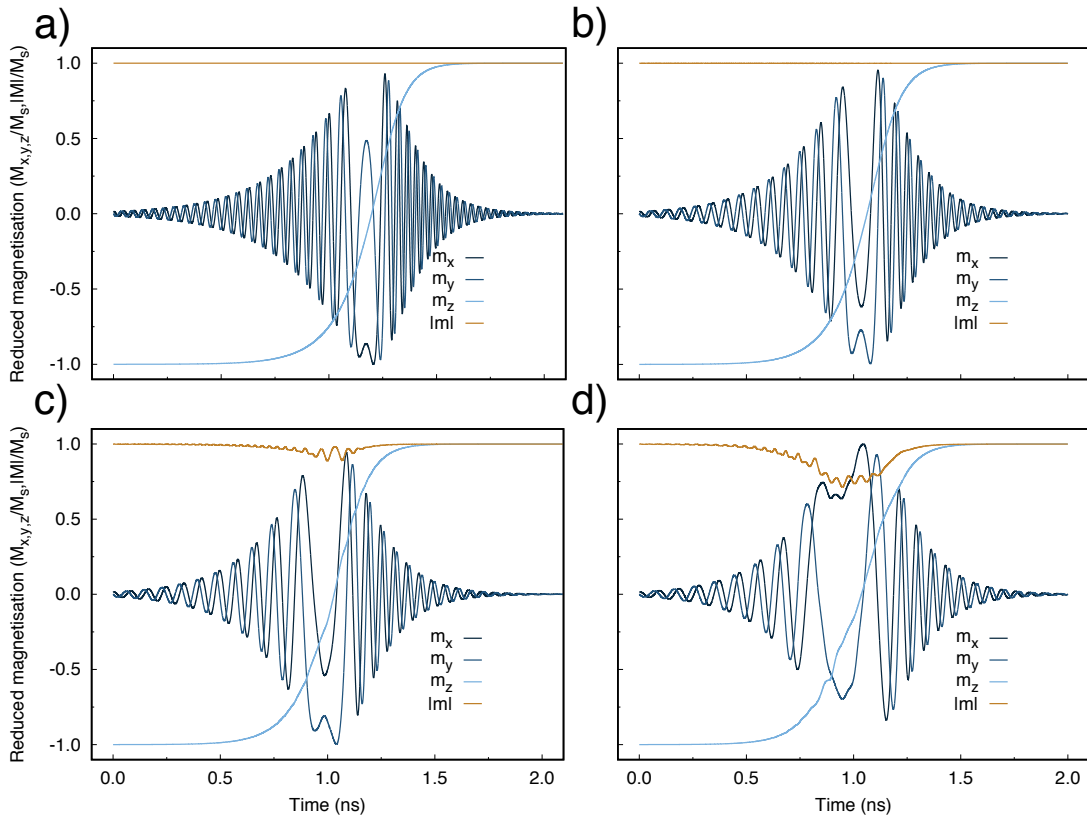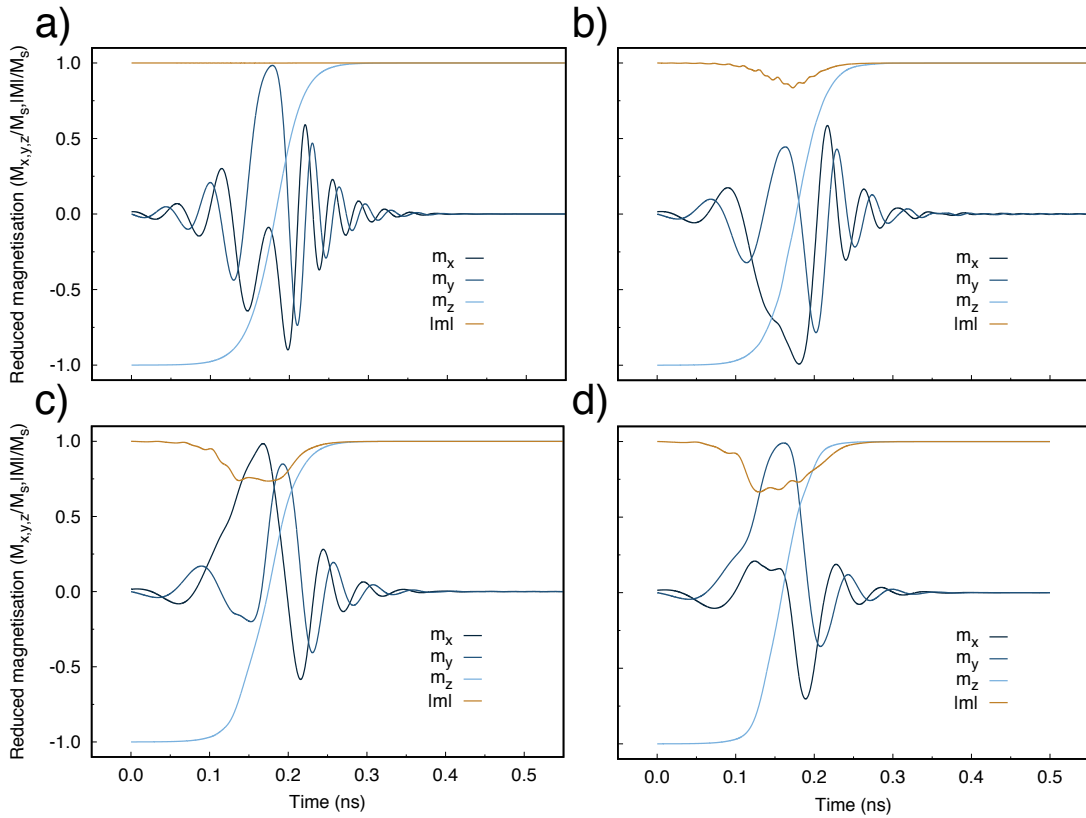
Figure 7.7 Plot of the simulated switching dynamics of the free layer magnetisation in CoFeB/MgO/CoFeB magnetic tunnel junction stacks at $T = 0\,\text{K}$ for 10 (a), 20 (b), 30 (c), and 40 nm (d) diameters induced by a current density $j_\text{e} = 5 \times 10^{11}\,\text{Am}^{-2}$. Different blue shades represent the x, y and z-components of the magnetisation $m_{x,y,z} = \text{M}_{x,y,z}/M_\text{s}$, whereas the reduced magnetisation length $|\vec{\text{M}}|/M_\text{s} = |m|$ is presented in brown.

switching takes place. This behaviour seems to be independent of the diameter, since it is observed in all the investigated cases.

By studying the time evolution of the magnetisation we can obtain a general view of the spin transfer torque dynamics. However, it does not allow to understand fully the dynamics and the nature of the reversal mechanism. For this reason, we calculate the excitation modes and the contour integral of the magnetisation of the system for the different injected currents and diameters. In Figure 7.8 we present a comparison of the calculated amplitudes of the excitation modes of the free layers of 20 nm (left figures) and 30 nm (right figures) MTJs for $j_\text{e} = 1 \times 10^{11}\,\text{Am}^{-2}$ (top figures) and $j_\text{e} = 5 \times 10^{11}\,\text{Am}^{-2}$ (bottom figures). The only mode with non-zero amplitude for $j_\text{e} = 1 \times 10^{11}\,\text{Am}^{-2}$ and diameter 20 nm is the coherent mode m_0, which suggests that the system behaves like a macrospin. The analysis of the magnetic configurations of the free layer during the switching, shown in Figure 7.9(a), confirms the coherent character of the magnetisation reversal, with the rotation of the in-plane components of the magnetisation due to the
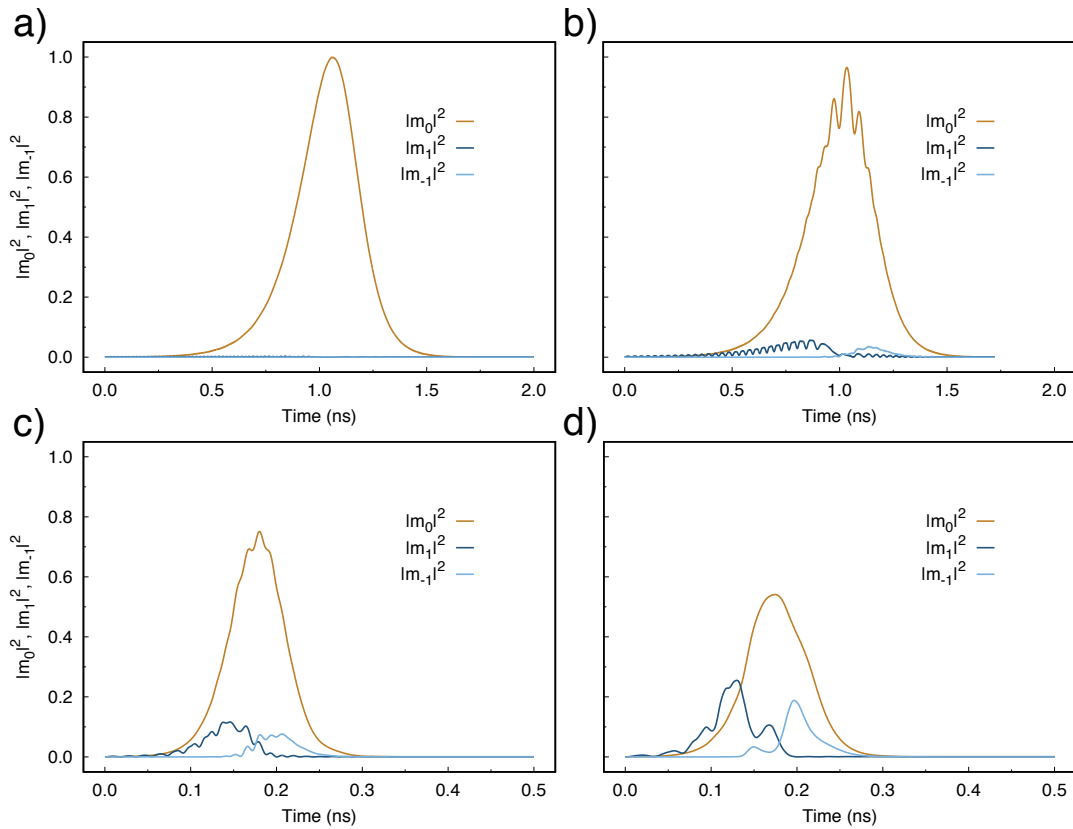
Figure 7.8 Comparison of the calculated amplitudes of the excitation modes of the free layers of 20 nm (left figures) and 30 nm (right figures) MTJs for $j_e = 1 \times 10^{11}\,\mathrm{Am}^{-2}$ (top figures) and $j_e = 5 \times 10^{11}\,\mathrm{Am}^{-2}$ (bottom figures) at $T = 0\,\mathrm{K}$.

nature of the spin torque. Analogous features are found for the smaller diameter. For higher j_e, the amplitude of m_0 decreases and the non-uniform modes become non-zero. Interestingly, we find that only either m_1 or m_{-1} is excited and that a transition from one to the other occurs. This exchange corresponds to the reversal of the winding direction of the in-plane components of the magnetisation from clockwise to counter-clockwise that occurs when the magnetisation changes sign in a vortex. This can be observed in the snapshots of the magnetisation representing the in-plane components, as shown in Figure 7.10. In Figure 7.10 the superimposed coherent mode can also be appreciated. Therefore, this transition between m_1 and m_{-1} excitation modes does not correspond to a change in the reversal mechanism. The same argument applies to the opposite case of transition from m_{-1} to m_1, but we do not observe it since we always initialise the systems in the same configuration. The switching of the magnetisation begins with almost uniform precession where the non-uniform mode m_1 is present with small amplitude. The non-uniform mode causes a small region of the disc to precess faster and to reverse the direction of the magnetisation after a critical tilting angle is exceeded forming a
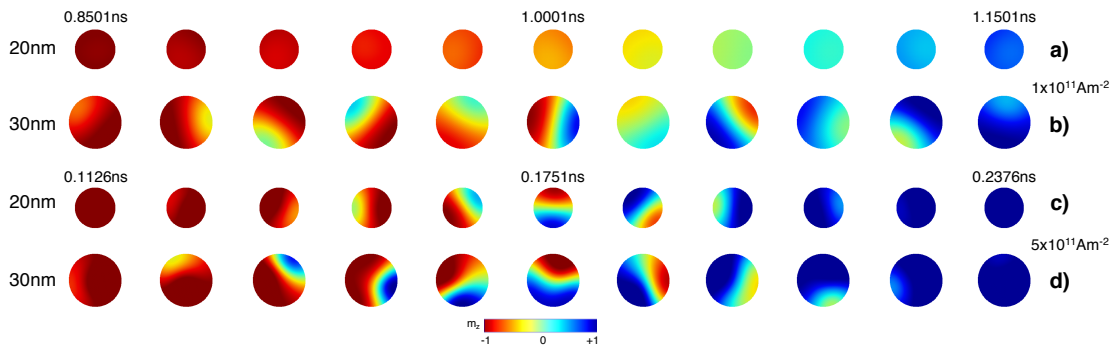
Figure 7.9 Snapshots of spin transfer torque induced magnetisation reversal at $T = 0\,\mathrm{K}$ for the free layer of a MTJ stack of diameter 20 nm (a) and c)) and 30 nm (b) and d)) for $j_\mathrm{e} = 1 \times 10^{11}\,\mathrm{Am}^{-2}$ (a) and b)) and $j_\mathrm{e} = 5 \times 10^{11}\,\mathrm{Am}^{-2}$ (c) and d)). The colour scheme describes the z component of the magnetisation (blue for $+z$, red for $-z$, and green for $z = 0$). The time scale of the switching differs depending on the current density: around a nanosecond for $j_\mathrm{e} = 1 \times 10^{11}\,\mathrm{Am}^{-2}$ and an order of magnitude less for $j_\mathrm{e} = 5 \times 10^{11}\,\mathrm{Am}^{-2}$. The time evolution of the spin configuration shows for b), c) and d) the rotation of the z component of the magnetisation, whilst a coherent mechanism in a).

domain wall. Figure 7.9(c) shows the growth of the of the reversed region until the wall reaches the edge of the disc. A rotational motion is superimposed on the propagation of the domain wall. This phenomenon is clear from the evaluation of the contour integral. Figure 7.11 shows the plots of the real and imaginary components of the contour integral for the annulus with the largest radius. We compare the results for the 20 nm systems with $j_\mathrm{e} = 1 \times 10^{11}\,\mathrm{Am}^{-2}$ and $j_\mathrm{e} = 5 \times 10^{11}\,\mathrm{Am}^{-2}$ in Figure 7.11(a) and Figure 7.11(c). The
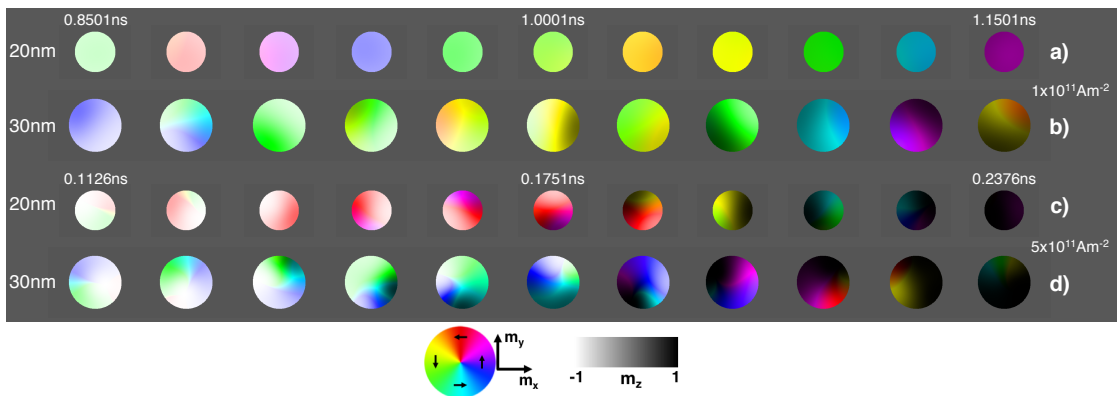
Figure 7.10 Snapshots of spin transfer torque induced magnetisation reversal at $T = 0\,\mathrm{K}$ for the free layer of a MTJ stack of diameter 20 nm (a) and c)) and 30 nm (b) and d)) for $j_\mathrm{e} = 1 \times 10^{11}\,\mathrm{Am}^{-2}$ (a) and b)) and $j_\mathrm{e} = 5 \times 10^{11}\,\mathrm{Am}^{-2}$ (c) and d)). The hue describes the in-plane components of the magnetisation while the intensity of the colour represents the z–component of the magnetisation, as described by the key. A coherent rotation is observed in a), whilst the combination of coherent rotation and non-uniform reversal occurs in the b) and c). A more complex dynamics characterises d).

contour integral is zero for $j_e = 1 \times 10^{11}\,\mathrm{Am}^{-2}$ even in the external region, as expected for coherent reversal. On the other hand, not only are the integral components non zero, but also oscillations of the contour integral can be detected at the edges of the disc when a higher current density is injected. The central regions, for which the results are not presented, exhibit a uniform character, except for when the magnetisation reverses sign. The switching mechanism with the coexistence of a main coherent mode and a weaker non-uniform excitation is similar to that obtained by Visscher *et al.* [102, 84]. However, we observe the rotation of the domain wall throughout the whole reversal process, whereas Visscher *et al.* find a linear propagation of the domain wall from one edge of the system to the other. The reason of the difference in the dynamics is still unclear, although we remark that the rotation of the in-plane components of the magnetisation can be explained by and ascribed to the action of the spin torque. In a micromagnetic description the spin torque has a the form $\vec{M} \times \vec{M}_p$, where $\vec{M}$ is the magnetisation of the free layer and $\vec{M}_p$ the direction of the spin polarised current. Consequently, the spin torque has a component that is in the plane of the free layer and that favours the rotation of the magnetisation.
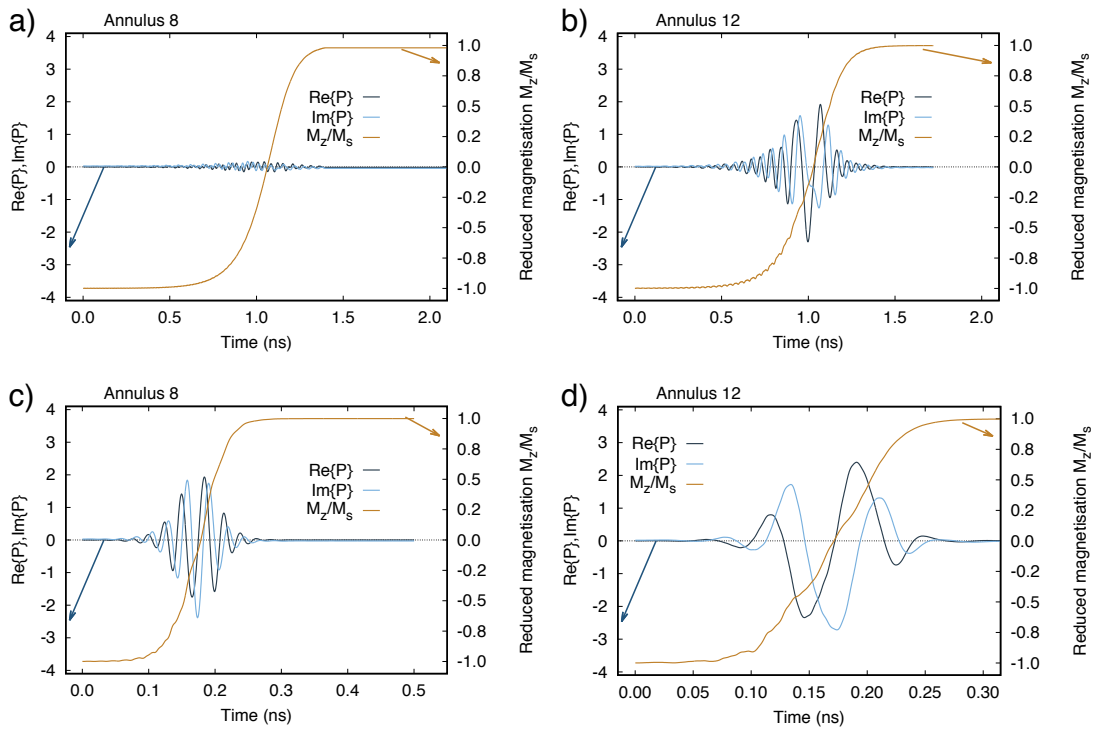
Figure 7.11 Comparison of the calculated components of the contour integral of the magnetisation for the most external annulus of the free layers of $20\,\mathrm{nm}$ (left figures) and $30\,\mathrm{nm}$ (right figures) MTJs for $j_e = 1 \times 10^{11}\,\mathrm{Am}^{-2}$ (top figures) and $j_e = 5 \times 10^{11}\,\mathrm{Am}^{-2}$ (bottom figures) at $T = 0\,\mathrm{K}$. In brown is plotted the magnetisation of the annulus and arrows indicate the *y*-axis of reference.

As we increase the diameter of the MTJ from 20 to 30 nm, the switching becomes non-coherent even for the lowest injected j_e. The change in the reversal mechanism can be understood considering that the system is larger than the single domain size, hence the formation of domains is more energetically favourable. This can be seen in the snapshots of the magnetic configuration in Figure 7.9(b) and Figure 7.9(d) for $j_e = 1 \times 10^{11}\,\mathrm{Am}^{-2}$ and $j_e = 5 \times 10^{11}\,\mathrm{Am}^{-2}$, respectively. When $j_e = 1 \times 10^{11}\,\mathrm{Am}^{-2}$ is injected, the system exhibits similar dynamic properties to the 20 nm MTJ and $j_e = 1 \times 10^{11}\,\mathrm{Am}^{-2}$. Interestingly, albeit the domain wall width remains nearly constant in the small disc, it exhibits breathing-like modes in the larger case and the reversal appears as quasi-coherent close to the switching of the magnetisation sign. The calculated excitation modes, presented in Figure 7.8(b), show that the coherent mode is the main excited mode. Although significant oscillations appear in the amplitude of m_0 around the switching of the magnetisation, m_0 remains the highest excited mode. This result is expected for coherent or quasi-coherent reversal and can be related to the variations in the domain wall width. Figure 7.11(b) presents the contour integral of the magnetisation. Here the reversed region originates at the edge of the system and the real and imaginary components of the contour integral oscillate, similarly to the 20 nm and $j_e = 1 \times 10^{11}\,\mathrm{Am}^{-2}$. We can conclude that for large diameters and low spin polarised current the reversal is driven by coherent mode of the magnetisation. Weak non-uniform excitations are also present and are responsible for an overall non-uniform switching, that is also favoured by the large in-plane size of the system. When we inject a higher current density $j_e = 5 \times 10^{11}\,\mathrm{Am}^{-2}$, the mode initially excited is the vortex mode m_1, as shown in Figure 7.8(d). This suggests a change in the nature of the reversal mechanism from coherent rotation of the magnetisation to edge nucleation of a domain that subsequently propagates thorough the system. The contour integral components for the external regions exhibit a lower oscillation frequency and larger amplitude compared to the previous cases. We attribute this feature to the change in the switching mechanism. Comparing the out-o-plane snapshots of the magnetisation, we find that the domain wall width is constant during the reversal and is thinner than for an injected current $j_e = 1 \times 10^{11}\,\mathrm{Am}^{-2}$. Moreover, the in-plane magnetisation exhibits a more complex dynamics, with formation of vortex-like spin structures during the reversal. Since larger diameters exhibit similar properties to the 30 nm system, we do not show them.

It is worth noting that the reversal mechanism in zero temperature differs markedly from the switching induced by the application of an external field. In Chapter 5 the reversal is centre nucleated for large enough diameters since the field is normal to the disc and the magnetostatic field is stronger at the centre. The in-plane component of the spin torque field aids non-uniformity at the edge of the system and can drive the generation of

a reversed region. For small diameters the reversal is coherent in both cases, although it is accompanied by rotation when the spin polarised current is applied.
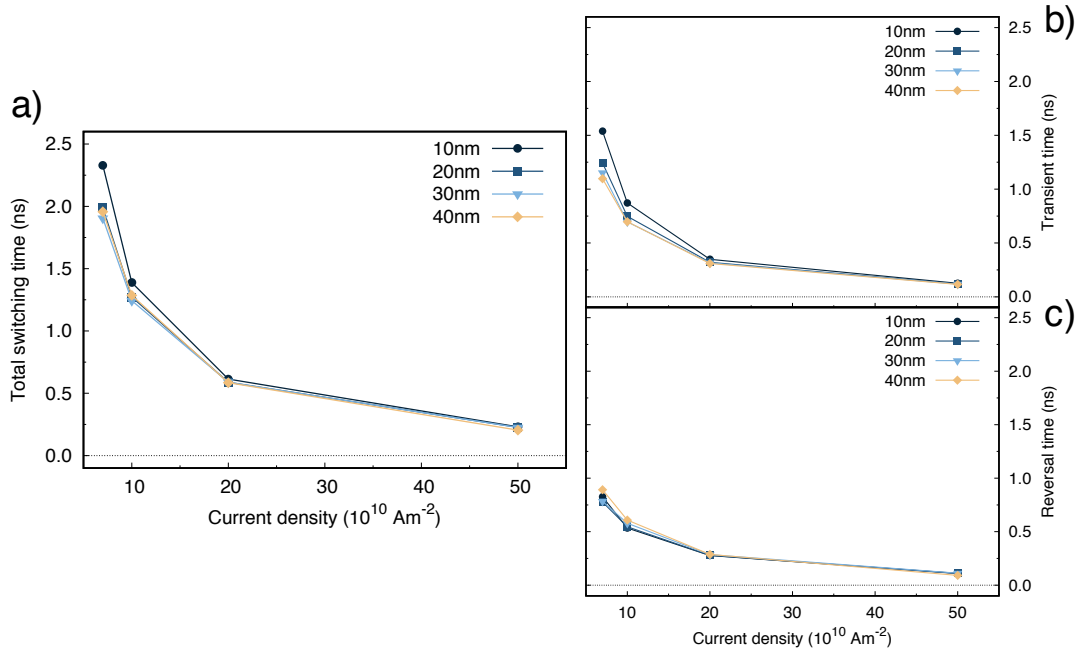
Figure 7.12 Plot of the total (a), transient (b), reversal (c) switching times of MTJ free layers for different diameters at $T = 0\,\text{K}$ as function of the injected current density. Transient and reversal time are defined in Section 7.2.3.

Fast switching times are desired for applications and devices with different switching speed are used to target different markets. Hence, we compute the switching time and we investigate its dependence on the current density j_e and on the diameter of the MTJ in order to characterise the CoFeB/MgO systems. Figure 7.12(a) shows the current density dependence of the total switching time for different diameters. We do not find large differences, except for a longer time required by the 10 nm stack for small j_e. To obtain a better understanding, we divide the switching time in transient and reversal time, as described in Section 7.2.3. The results are presented in Figure 7.12(b) and Figure 7.12(c) for the former and the latter, respectively. The transient time increases for small diameter as the system behaves as macrospin and is harder to reverse, as we have shown it occurs for the coercive field at low temperature in Chapter 5 [69]. The analogy can be understood since the coercivity is the field necessary to initiate the reversal of the magnetisation and the transient time represents the time required for the spin polarised current to drive the system out of equilibrium. The reversal time shows a weaker size dependence than the transient time with only a small increase for weak j_e for free layers with diameter 40 nm, which suggests that the time required to switch the magnetisation is not strongly dependent on the switching mechanism. Nonetheless, the increase of the reversal time

that we observe for the largest simulated diameter suggests that larger dimensions are accompanied by a more complex non-uniform dynamics of the magnetisation that could result in the deterioration of the switching properties. Even though the largest dimension we investigate are beyond the most recent technological requirements ($< 20\,$nm), this aspect needs to be accounted for when manufacturing a device. In fact, impurities and fabrication defects can aid the nucleation in the system and favour non-uniform reversal event at smaller dimensions.

7.3.2 Effect of temperature
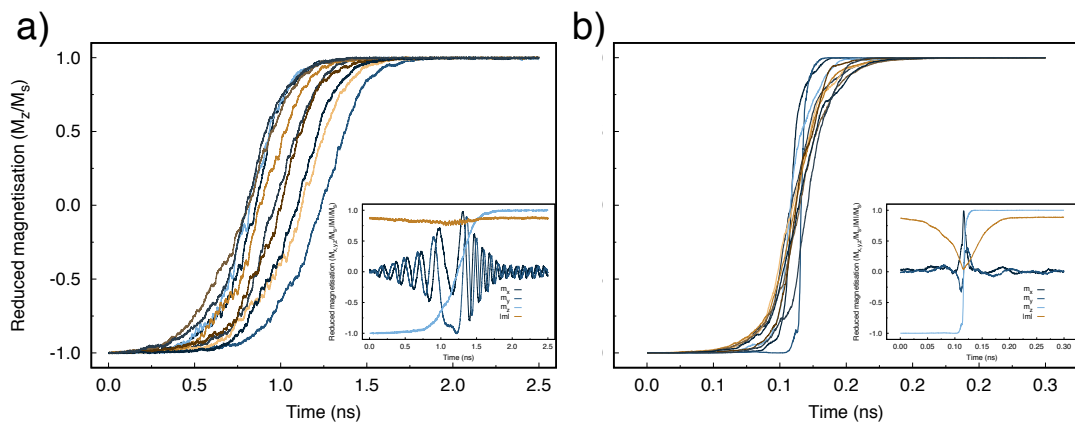
Figure 7.13 Plot of the reduced z-component of the magnetisation M_z/M_s of the free layer of CoFeB/MgO MTJs with diameter $30\,$nm obtained simulating ten independent switching events at $T = 300\,$K for an injected current $j_e = 7 \times 10^{10}\,$Am^{-2} (a) and $j_e = 5 \times 10^{11}\,$Am^{-2} (b). Different colours refer to different runs. The insets show the reduced components of the magnetisation for a specific switching event. Different blue shades represent the x, y and z-components of the magnetisation $M_{x,y,z}/M_s$, whereas the reduced magnetisation length $|\vec{M}|/M_s = |m|$ is presented in brown.

The analysis of the reversal mechanism induced by spin polarised currents developed so far neglects thermal effects. We expect that the random fluctuations might yield a stochastic character to the reversal, lead to faster switching due to thermal activation and might affect the nature of the magnetisation dynamics, similarly to the case of field induced magnetisation dynamics. We study the thermal effects at $T = 300\,$K. We simulate ten different switching events using a different pseudorandom number sequence that represents the random nature of the thermal noise to obtain a significant statistical average over the switching times, similarly to the method used in Chapter 5.

To illustrate the thermal effects on the switching properties, we plot the reduced z-component of the magnetisation M_z/M_s of the free layer of a $30\,$nm MTJ for $j_e =$

$7 \times 10^{10}\,\mathrm{Am^{-2}}$ and $j_e = 5 \times 10^{11}\,\mathrm{Am^{-2}}$ in Figure 7.13 (a) and Figure 7.13 (b), respectively. We observe that the distribution of magnetisation curves is larger for lower current densities and that the switching of the magnetisation does not exhibit significant differences for different runs, whereas M_z/M_s varies when $j_e = 5 \times 10^{11}\,\mathrm{Am^{-2}}$ is applied. The reversal becomes non-uniform for diameters larger than 10 nm even for the lowest j_e due to the thermal activation. In fact, thermal agitation promotes nucleation sites at the edge of the system favouring non-uniform processes. Interestingly, we find that the switching of the magnetisation is very sharp in some of the simulations with high j_e, as shown in the inset of Figure 7.13 (b). We do not observe rotation of the in-plane components of
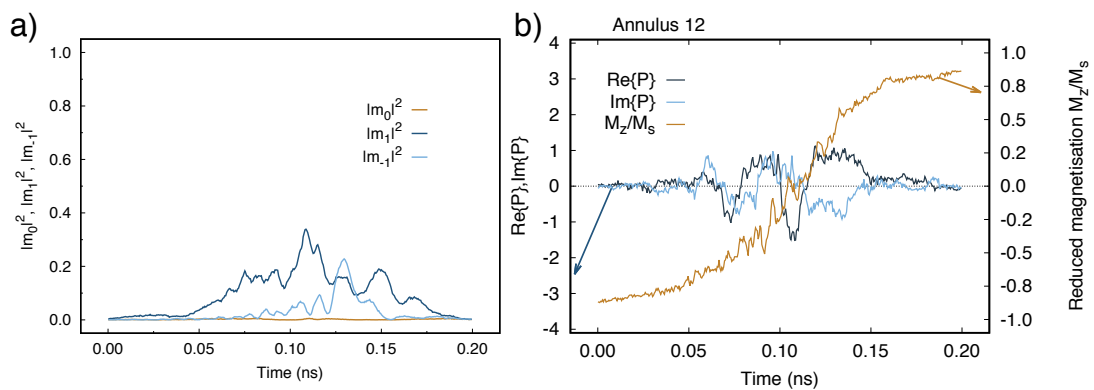
Figure 7.14 (a) Calculated amplitudes of the excitation modes (a) and components of the contour integral of the magnetisation for the most external annulus (b) of the free layers of 30 nm MTJs for $j_e = 5 \times 10^{11}\,\mathrm{Am^{-2}}$ at $T = 300\,\mathrm{K}$ whose magnetisation dynamics is presented in the inset of Figure 7.13(b). Arrows indicate the respective y-axis.

the magnetisation, a characteristic feature of spin torque dynamics observed so far. In addition, the free layer demagnetises across the switching. We compute the excitation modes associated to this switching event and the contour integral of the magnetisation, shown in Figure 7.14(a) and Figure 7.14(b), respectively. Surprisingly, we find that the coherent mode results suppressed totally and m_1 is the most strongly excited mode. Moreover, we do not observe the usual transition from vortex to antivortex mode, but rather a peak of the latter around the switching. Analysis of the snapshots of the magnetic configurations suggests the formation of multiple local metastable antivortex-like states. The analysis of the real and imaginary components does not show the usual oscillatory behaviour and we do not find large variations as function of radius. All these features confirm the complex nature of the reversal dynamics driven by the random nature of the thermal fluctuations and the need for a further understanding of the switching dynamics at finite temperature in these systems.

We now calculate the mean switching times and their distributions. We compare the size dependence of the transient and reversal times in Figure 7.15 (a) and Figure 7.15 (b),
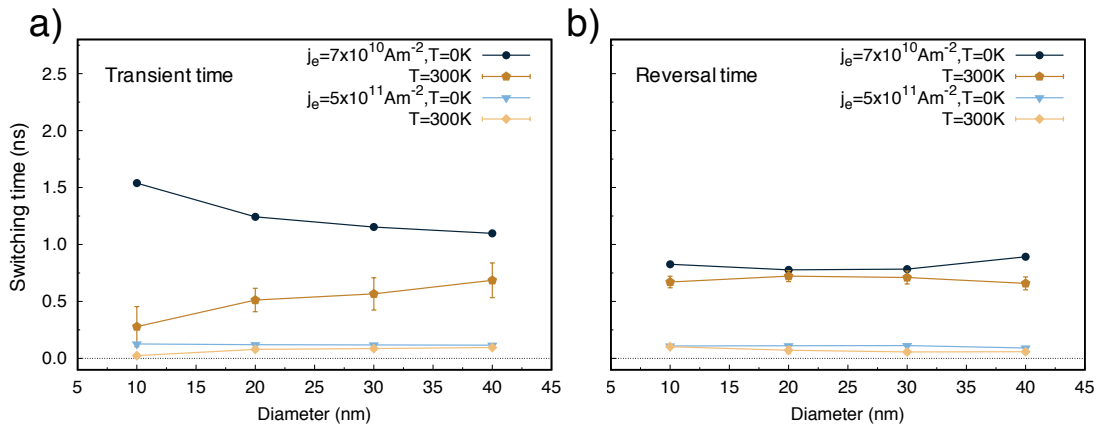
Figure 7.15 Plot of the calculated mean transient (a) and reversal (b) switching times of the free layer magnetisation induced by spin transfer torque dynamics as function of the system diameter for (a) $j_e = 7 \times 10^{10}\,\mathrm{Am}^{-2}$ and (b) $j_e = 5 \times 10^{11}\,\mathrm{Am}^{-2}$ at $T = 0\,\mathrm{K}$ (dark colours) and $T = 300\,\mathrm{K}$ (light colours). The error bars are the standard deviation of the switching times calculated over ten independent switching events.

respectively, for two different j_e values at zero temperature and $T = 300\,\mathrm{K}$. The reversal time is a characteristic of the system and we expect to depend on the injected current density. The extracted mean reversal times plotted in Figure 7.15 (b) are comparable at $T = 0\,\mathrm{K}$ and $T = 300\,\mathrm{K}$. This supports that the reversal time is an intrinsic property and is affected mainly by external factors, such as j_e. On the other hand, the transient time exhibits a stronger dependence on size and temperature. For small injected currents the average reversal time decreases when decreasing the diameter of the MTJ at $T = 300\,\mathrm{K}$. At finite temperature, small diameters become thermally unstable and the switching is triggered faster, in analogy with the coercive field dependence on the junction diameter at high temperature discussed in Chapter 5. As we inject higher current densities this effect persists, but it becomes less evident. Regarding the distribution of switching times, we find that the reversal time distribution is weakly dependent on the size and current density. The distribution is around $0.03\,\mathrm{T}$, a further confirmation of the intrinsic nature of the reversal time. The transient time is characterised by a larger distribution of the order of $0.1\,\mathrm{T}$ for small j_e, whereas the distribution approaches a value close to that of the reversal time for large current densities. The separation in reversal and transient components allows to distinguish the intrinsic time that the magnetisation requires to reverse from the time needed to initiate the switching. Consequently, this approach can be used to optimise the switching dynamics and engineer the stacks by focusing on the specific target.

7.3.3 Comparison with experiments

Time resolved spin transfer torque switching experiments have been performed on CoFeB/MgO-based MTJs. Devolder *et al.* [106, 107] measure switching events for different diameters and voltages. Devolder *et al.* infer that the reversal of the magnetisation occurs via domain wall generation and propagation through the system and the reversed region propagates linearly once it is nucleated at the edge of the disc. In similar studies, Hahn *et al.* [105] investigate the switching mechanism as function of diameter and current density. Hahn *et al.* find that the switching time is more sensitive to the lateral size of the stack at low current densities and that the switching is domain wall mediated, followed by linear propagation. Because of a more complex dynamics when switching from antiparallel to parallel configuration, Hahn *et al.* attribute the change to a different reversal mechanism. Our simulations agree with the results presented by Hahn *et al.* [105], showing a stronger dependence on the diameter of the MTJ when low current densities are injected. We also find that the reversal is non-uniform for similar dimensions, in agreement with Devolder *et al.* [106, 107] and Hahn *et al.* [105]. However, we stress that the simulations are characterised by a rotation of the reversed region in addition to the propagation. This has not been observed experimentally and it is worth noting that it is not feasible to access the real time dynamics at the nano- or subnano- time scales experimentally due to technological limitations. Hence, the atomistic modelling of the spin transfer torque, even though in its simplest form derived from the micromagnetic theory, is able to predict the switching dynamics and to shine some light on the reversal mechanism proving a useful model to interpret experimental results.

7.4 Conclusions

In the present chapter we have presented the main principles of the spin transfer torque phenomenon and discussed two approaches to model the spin transfer torque. Slonczewski's model is based on the transfer of angular momentum between the spin polarised current and the magnetisation in a trilayer stack where the ferromagnetic layers are treated within the macrospin approach and the parametrisation is empirical. The spin accumulation model is an improved approach based on the drift-diffusion theory that describes the spin transfer torque as the interaction between the local magnetisation and the spin accumulation, i.e. the local deviation of the spin density from equilibrium. Afterwards, we have described the formalism and how the calculation of the spin transfer torque are performed. We have also discussed useful methods that can provide a deeper understanding of the switching nature and dynamics, such as the analysis of the excitation modes, the computation of the contour integral of the magnetisation and the separation of

the switching time in transient time and reversal time. Finally, we have presented and analysed the results obtained for simulations of spin polarised induced switching.

The magnetisation reversal is driven by the combination of coherent and non-uniform excitation modes that, depending on the lateral size, temperature and injected current density, can be either non-uniform and initiated by a coherent mode of the magnetisation or domain wall nucleated. The dynamics of the magnetisation is accompanied by rotation in the plane components that persists even after the mean magnetisation of the system switches sign. Our results present comparable features to the experimental measurements of spin transfer torque switching in similar CoFeB/MgO-based magnetic tunnel junctions. Furthermore, the simulations suggest a more complex switching dynamics than assumed both experimentally and theoretically, and show the need for accurate modelling the spin torque phenomenon.

As final remark, we note that the systems object of study in this thesis are relatively simple structures. However, to study the spin torque and other similar effects at the atomistic level in systems where more complex magnetic structure, e.g. skyrmions, might occur would require a more accurate description of the spin torque, such as it is provided by the spin accumulation model.

Chapter 8

Multiscale atomistic simulations of the temperature dependent properties of Fe/MgO(001) ultrathin films

Due to technological requirements, spintronic devices are fabricated on a smaller and smaller scale. However, thin films differ from bulk systems due to surface, interface and relaxation effects that can affect the electronic and magnetic properties. In Fe/MgO-based MTJs the interaction between Fe and MgO planes results in complex finite-size effects and temperature dependent magnetic properties which must be carefully controlled for practical applications. For these reasons we investigate the magnetic properties of Fe/MgO thin films based on a multiscale approach, from *ab initio* to spin-dynamics. R. Cuadrado performed *ab initio* simulations of MgO/Fe/MgO thin films with different Fe thickness, calculating the relaxed structures necessary to obtain accurate magnetic parameters. R. Cuadrado and L. Szunyogh calculated the layer resolved magnetic moments, on-site anisotropy and exchange coupling using the relaxed system coordinates. A. Meo mapped the input *ab initio* data into an atomistic formalism suitable for VAMPIRE software package and used the input parameters to investigate the magnetic properties, ground state and thermodynamics, of MgO/Fe/MgO thin films.

In the first part a description of the model and of the parameters used in the spin simulations are discussed. Then, the ground state properties of MgO/Fe/MgO thin film are presented showing that thin films of Fe/MgO are characterised by complex ground-states with non-collinear magnetic surface structures. Such structures arise due to the complex exchange interactions with competition between antiferromagnetic in-plane interactions, Dzyaloshinskii-Moriya interaction and exchange anisotropy. Finally, the temperature dependence of the magnetisation and anisotropy are investigated, highlighting a non-monotonic behaviour of the temperature dependent anisotropy that depends strongly on

the exchange coupling. The results concerning the *ab initio* calculations and a brief investigation of the magnetic properties of Fe/MgO thin films are published in [60].

8.1 Introduction

When a system is reduced to few atomic layers, the magnetic properties deviate significantly from what is expected for bulk systems. In the case of MRAMs, the downscaling of the device size is an important factor and fabricating structures with thinner and thinner magnetic layers might results in affecting properties such as the energy barrier or the magnetoresitance. To achieve an understanding at the fundamental level, we investigate the complex magnetic properties of MgO(001)/Fe/MgO(001) thin films using a multiscale atomistic model parametrised *ab initio*, where the input parameters are calculated by means of the screened Korringa-Kohn-Rostoker (sKKR) Green's function method [19]. We perform atomistic spin simulations considering the full exchange coupling tensor containing long range interactions, layer resolved on-site magnetic anisotropies and magnetic moments. In the following, we present the modelling of such complex systems and we investigate how the magnetic properties, such as the magnetic ground state, magnetisation and anisotropy, of MgO(001)/Fe/MgO(001) ultra-thin films vary depending on the relaxation mechanism and on the thickness.

8.2 Methods

Ab initio parameters obtained using the fully relativistic sKKR Green's function method [19, 108] provide layer resolved magnetic moments (μ_s), localised anisotropy (k_u) and the full exchange coupling tensor ($\bar{\bar{J}}_{ij}$) with over 2000 interactions per spin. We focus on n_Fe-Fe/MgO multilayer structures, where $n_\mathrm{Fe} = 4, 8$ indicate the number of Fe layers considered. The atomic structure is a tetragonal distorted bcc lattice, whose relaxed coordinates and lattice parameters are calculated by *ab initio* simulation with the SIESTA package [109]. Since the electronic as well as the magnetic properties strongly depend on the crystal structure, obtaining the relaxed structure allows to better model these properties. An example is the change in the exchange coupling in manganese compounds from ferromagnetic to antiferromagnetic depending on the lattice spacing [24]. The detailed *ab initio* informations, described elsewhere [60], are used as input parameters within the atomistic spin framework to reach an accurate description of the magnetic properties of the system. A list of the layer resolved magnetic moments and on-site anisotropies for both $n_\mathrm{Fe} = 4$ and $n_\mathrm{Fe} = 8$ are shown in Table 8.1. We include these parameters in our spin model, described in section 2.5, and we study the magnetic

Table 8.1 Layer resolved parameters for MgO/n_{Fe}-Fe/MgO obtained from sKKR simulations [60] used as input parameters for the atomistic spin simulations.

MgO/8-Fe/MgO		
Layer	Atomic moment (μ_B)	On-site k_u (J)
1	2.783	3.283e-23
2	2.521	1.672e-23
3	2.328	2.832e-24
4	2.328	-2.991e-23
5	2.328	-2.991e-23
6	2.328	2.832e-24
7	2.521	1.672e-23
8	2.783	3.283e-23
MgO/4-Fe/MgO		
Layer	Atomic moment (μ_B)	On-site k_u (J)
1	2.693	1.227e-22
2	2.467	1.834e-23
3	2.467	1.834e-23
4	2.693	1.227e-22

properties of $10\,\text{nm} \times 10\,\text{nm} \times 8$ and 4 monolayer (ML) Fe/MgO thin films and their temperature dependence.

The dynamics of the magnetisation is obtained by integrating the LLG equation of motion (see Section 2.5.2). The ground-state magnetic configuration can be simulated performing zero field cooling simulations: the system is initialised at a temperature above T_c, around 1000 K, and afterwards the temperature is slowly reduced to 0 K. This method allows the system to relax towards the equilibrium configuration. The temperature dependence of the magnetic anisotropy is obtained using a constrained Monte Carlo (cMC) algorithm [87] in addition to the Monte Carlo (MC) method, which is applied to calculate the variation of magnetisation with temperature. The MC method used here is an extension of the more common Metropolis approach, where the trial move is a random displacement of the spin inside the unit sphere that includes all the possible spin arrangements. The employed algorithm combines the Metropolis move, which at very low temperature would lead to a high rejection rate since large variations in the spin direction have low probability, to other two types of trial moves: the spin flip and the Gaussian move. The former consists in reversing the spin direction of the selected atom, whereas the latter moves the direction of the spin in a cone whose width depends on the temperature. This favours small displacements from the initial position at low

temperature. At each step one of the three trial moves is picked randomly and the new energy is evaluated. This MC algorithm developed by Hinzke and Nowak provides a higher acceptance rate than Metropolis, resulting in a faster sampling of the accessible states [43]. The cMC algorithm is a MC method that acts on two spins at the same time [87]. It allows to constraint the direction of the magnetisation during the simulation along specific directions, whilst leaving individual spins to reach thermal equilibrium, as briefly discussed in Section 6.2.
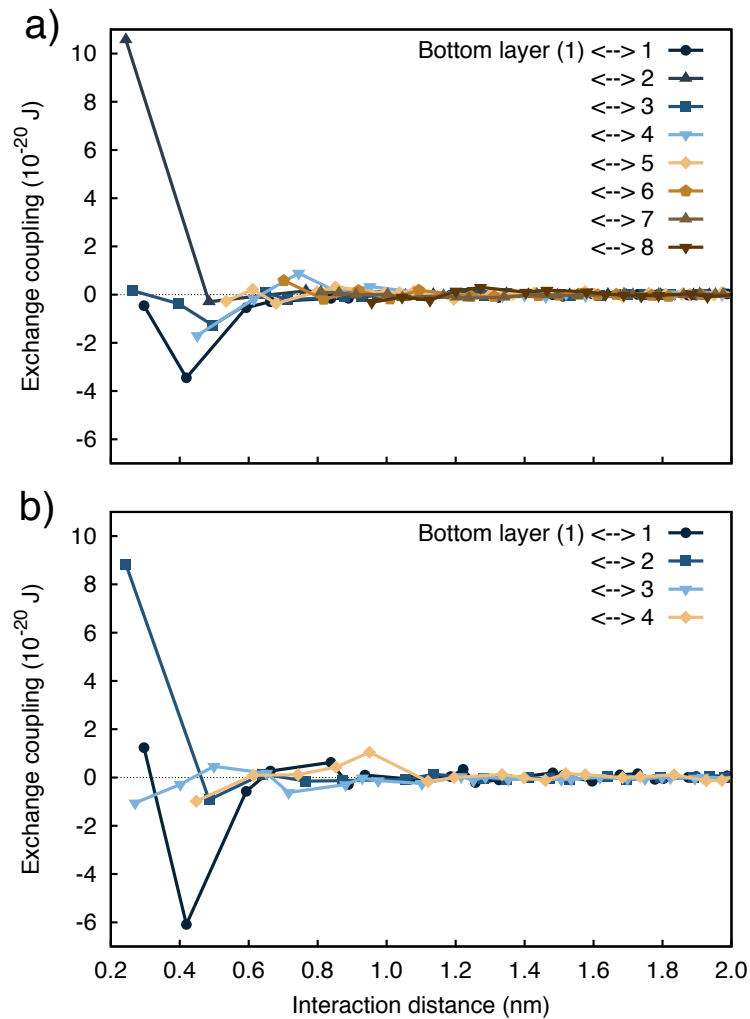

Figure 8.1 Fe-Fe isotropic magnetic exchange interactions as a function of the neighbor distances for an Fe atom located at the interface of the MgO/8-Fe/MgO (a) and MgO/4-Fe/MgO (b) system with the other Fe planes. Solid lines are guides for the eye.

8.3 Ground-state properties

A standard ferromagnet has a ground-state where all the spins align along the same direction. More complex exchange couplings might result in deviations from a uniform configuration, such as non-collinear magnetic structures, that can affect the temperature dependence of the magnetisation and anisotropy. We investigate the ground-state of Fe/MgO thin films using the *ab initio* input parameters [60] varying *a)* the interaction range and *b)* the exchange interaction type for both the system with 4 and 8 Fe layers. MgO causes strain in the Fe layers that yields compression of the lattice structure and hence a reduced out-of-plane lattice parameter. This tetragonal distortion induces a competition between ferromagnetic and antiferromagnetic interactions at the interface between Fe and MgO which results in different interactions between neighbouring Fe planes. We find strong in-plane antiferromagnetic interactions for the first few shells of neighbours in the interfacial Fe layers, as shown in Figure 8.1(a) and Figure 8.1(b). *Ab initio* calculations provide an exchange coupling which includes non-negligible Dzyaloshinskii-Moriya interaction (DMI) [31, 30] in the Fe layers in contact with MgO. As discussed in
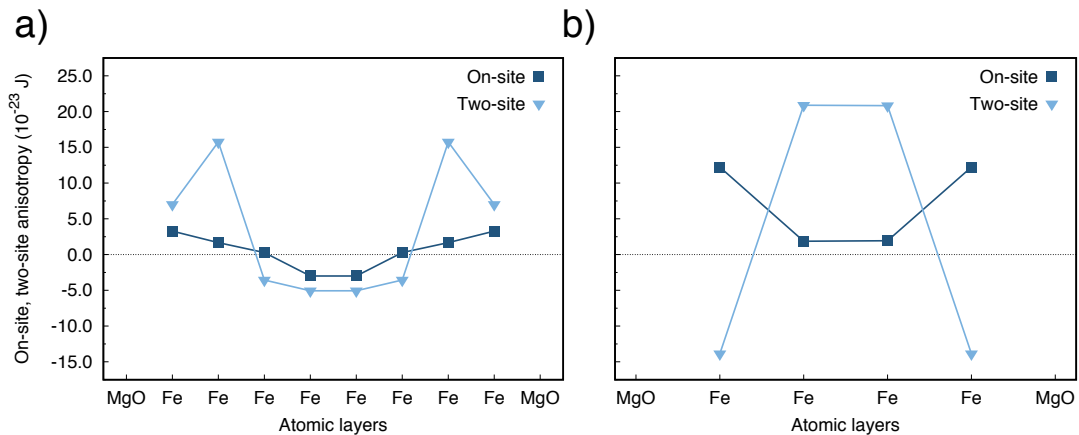
Figure 8.2 (a) On-site and (b) two-site magnetic anisotropy contributions for MgO/n_{Fe}–Fe/MgO ($n_{Fe} = 4$, 8) systems, where positive and negative values represent out-of-plane and in-plane anisotropy, respectively. In both $n_{Fe} = 4$ and $n_{Fe} = 8$ the two-site contribution is larger in magnitude than the on-site anisotropy. Lines are guide for the eye. The data is kindly provided by R. Cuadrado [60].

the method chapter, DMI arises due to breaking of symmetry and therefore is localised at the interfaces. The interactions between adjacent Fe planes are ferromagnetic and are the strongest coupling experienced by the interface layers, for both the considered thicknesses. We find that the polarisation of the magnetisation of the central layers depends on the Fe thickness: the magnetisation lies out-of-plane for $n_{Fe} = 8$ and in-plane for $n_{Fe} = 4$. This different orientation of the magnetisation is caused by the two-sites anisotropy [60],

an exchange anisotropy, whose magnitude is comparable with the on-site anisotropy, as shown in Figure 8.2. Despite this, the central layers are ferromagnetically coupled between each other in both systems. Such complex interactions lead to non-collinear spin surface configurations, i.e. non-collinear magnetic structures, at low temperature. These results agree with Yavorsky and Mertig [110], who perform *ab initio* calculations in Fe/FeO/MgO/Fe tunnel junctions and infer that non-collinear structures are likely to form.
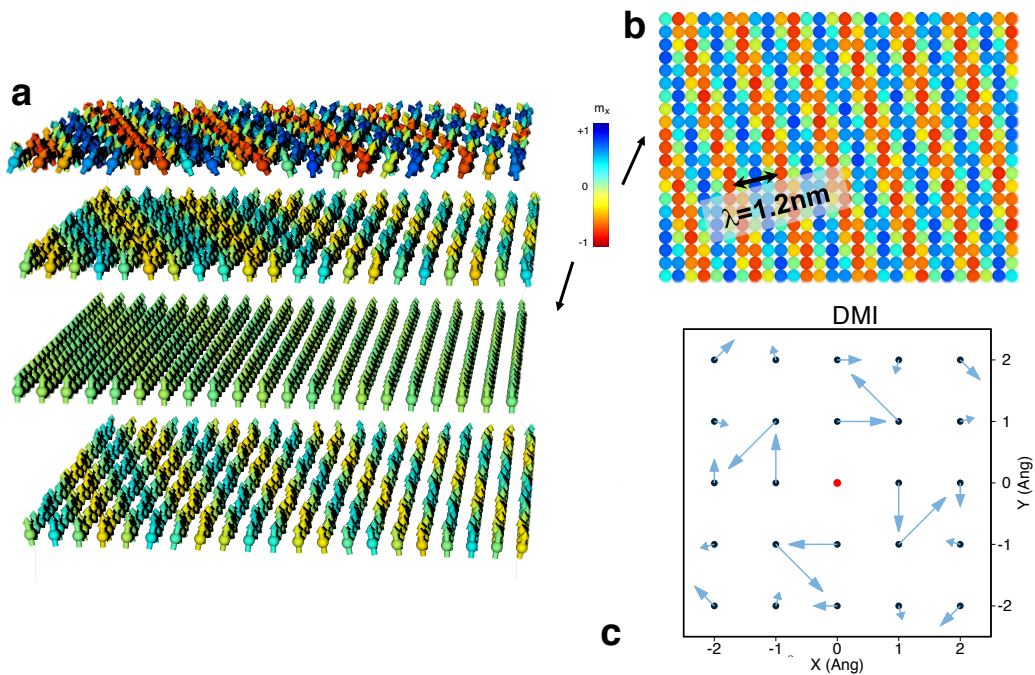
Figure 8.3 Perspective (a) and top (b) view of the simulated ground-state spin structure at the n_{Fe}-Fe/MgO interface for $n_{Fe} = 8$, leading to a near ferromagnetic state in the centre of the sandwich. The colouring indicates the x component of the magnetisation (blue for $+x$, red for $-x$, and green for $x = 0$). The atomic moments form a non-collinear configuration with wavelength $\lambda = 1.2$ nm and angle between spins no larger than $45°$ in the perpendicular direction. (c) Plot of Dzyaloshinsky-Moriya interaction (DMI) between an atom (red dot) located at the top layer and the neighbouring atoms (black dots) in the same layer. The magnitude of DMI is given by the arrow length. We note that DMI is in the x–y plane solely.

8.3.1 MgO/8-Fe/MgO

A visualization of the final magnetic ground-states for $n_{Fe} = 8$ is presented in Figure 8.3(a) and Figure 8.3(b). In Figure 8.3(a) the top plane represents Fe at the MgO interface. A spin-spiral ground-state appears due to the frustration between ferromagnetic and antiferromagnetic interactions and DMI at the interface caused by broken inversion

symmetry. Interestingly, the orientation of the spiral is at approximately 16.4° to the *x*-axis and the spin-spiral is confined to positive *z* values. Moving along the layers towards the centre of the stack, the spin-spiral becomes much less prominent and a ferromagnetic ordering dominates. This confirms that the interfacial antiferromagnetic nearest-neighbour interactions and DMI are responsible for the frustrated spin-spiral structure. In fact, such a complex exchange pattern arises only in those layers that are at the interface with MgO. Figure 8.3(c) shows the top view of DMI vectors and their magnitude for the top layer. The vectors lie in the *x-y* plane and we can see a non-trivial relationship among the neighbours and the magnitude of DMI. Figure 8.4 presents snapshots of the magnetic
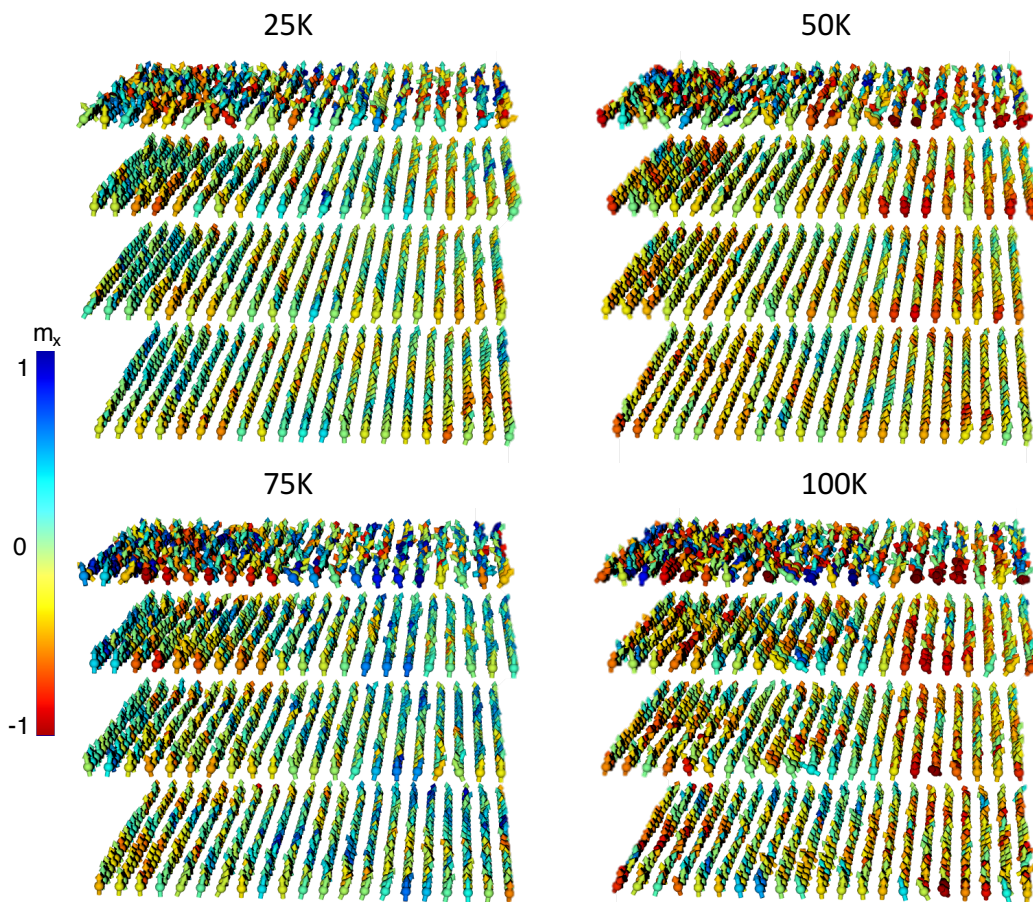
Figure 8.4 Snapshots of the spin configuration showing the temperature evolution of the spin-spiral for the first 4 layers of the $n_{Fe} = 8$ system. The non-collinear character starts fading as the thermal contribution increases and is lost at $T = 50$ K. The colour scheme describes the *x* component of the magnetisation (blue for $+x$, red for $-x$, and green for $x = 0$).

configurations for the top four layers of the $n_{Fe} = 8$ system at different temperatures. A distinct magnetic ordering between the top interfacial layer and the other Fe layers can be observed at 25 K, even though spin fluctuations caused by the thermal agitation are found.

Snapshots obtained at higher temperature show the loss of the non-collinear feature and a more uniform layer behaviour emerges. This re-orientation of the spin structure is visible in the temperature dependence of the magnetisation and effective anisotropy, and it will be discussed in Section 8.4.
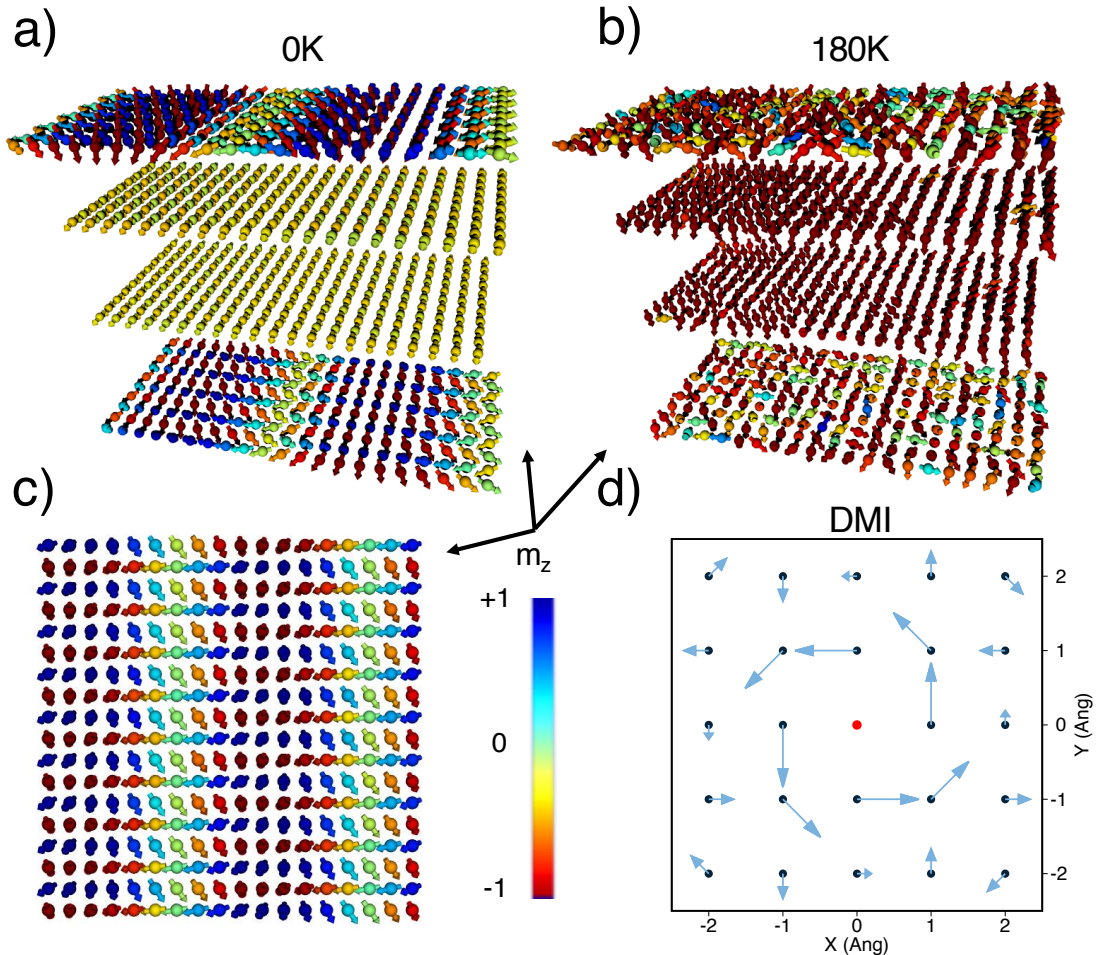
Figure 8.5 Snapshots of the spin configuration showing the temperature evolution of the spin-spiral for the $n_{Fe} = 4$ system from $T = 0\,K$ (a) and (c) perspective and top view, respectively, to $T = 180\,K$ (b). The non-collinear character seen at $0\,K$ is lost at temperatures larger than $T = 180\,K$. The colour scheme describes the z component of the magnetisation (blue for $+z$, red for $-z$, and green for $z = 0$). (d) Plot of Dzyaloshinsky-Moriya interaction (DMI) between an atom (red dot) located at the bottom layer and the neighbouring atoms (black dots) in the same layer. The magnitude of DMI is given by the arrow length. We note that DMI is in the x–y plane solely.

8.3.2   MgO/4-Fe/MgO

Figure 8.5(a) and Figure 8.5(c) present the perspective and top view of the simulated ground-state at $T = 0\,\mathrm{K}$ for $n_{\mathrm{Fe}} = 4$ system, respectively. While in the ground-state the spins at the Fe/MgO are canted with respect to the perpendicular direction (z–axis) with an angle around $16.4°$ and the layers keep a strong out-of-plane magnetisation in the $n_{\mathrm{Fe}} = 8$ system, the magnetic configuration of the interfacial layers is a spin-spiral state with the spins undergoing a full $180°$ rotation for $n_{\mathrm{Fe}} = 4$. The competition between the strong intra-layer antiferrormagnetic coupling, which induces canting and non-collinear structures, and DMI in the interfacial layers are responsible for the full spin-spiral state. A plot of DMI for $n_{\mathrm{Fe}} = 4$ is presented in Figure 8.5(d). DMI arises only at the Fe/MgO interface and lies in the x-y plane, as discussed for $n_{\mathrm{Fe}} = 8$. Here the strength of the interaction decreases with distance. Moreover, the interactions within a few neighbouring shells are arranged in a vortex-like fashion contributing to the formation of the spin-spiral. Looking at the properties of the layers away from the interface, one can see that the central layers are magnetised in-plane, differently from what happens for the thicker sandwich where the magnetisation of the inner layers is oriented out-of-plane. The lattice distortion caused by the MgO is stronger in the $n_{\mathrm{Fe}} = 4$ system and is responsible for the in-plane orientation of the magnetisation. The central layers in the Fe system with $n_{\mathrm{Fe}} = 8$ preserve a bulk-like character instead. Figure 8.5(b) presents the snapshot of the magnetic configuration for the $n_{\mathrm{Fe}} = 4$ system at $180\,\mathrm{K}$. The non-collinear character is lost at about $180\,\mathrm{K}$ and an overall ferromagnetic ordering is recovered. Interestingly, this transition in the magnetic configuration of the interfacial layers corresponds to the re-orientation of the magnetisation of the two central layers from in-plane to out-of-plane. These complex interactions will affects the temperature dependence of the magnetisation and anisotropy, similarly to the case of $n_{\mathrm{Fe}} = 8$, and will be the subject of later discussion.

8.3.3   Ground-state dependence on exchange coupling

In order to study the effect of the exchange coupling on the magnetic properties of the Fe systems, we adapt the exchange interaction matrix considering the following cases: a) (isotropic) only the trace of $\bar{\bar{J}}_{ij}$ for an isotropic approximation, b) (vectorial) the three diagonal components J_{ij}^{xx}, J_{ij}^{yy}, J_{ij}^{zz} to include the exchange anisotropy contribution and c) (tensorial) the whole $\bar{\bar{J}}_{ij}$ tensor to study the general case. For $n_{\mathrm{Fe}} = 4$ the ground-state has a non-collinear character in all the three cases we investigated, as shown in Figure 8.5 for tensorial and Figure 8.6 for isotropic and vectorial approximations. The magnetic configuration obtained for a full exchange tensor is a spin-spiral state where the spin directions vary by $180°$ from positive to negative z-axis in the interface layers and the central two layer re-orient in-plane. In contrast, if we approximate the exchange
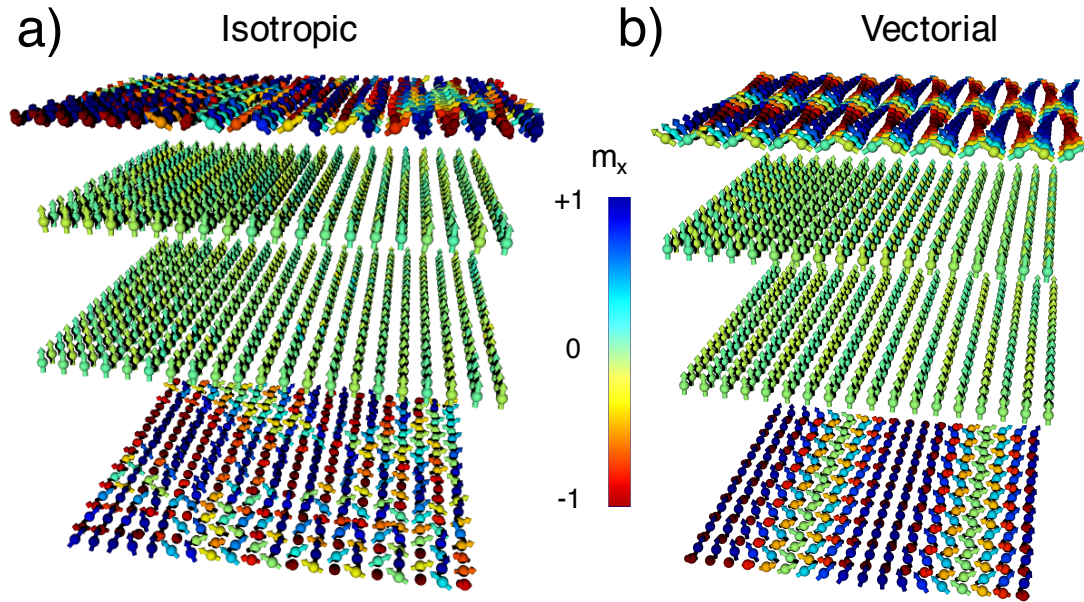
Figure 8.6 Perspective view of the simulated ground state for $n_{Fe} = 4$ for an isotropic (a) and vectorial (b) approximation of the exchange coupling tensor $\bar{\bar{J}}_{ij}$. The colouring indicates the x component of the magnetisation (blue for $+x$, red for $-x$, and green for $x = 0$).

coupling, spin canting occurs only at the interface with MgO. This suggests that the canting is driven by the antiferromagnetic in-plane interactions and appropriate DMI, in strength and direction, is required to achieve a spin-spiral state. For $n_{Fe} = 8$ the magnetic ground-state is characterised by spin canting in the interfacial layers. In this case, different approximations for the exchange coupling do not cause significant changes in the magnetic texture. The difference between $n_{Fe} = 4$ and $n_{Fe} = 8$ is likely to be attributed to the stronger bulk character of the thicker system.

8.4 Temperature dependent magnetic properties

We investigate the effect of complex atomic resolved properties, in particular the exchange coupling and reduced dimensionality, on the temperature dependence of the macroscopic magnetic properties.

8.4.1 Magnetisation

The presence of interfaces and the fact that the system is composed of few atomic layers cause a decrease in the coordination number and exchange links. These result in larger random thermal fluctuations of the spins, particularly at the interfacial layers. From the

mean-field Heisenberg model, as discussed in Section 4.2, $J_{ij} = 3k_B T_c / (\varepsilon z)$ [43] and hence one expects a reduction of T_c when passing from a bulk system to a thin film. We
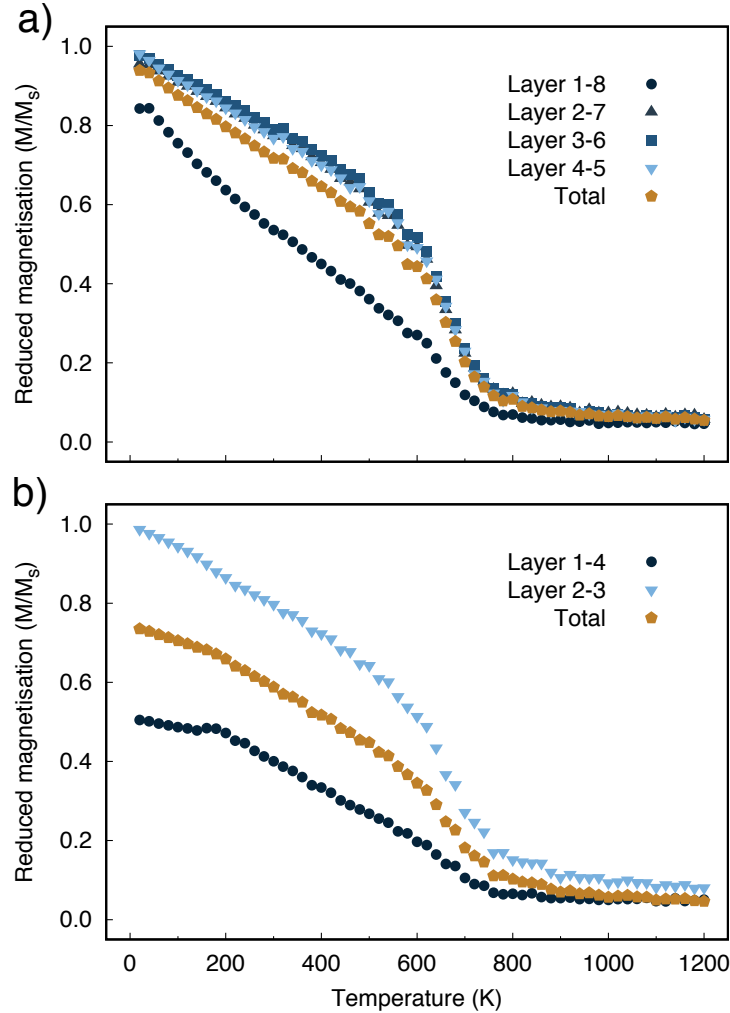
Figure 8.7 Simulated layer resolved temperature dependent reduced magnetisation (M/M_s) for $n_{Fe} = 8$ (a) and $n_{Fe} = 4$ (b) systems. The light brown diamonds describe the resulting magnetisation length of the whole system, while different shades of blue represent the individual layer magnetisation. The Fe/MgO interface shows reduced low temperature ordering, more evident for $n_{Fe} = 4$, due to the spin-spiral state and a stronger temperature dependence of the magnetisation due to the frustration in the spin system and the presence of DMI. A transition temperature below which the magnetisation is almost constant at around 50 K and 200 K can be seen for the $n_{Fe} = 8$ and $n_{Fe} = 4$ systems, respectively. The simulations are performed by first equilibrating the system for 10,000 Monte Carlo steps at each temperature, and then the average of the magnetisation is calculated over 50,000 steps.

simulate the temperature dependence of the magnetisation and we find that the Curie temperature (T_c) decreases in comparison with bulk bcc Fe, for which $T_c \sim 1043$ K [47].

The simulations are performed by first equilibrating the system for 10,000 Monte Carlo steps at each temperature and then the average of the magnetisation is calculated over 50,000 steps. This reduction of T_c can be also related to the distortion of the Fe lattice and the frustration of the spin structure induced by the MgO. Ležaić *et al.* [47] find that the exchange energies in Co, Fe and CoFe alloys are affected by the deformation of the lattice structure as this introduces stretching or compression of interatomic distances, causing variations in the electronic properties such as the exchange coupling. Since the distance between Fe planes is compressed and the in-plane distance between atoms increases during the relaxation process, a decrease in the exchange coupling and a lower T_c than in an unrelaxed bcc face occur. Figure 8.7(a) and Figure 8.7(b) show the simulated temperature dependent reduced magnetisation length (M/M_s) for the $n_{Fe} = 8$ and $n_{Fe} = 4$ systems, respectively. We find that the interfacial layers (black dots) are characterised by a different dependence on the temperature with respect to the other planes. The former show a reduced criticality and lower T_c, due to the reduced number of exchange links, the presence of DMI and frustration of the spin system. Moreover, the interfacial layers exhibit two distinct trends at low temperature up to 50 K and 200 K for $n_{Fe} = 8$ and $n_{Fe} = 4$ systems, respectively. At low temperature both systems are characterised by non-collinear magnetic states at the interface, with the spins that are canted rather than aligning along the same direction, as it would occur in a bulk Fe system. This effect is clear in Figure 8.7(a) and Figure 8.7(b), where we can observe the initial plateau of the magnetisation followed by a decreasing trend. We observe that for $n_{Fe} = 4$ the system has a reduced magnetisation due to the appearance of a full spin-spiral in the ground state, as shown above. DMI presents a strong temperature dependence, which results in a flat temperature dependence initially. When the thermal energy becomes comparable with the contribution of DMI, a transition from the non-collinear state towards a more uniformly magnetised configuration occurs. Despite this, the criticality of the temperature dependence of the magnetisation of the interface differs from that the rest of the other layers, with a trend typical of surfaces.

To test the effect of the long exchange interaction range on the magnetisation and its temperature dependence, we first perform simulations considering a nearest-neighbour approximation of $\bar{\bar{J}}_{ij}$. We retain the tensorial form of the exchange coupling and, interestingly, we find that the system behaves as a slab of unrelaxed bcc Fe of the same thickness and with isotropic exchange approximation. The temperature dependence of the magnetisation for $n_{Fe} = 8$ is presented in Figure 8.8(a). All layers exhibit a similar temperature dependent magnetisation, with a criticality closer to that expected in systems characterised by Heisenberg exchange. Furthermore, the layers close to the interface do not show non-collinear magnetic configurations at low temperature. To further understand the effect of the exchange range, we increase the shells of nearest-neighbours considered
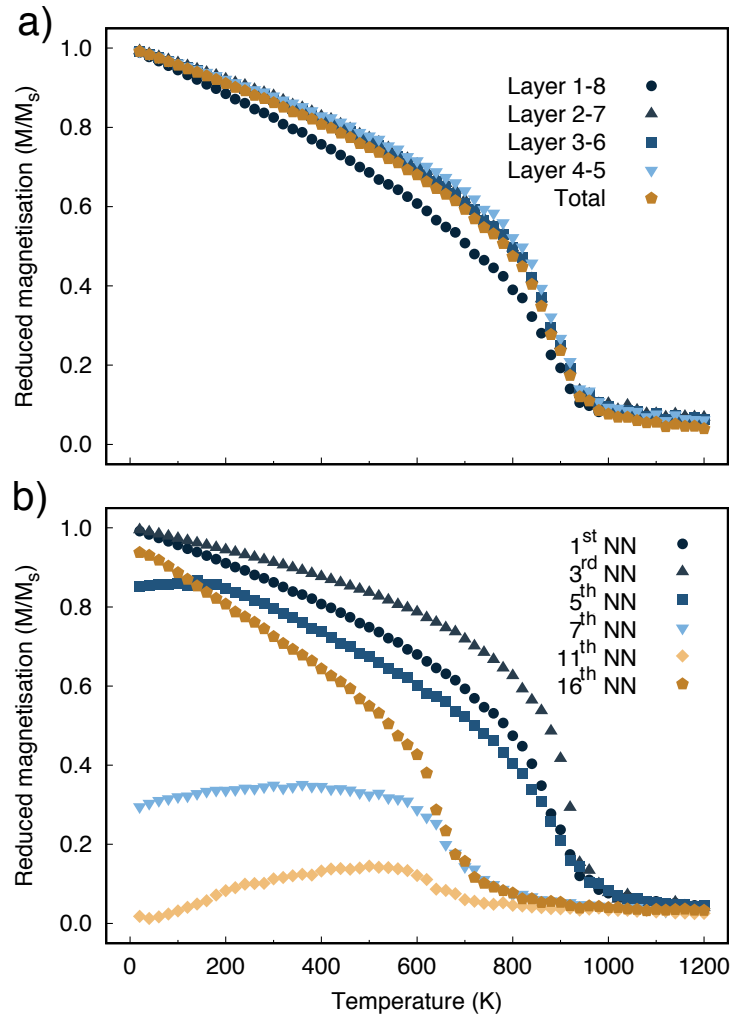
Figure 8.8 (a) Simulated layer resolved temperature dependence of the reduced magnetisation (M/M_s) for MgO/8-Fe/MgO for a nearest-neighbours approximation of the exchange coupling. (b) Simulated temperature dependent reduced total magnetisation for $n_{Fe} = 8$ systems for different interaction ranges. Increasing the interaction range from a few neighbours to the totality of the interactions yields a reduction of the Curie temperature and a loss of ordering at low temperature.

in the exchange tensor. We present the total magnetisation of the system for different shells of nearest-neighbours in Figure 8.8(b). Surprisingly, the trend of the magnetisation is strongly affected by the interaction range of the exchange coupling. The interaction range affects T_c, the criticality and the magnetic ordering at low temperature. As more and more interactions are included, the in-plane antiferromagnetic coupling in the interface layers becomes the dominant contribution and aids the formation of non-collinear magnetic states. Non-collinear structures are responsible for low magnetised states at low temperature. Such a reduction continues until almost the complete loss of magnetisation occurs for simulations that include up to the eleventh nearest-neighbouring shell. If

more neighbours are taken into account, we observe a partial recovery of the magnetic ordering. The system with $n_{Fe} = 4$ exhibits analogous features when varying the range of the exchange coupling. We can conclude that the long range exchange coupling induced by the presence of MgO and by the relaxation process is a main factor in causing the reduction of T_c, the formation of non-collinear spin states in the interfacial layers and a stronger temperature dependence of the magnetisation than in a simple Fe thin films.

8.4.2 Anisotropy

We also investigate the magnetic anisotropy energy (MAE) and its temperature dependence. We perform simulations with the cMC algorithm constraining the direction of the magnetisation away from the easy axis, the direction orthogonal to the Fe planes, from $\vartheta = 0$ to $\vartheta = 180°$. Assuming a uniaxial anisotropy, the anisotropy energy can be expressed as $E(\vartheta) = K_{eff} \sin^2(\vartheta)$, where K_{eff} is the effective anisotropy energy constant. Since the torque is given by $T(\vartheta) = -\partial E(\vartheta)/\partial \vartheta$, it is proportional to $K_{eff} \sin(2\vartheta)$. Fitting the torque using this relation allows to extract K_{eff} as a fit parameter. A more general approach is to derive K_{eff} using a quadrature method [87] integrating the torque over the angle distribution and extracting K_{eff} from the area of the curve. This technique has the advantage that does not require to predict the properties of the system. We choose to adopt the latter, given the complexity of the magnetic properties of our system with layer resolved anisotropy parameters other than a long range tensorial exchange coupling and strong interfacial effects. In the cMC method a calculation per constraining angle is performed and this results in a long run time. In addition, our system is characterised by a large number of interactions per spin, about 2000. As the computational cost of the simulations increase with the number of interactions per spin, we decide to investigate K_{eff} and its temperature dependence focusing on the effect of different exchange coupling approximations, whereas we keep the interaction range constant. The simulations are performed by first equilibrating the system for 10,000 Monte Carlo steps at each temperature, afterwards the average of the restoring torque and magnetisation is calculated over 50,000 steps.

MgO/8-Fe/MgO

We calculate the torque acting on the magnetisation for different constraint angles at different temperatures. Figure 8.9 presents the angular dependence of the torque for different temperatures for the $n_{Fe} = 8$ system obtained performing simulations with the full exchange tensor. After an initial increase from 20 K to 40 K, the torque decreases with increasing temperature, as expected for a standard ferromagnet. The change in the trend corresponds to the transition in the magnetic state from a canted magnetic configuration
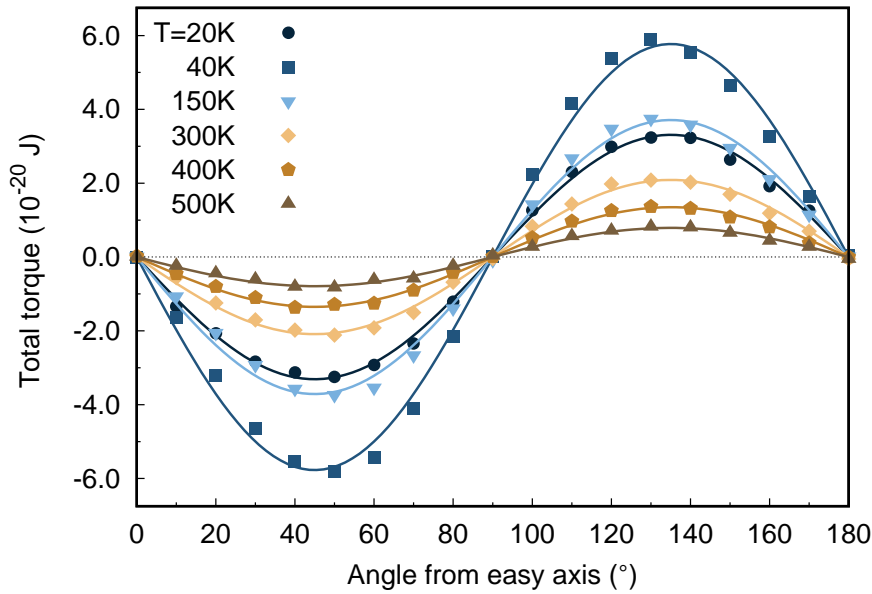
Figure 8.9 Simulated restoring torque in a MgO/8-Fe/MgO thin film. The solid lines are $\sin(2\vartheta)$ fits of the data in the range $[0° : 36°]$.

to a ferromagnetically ordered structure and change in the trend of the magnetisation temperature dependence. We fit the torque curves with the $\sin(2\vartheta)$ expression expected for uniaxial anisotropy, shown by the solid lines in Figure 8.9. The agreement between the data and the analytic model is not perfect and can be understood taking into account the complexity of the anisotropy. In fact, the system is characterised by in-plane bulk-like anisotropy, strong out-of-plane anisotropy, two-sites anisotropy contribution and DMI. To discern the different contributions, we calculate the total restoring torque acting on the magnetisation approximating the exchange coupling. We consider the vectorial approximation to account for the anisotropy in the exchange coupling in the absence of DMI and the isotropic form of the exchange. Reducing the exchange coupling to the diagonal components J_{ij}^{xx}, J_{ij}^{yy}, J_{ij}^{zz} does not affect the initial increase of the torque with temperature up to $T = 40\,\text{K}$, as shown in Figure 8.10(b). Differently from the full exchange coupling case, we note that the system torque exhibits the $\sin(2\vartheta)$ characteristic of uniaxial anisotropy after the transition temperature with the vectorial approximation. Similarly, considering an isotropic approximation of the exchange coupling, presented in Figure 8.10(a), results in the torque displaying the behaviour expected for a uniaxial system. The fact that the uniaxial character is recovered for simulations performed with approximated forms of the exchange suggests that frustration and DMI at the Fe/MgO interfaces induce deviations from such a trend. Instead, the long range of the exchange coupling and the competition between ferromagnetic and antiferromagnetic interactions is responsible for the non-monotonic dependence of the torque with the temperature.
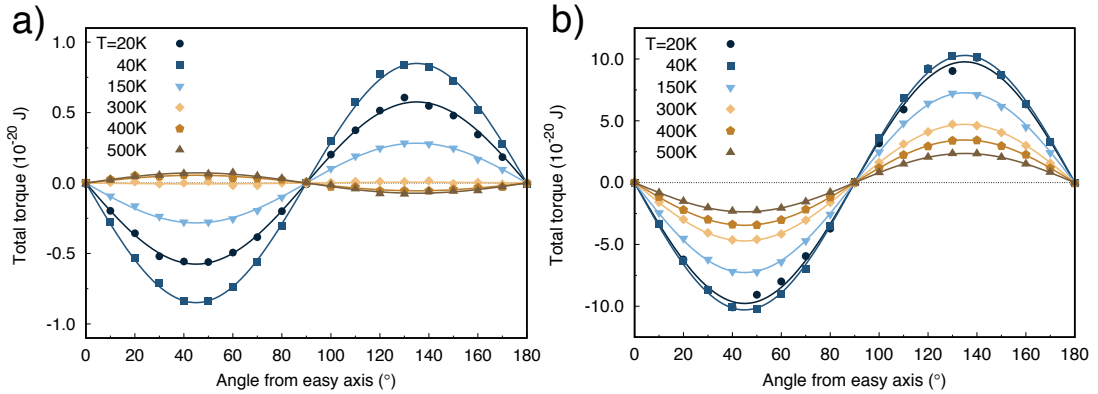
Figure 8.10 Simulated restoring torque in a MgO/8-Fe/MgO thin film for an isotropic (a) and vectorial (b) approximation of the exchange coupling. The solid lines are $\sin(2\vartheta)$ fits of the data in the range $[0° : 36°]$.

Interestingly, we find that the system undergoes a re-orientation from out-of-plane to in-plane magnetisation in the isotropic case as the temperature is increased more than $T = 300\,\text{K}$. This is evident from the change in the sign of the restoring torque in Figure 8.10(a). This temperature-dependent re-orientation occurs in thin films when there is competition between bulk and surface anisotropies [87]. At low temperature the magnetisation lies along the easy direction of the surface, which is perpendicular to the plane for our system. As the temperature is increased, the surface contribution to the total anisotropy energy of the system decreases and the magnetisation lies along the bulk easy axis, which is oriented in the plane [60].

We present in Figure 8.11 the extracted temperature dependences of the effective anisotropy $K_{\text{eff}}(T)$ for $n_{\text{Fe}} = 8$, where different colours represent a different exchange approximation. All the values of $K_{\text{eff}}(T)$ are normalised to the sum of the on-site and two-sites anisotropies at $T = 0\,\text{K}$ ($K_{\text{u}}(0\,\text{K})$), obtained from the sKKR calculations [60]. $K_{\text{eff}}(T)$ shows a non-monotonic behaviour at low temperatures caused by the non-collinear magnetic state. This feature does not depend on the type of exchange, since we observe it for all the exchange approximations. As the spin agitation induced by the temperature increases, the spin-spiral ground state weakens leading to an increase in the $K_{\text{eff}}(T)$ and a ferromagnetic-like ordering in the interface layers is recovered. Moreover, $K_{\text{eff}}(T)$ exhibits a re-orientation from out-of-plane to in-plane for an isotropic exchange, as already observed with the torque.

We extract the scaling exponents of the anisotropy with the magnetisation as function of temperature. Interestingly, the scaling $K_{\text{eff}}(T)$ is characterised by an exponent of 4.1, shown in Figure 8.12. This value differs from what is expected for either single-ion or two-ion anisotropy [27, 87], 3 and 2 respectively. We exclude from the analysis the data
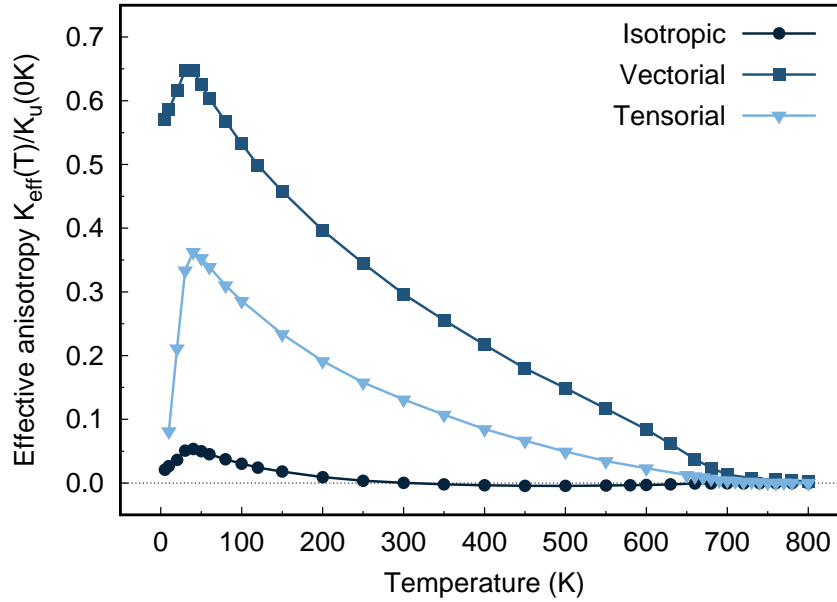
Figure 8.11 Plot of the temperature dependence of the effective anisotropy (K_{eff}) as function of temperature (T) for the n-Fe/MgO system with $n_{\text{Fe}} = 8$. Different colours correspond to simulations performed using different exchange approximations: black dots for isotropic exchange, blue squares for the vectorial approximation and light blue downward triangles for the whole $\bar{\bar{J}}_{ij}$ tensor. All the values of $K_{\text{eff}}(T)$ are normalised to the sum of the on-site and two-sites anisotropies at $T = 0\,\text{K}$, $K_{\text{u}}(0\,\text{K}) = 3.53 \times 10^6\,\text{Jm}^{-3}$, obtained from the sKKR calculations [60]. Lines serve as guide for the eye.

at temperatures lower than $T = 50\,\text{K}$, the temperature at which the system recovers a decreasing behaviour. We attribute this scaling exponent value to the frustrated nature of the exchange interactions and to the presence of DMI at the Fe/MgO interfaces. We suggest that DMI and frustration cause a high scaling exponent, such as the appearance of a cubic-like component in the anisotropy. The layers away from the interface present a bulk-like character with comparable uniaxial and two-ion anisotropy that would result in a scaling exponent between 2 and 3. Consequently, when we take the average anisotropy and magnetisation and we extract the scaling with temperature, we obtain a higher exponent. In addition, DMI can be seen as a higher order anisotropy and, as such, it could affect temperature dependence of $K_{\text{eff}}(T)$.

A distinct feature we observe is the strong dependence of $K_{\text{eff}}(T)$ on the exchange coupling. Although a definitive explanation is to be found yet, it is reasonable to assume that the largest $K_{\text{eff}}(T)$ is found for the vectorial case due to the strong two-ions anisotropy contribution. In fact, this contribution dominates over the uniaxial on-site anisotropy yielding a larger $K_{\text{eff}}(T)$ than in the isotropic case. When the whole tensor is considered, DMI acts as an additional source of anisotropy [111]. DMI competes with the on-site and two-sites anisotropies resulting in a $K_{\text{eff}}(T)$ that has a value that lies in between. The
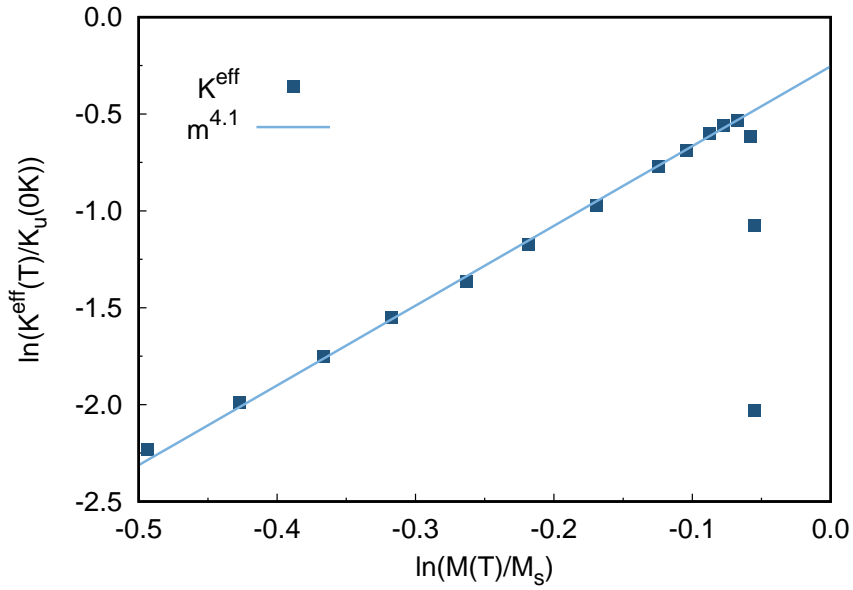
Figure 8.12 Scaling of the effective anisotropy with the total magnetisation for $n_{Fe} = 8$ systems. The symbols represent the data and the solid line the $K_{eff}(T)/K_u(0\,K) = m^a$ fit in the range $[50\,K : 400\,K]$ where m is the reduced magnetisation $M(T)/M_s$ and $a = 4.1$ is obtained from the fit.

analysis of the magnetic properties as function of the exchange coupling implies that it is not possible to approximate such complex exchange interactions using a simpler effective form. Consequently, the whole tensor should be used, which comports a large computational cost.

MgO/4-Fe/MgO

We apply the same approach just discussed for $n_{Fe} = 8$ to MgO/4-Fe/MgO thin films. Figure 8.13 presents the angular dependence of the torque for simulations performed with a full tensorial exchange coupling. We fit the data with $\sin(2\vartheta)$ functions and we find that below 200 K the torque has a complex angular dependence that cannot be described by a simple uniaxial model. The competition at the interface with MgO between the on-site and two-sites anisotropies, which are out-of-plane and in-plane respectively, and DMI causes this complex behaviour of the torque at low temperature [60]. As the temperature is increased, the system re-orients out-of-plane and the torque magnitude increases reaching a maximum around 250 K. If the temperature is raised further, we recover the decreasing trend of the torque with temperature. The data and the $\sin(2\vartheta)$ do not show a perfect agreement, likely caused by the complex layer resolved anisotropies. The effect of DMI and antiferromagnetic in-plane interactions weakens as thermal fluctuations increase, as seen with the loss of the spin-spiral state at high temperatures. When we approximate
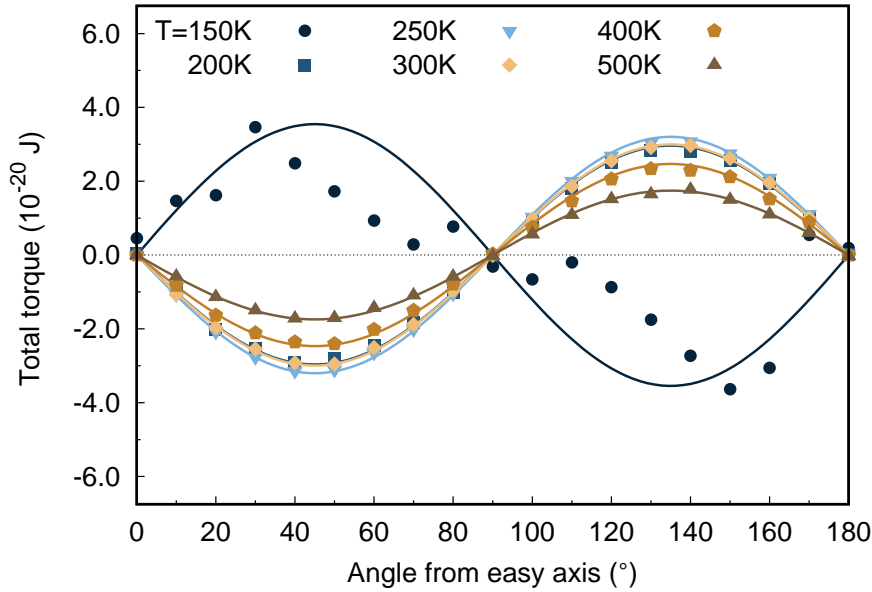
Figure 8.13 Simulated restoring torque in a MgO/4-Fe/MgO thin film. The solid lines are $\sin(2\vartheta)$ fits of the data in the range $[0° : 36°]$.

the exchange coupling with the isotropic or vectorial form, we do not observe any re-orientation of the magnetisation from in-plane to out-of-plane. This lack of re-orientation suggests that DMI plays an important role in determining the magnetic properties of the system at low temperature, in agreement with the analysis of the ground state properties.

We calculate $K_{\mathrm{eff}}(T)$ from the angular dependence of the torque and we plot the results in Figure 8.14 comparing the effect of the exchange coupling normalised with respect to the sum of the on-site and two-sites anisotropies at $T = 0\,\mathrm{K}$, $K_{\mathrm{u}}(0\,\mathrm{K}) = 8.88 \times 10^6\,\mathrm{Jm}^{-3}$. The trend of $K_{\mathrm{eff}}(T)$ is non-monotonic independently of the approximation adopted to describe the exchange. Similarly to what we observe for the $n_{\mathrm{Fe}} = 8$ systems, this is due to the long range of the coupling and the frustration of the spin system. At low temperature the system with full tensorial exchange is characterised by a large in-plane anisotropy. As we do not find such feature in the other two cases, this must be induced by DMI, which can be considered as an anisotropy contribution. Since DMI is oriented in-plane, as shown in Figure 8.5(c), it competes with the on-site anisotropy that is perpendicular to the plane at the Fe/MgO interface Cuadrado *et al.* [60]. $K_{\mathrm{eff}}(T)$ increases and reaches a maximum at about $T = 200\,\mathrm{K}$. This temperature corresponds to the loss of the non-collinear states at the interface. For higher temperatures $K_{\mathrm{eff}}(T)$ decreases and the trend is similar to that exhibited by the system with vectorial exchange. Such an agreement underlines the importance of the two-sites anisotropy in these systems. In this, the system with $n_{\mathrm{Fe}} = 4$ differs from $n_{\mathrm{Fe}} = 8$, where isotropic and vectorial exchange yield similar temperature dependences.
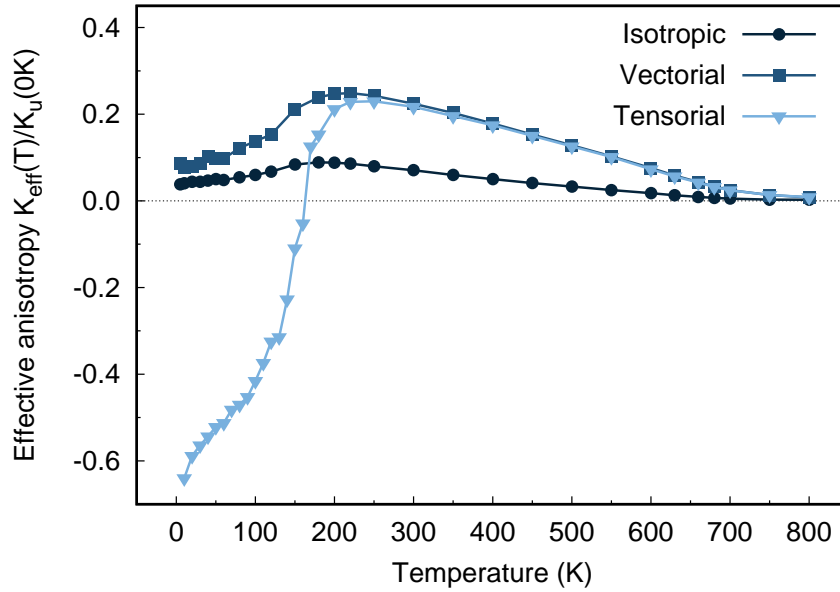
Figure 8.14 Plot of the temperature dependence of the effective anisotropy (K_{eff}) as function of temperature (T) for the n-Fe/MgO system with $n_{\mathrm{Fe}} = 4$. Different colours correspond to simulations performed using different exchange approximations: black dots for isotropic exchange, blue squares for the vectorial approximation and light blue downward triangles for the whole $\bar{\bar{J}}_{ij}$ tensor. All the values of $K_{\mathrm{eff}}(T)$ are normalised to the sum of the on-site and two-sites anisotropies at $T = 0\,\mathrm{K}$, $K_{\mathrm{u}}(0\,\mathrm{K}) = 8.88 \times 10^6\,\mathrm{Jm}^{-3}$, obtained from the sKKR calculations [60]. Lines serve as guide for the eye.

Figure 8.15 shows the comparison of the scaling of $K_{\mathrm{eff}}(T)$ with the total magnetisation of the system between system with different exchange couplings for $n_{\mathrm{Fe}} = 4$. We do not focus on the temperature region $T < 250\,\mathrm{K}$ as the system exhibits complex temperature dependences of both anisotropy and magnetisation. We find a scaling exponent of 2.05 and 2.06 for the systems with tensorial and vectorial exchange, respectively. These values are in good agreement with theoretical predictions for two-ion anisotropy scaling [87]. This suggests that the system behaves as a thin film with two-sites surface anisotropy and almost zero bulk anisotropy. In fact, the two-sites anisotropy is the dominant contribution to the anisotropy in the $n_{\mathrm{Fe}} = 4$ system, and it yields a weaker anisotropy in the interfacial layers due to the competition with the on-site term. Nonetheless, small differences should be expected in the dynamics in this temperature range when DMI is neglected. For systems with isotropic exchange, the absence of two-ion anisotropy comports a larger scaling exponent, closer to what expected for uniaxial anisotropy than in the other cases, as we can see in Figure 8.15. We ascribe the discrepancy from a pure uniaxial anisotropy scaling to the effect of the tetragonalisation of the crystal structure from bcc to bct, which affects the properties of the system even in a simple isotropic case.
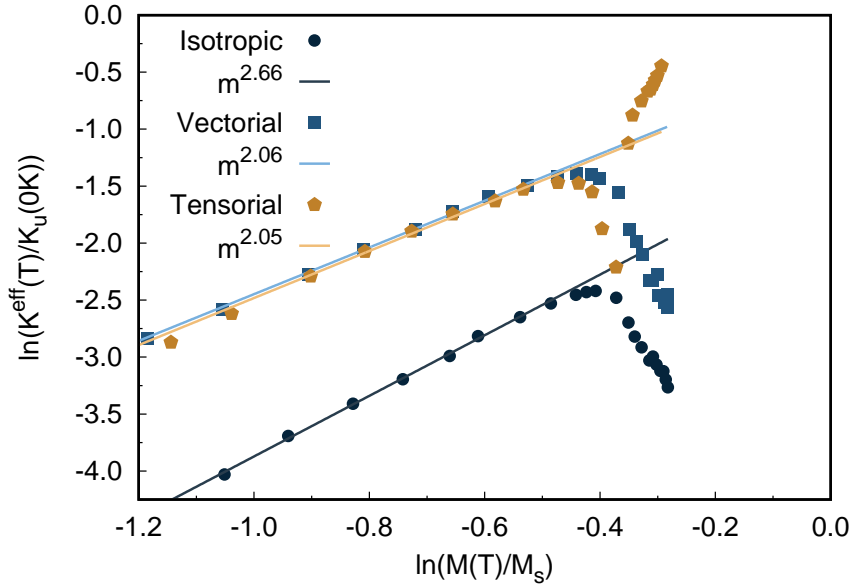
Figure 8.15 Scaling of the effective anisotropy with the total magnetisation for $n_{Fe} = 4$ systems. The symbols represent the data and the solid line the $K_{eff}(T)/K_u(0\,\mathrm{K}) = m^a$ fit in the range $[280\,\mathrm{K}:600\,\mathrm{K}]$, where m is the reduced magnetisation $M(T)/M_s$ and a is obtained from the fit.

8.5 Conclusions

We investigated the magnetic properties in Fe/MgO multilayer systems and their temperature dependence using a multiscale model. In this approach, atomistic resolved parameters obtained from *ab initio* calculations [60] are passed as input parameters for atomistic spin simulations. We find that Fe/MgO thin films are characterised by complex ground-states with non-collinear magnetic surface structures. Such non-collinear configurations arise from the competition between interfacial ferromagnetic and antiferromagnetic interactions and the presence Dzyaloshinskii-Moriya interaction. These are caused by the tetragonal distortion that the MgO induces on the Fe lattice. The resulting temperature dependence of the magnetisation exhibits a complex behaviour with the interface planes that are not fully magnetised. The temperature dependence of the effective anisotropy is non-monotonic and is strongly dependent on the exchange coupling, showing the re-orientation from in-plane to out-of-plane anisotropy in extreme cases. These results suggest that thin Fe/MgO films have more complex magnetic properties than usually assumed, with relevant consequences on the device level. We stress that samples of high purity, degree of crystallinity and control of growth at the atomic level, such as with MBE, are required in order to observe the same properties experimentally. However, such experiments have not been reported yet.

Conclusions

In this final chapter of the thesis, we summarise the results presented previously, highlighting the main conclusions and the most significant results. Finally, we present an outline of future prospects to develop further the work discussed in this thesis.

Calculation of magnetostatic interactions

The magnetostatic interaction plays an important role in multilayer structures such as magnetic tunnel junctions and, as such, an accurate description of this coupling needs to be done to simulate the properties of these systems. Simplifications are necessary to compute this interaction in order to limit the computational cost. This requirement comes from the long range nature of the coupling, which involves all the moments in the system; a widely used approach is the dipole approximation. We implement an improved approach of the bare macro-cell method based on the dipole approximation and previously used in VAMPIRE software package, called inter & intra macro-cells approach. In this approach the system is discretised in regions of uniform magnetisation, macro-cells, and the dipole-dipole field between them is computed accounting for the detail of the atomic positions inside each macro-cell. The technique is based on the work developed by Bowden *et al.* [44] and it allows to obtain agreement with an atomistic dipole-dipole approach for bodies with uniform magnetisation. We perform tests and verify the correctness of the implementation of the approach testing against available analytic results and examples presented by Bowden. We also show that the implemented approach provides higher accuracy than the bare macro-cell model.

Thermally nucleated field-driven switching in CoFeB/MgO systems

We investigate the field-driven dynamics in CoFeB/MgO systems looking at the effects of size and temperature, in particular. Initially, we concentrate on the single CoFeB/MgO layers that constitute the whole magnetic tunnel junction stack. The magnetisation reversal is incoherent for in-plane dimensions larger than the expected single domain size and the switching originates at the edge of the system at temperatures of technological relevance. In fact, the effect of random thermal fluctuations is to promote nucleation

sites favouring non-uniformity in the magnetic texture. The non-coherent nature of the reversal results in a reduction of the coercivity compared with a coherent switching mechanism. In addition to the properties exhibited by the individual ferromagnetic layers, we study the field-driven dynamics in the whole MTJ multilayer structure. The strong magnetostatic interaction between the ferromagnetic layers in the MTJ geometry leads to a stabilising/destabilising effect on the magnetisation of the layers depending on the relative orientation of their magnetisation. This affects the coercive field value and the reversal, since the coupling between the layers can aid or oppose the edge nucleation. We also find that an intrinsic thermal switching field distribution characterises the field-induced switching on the sub-nanosecond time-scale. This distribution is a signature of these systems and limits how accurately the magnetisation reversal can be controlled and needs to be accounted for on the device level. Our results show a complex switching dynamics characterised by non-uniform processes at small dimensions and underline the necessity of modelling such small scale magnetic devices via an atomistic formalism. Finite size effects, interfacial effects and thermal fluctuations can have a dominant effect on physical properties and switching mechanisms of these systems and atomistic models deal with them naturally.

Energy barrier in CoFeB/MgO nanomagnets

In storage and non-volatile memory devices the data need to be safely stored up to a minimum of ten years. The energy barrier is the key parameter that controls the data retention and continuous efforts are under way to improve it. The small finite sizes required for new technological nodes, the presence of surfaces and the necessity to provide stability at operational temperatures make micromagnetic approaches unsuitable. Hence, we characterise the energy barrier in CoFeB/MgO systems using an atomistic spin model. A transition from coherent rotation to domain wall mediated reversal occurs for small lateral dimensions, around the single domain wall size. Nucleation processes are characterised by a reduction in the energy barrier with respect to the macrospin-type coherent reversal, mechanism that is generally assumed to occur in these systems for small dimensions. Close to the transition, the system exhibits mix features and the behaviour cannot be predicted by the available analytic models. Our results show a good agreement with the available analytic models, where possible to compare them, and with experimental measurements of energy barriers. The agreement between simulations and experimental results is obtained using parameters for CoFeB/MgO systems that are independent of the experiments and that the measurements are performed on state of the art devices. As such, our results can provide details about the reversal mechanism and the energy barrier in such MTJs.

Spin transfer torque dynamics in CoFeB/MgO MTJs

In spin transfer torque MRAMs, the writing process is performed exploiting the spin torque effect. Understanding the principles of this phenomenon and how it affects the dynamics of the magnetisation is of great relevance for technological developments. We investigate the magnetisation dynamics induced by a spin polarised current in CoFeB/MgO magnetic tunnel junctions to obtain insights on the nature of the switching mechanism. We model the spin torque following Slonczewski's model and we base our parametrisation on the spin accumulations model of Zhang *et al.*. Our results suggest that the magnetisation reversal is driven by the combination of coherent and non-uniform excitation modes. At low temperature and for small lateral dimensions the reversal is coherent and, as larger sizes are considered, the magnetisation switches non-uniformly. The non-uniform reversal can be driven by a coherent excitation mode where the reversed region is created after the magnetisation exceed a critical angle in the rotation and afterwards it propagates through the system. Alternatively, the switching is initiated by nucleation of a domain at the edge of the system, followed by propagation. In both cases, the out-of-plane reversal is accompanied by the rotation of the in-plane components of the magnetisation. Thermal fluctuations cause a faster reversal and a more complex switching dynamics than at low temperature. Our results suggest a more complex magnetisation dynamics than generally assumed and modelled, hence further studies and more accurate approaches are required to fully understand the spin torque phenomenon. Nonetheless, our results are able to provide useful insights on the spin transfer torque switching dynamics and present comparable features to the experimental measurements on similar systems.

Multiscale atomistic modelling of magnetic properties of Fe/MgO ultrathin films

We use a multiscale model to investigate the magnetic properties of MgO/Fe/MgO thin films. In this approach, atomistic resolved parameters obtained from *ab initio* calculations [60] are passed as input parameters for atomistic spin simulations. The investigated systems are characterised by a long range anisotropic exchange coupling energy with two-sites anisotropy and at the Fe/MgO interface Dzyaloshinskii-Moriya interaction. These electronic properties arise due to the tetragonal distortion of the Fe lattice induced by the MgO. The competition between ferromagnetic and antiferromagnetic exchange interactions and the presence of Dzyaloshinskii-Moriya interactions at the Fe/MgO interface causes the formation of non-collinear spin configurations in the magnetic ground state. The temperature dependence of the magnetisation exhibits a complex behaviour with the Fe planes at the interface with MgO that are not fully magnetised due to the non-collinear magnetic configurations. The temperature dependence of the effective anisotropy is non-monotonic and it is strongly dependent on the exchange coupling,

showing the re-orientation from in-plane to out-of-plane anisotropy in extreme cases. The non-monotonic behaviour is caused by the long range of the exchange interactions and by the presence of in-plane antiferromagnetic coupling at the Fe/MgO interface. Dzyaloshinskii-Moriya interactions and two-ion anisotropy compete with the on-site uniaxial anisotropy and cause deviation from the usually expected uniaxial anisotropy character. Our results suggest that thin Fe/MgO films have more complex magnetic properties than usually assumed for these systems that are common in spintronic applications, with relevant consequences on the device level.

Further work

Further developments to the research presented in this thesis are listed here and discussed in the following text:

1. Further studies to understand the nature of the difference between simulated and measured values of the coercivity.

2. Further study of the temperature and size dependence of the energy barrier.

3. Further investigation of spin transfer torque switching dynamics

4. Application of a multiscale approach to CoFe/MgO systems.

5. Magnetostatic interactions.

In Chapter 5 we presented field-induced magnetisation dynamics of CoFeB/MgO systems. The coercivity values obtained by the simulations are higher than reported in experiments. Reason for the drop in the coercivity can be ascribed to the oxidation of the MgO and consequent formation of FeO_x composites. It is also possible that the magnetic properties of the pristine film are damaged during the fabrication process, resulting in a deterioration of the anisotropy and hence of the coercivity. To progress it is essential to understand the effects that growth, fabrication and production can have on the ideal properties of the system, and modelling can provide a useful tool to support these experimental findings.

We discussed the properties of the energy barrier in CoFeB/MgO nanomagnets in Chapter 6. Due to the high computational cost of the constrained Monte Carlo approach we were limited in the simulations of relatively small dimensions. Such a limitation hinders the investigation of energy barrier for large diameters, where we expect a nucleation regime. Despite this size range is beyond the technological interest ($d < 20$ nm), it is still an open question on a more fundamental level. We aim to compare our results

against the available analytics models, such as the droplet/nucleation theory, to determine if these approaches that have been developed based on micromagnetic description can be applied on a nanoscale level. Moreover, an improvement need to be done in the way magnetostatic effects are included in these models for non-uniform magnetisation states.

Slonczewski's model is the first step in modelling the effect of a spin polarised current on a magnetic system. It is able to provide useful insights on the nature of the magnetisation reversal and on the properties of the switching. Nonetheless, it is characterised by strong assumptions and it is was developed as a micromagnetic approach. To exploit fully the potentiality of atomistic descriptions and to obtain an accurate description of the dynamics of the magnetisation induced when an electrical current is injected into a magnetic tunnel junction, simulations with more advanced and accurate models are required. A suitable candidate is the spin accumulation model. In addition to the spin torque effect, the study of the magnetisation dynamics induced by spin orbit torque (SOT) in similar systems is of great interest, as SOT MRAMs are considered possible candidates to be used as cache memories[1–3].

In the study of the properties of CoFeB/MgO system, CoFeB was modelled assuming a nearest-neighbours isotropic exchange, uniaxial anisotropy and the magnetic moment constant throughout the stack. On the other hand, multiscale simulations of Fe/MgO thin films show that these systems might be more complex than usually assumed, with long range anisotropic exchange interaction, two-ion anisotropy contributions, Dzyaloshinskii-Moriya interactions. Since CoFe and Fe are alike, it is reasonable to assume that CoFe/MgO systems will exhibit similar features. This suggests that the application of an analogous approach to CoFe(B)/MgO structures can help in characterising the magnetic properties of such important systems.

We implemented an accurate approach to calculate the magnetostatic interaction based on the dipole approximation. The major downside of the method is the large computational cost in memory and runtime associated with small cell size discretisation. The implementation of a hierarchical scheme that uses different approaches for different length scales would allow to improve the efficiency and the accuracy of the calculation. One could use an atomistic dipole-dipole calculation in a very short range to capture the effects due to the lattice structure and finite shapes effects. On a larger scale a macro-cell approach can be used, where the correction coming from the atomistic dipole-dipole calculation is added, and for larger distances one could apply a multipole expansion method.

Nomenclature

List of Abbreviations

2D	Two dimensional
AF	Antiferromagnet
AMR	Anisotropic magneto resistance
AST	Adiabatic spin torque
bcc	Body centred cubic
CIP	Current in plane
cMC	Constrained Monte Carlo
CPP	Current perpendicular
CPU	Central processing unit
DFT	Density functional theory
DMI	Dzyaloshinskii-Moriya interaction
DRAM	Dynamic random access memory
fcc	Face centred cubic
FFT	Fast Fourier transform
FL	Free layer in spin valve or magnetic tunnel junction
FM	Ferromagnet
GMR	Giant magneto resistance
HAMR	Heat assisted magnetic recording

KKR	Korringa–Kohn–Rostoker
kMC	Kinetic Monte Carlo
LLG	Landau-Lifshitz-Gilbert
LL	Landau-Lifshitz
MAE	Magnetic anisotropy energy
MC	Monte Carlo
ML	Monolayer
MRAM	Magnetic random access memory
MR	Magneto resistance
MTJ	Magnetic tunnel junction
NAST	Non-adiabatic spin torque
OOMMF	Object Oriented MicroMagnetic Framework software package
PCRAM	Phase change random access memory
PL	Pinned layer in spin valve or magnetic tunnel junction
PMA	Perpendicular magnetic anisotropy
RAM	Random access memory
ReRAM	Resistive random access memory
RHS	Right hand side
RL	Reference layer in a magnetic tunnel junction stack
SAF	Synthetic antiferromagnet
SI	International system
sKKR	Screened Korringa–Kohn–Rostoker
SOT MRAM	Spin orbit torque magnetic random access memory
SRAM	Static random access memory

STT MRAM	Spin transfer torque magnetic random access memory
TDDFT	Time-dependent density functional theory
TMR	Tunnel magneto resistance
TSFD	Thermal switching field distribution
VAMPIRE	VAMPIRE software package
VCMA MRAM	Voltage control magnetic anisotropy magnetic random access memory

List of Symbols

A	Surface area
a	Lattice constant
a_{je}	Adiabatic spin torque parameter
A_s	Exchange stiffness
$\vec{B}$	Magnetic induction
B_{app}	Applied magnetic induction
b_{je}	Non-adiabatic spin torque parameter
χ	Magnetic susceptibility
$\bar{\bar{D}}$	Dipolar tensor
dA	Surface area element
$D(E)$	Density of states
Δ	Stability factor
δ_B	Bloch-wall domain wall width
ΔR	Change in electrical resistance
δ_w	Domain wall width
$\bar{\bar{D}}_{inter}$	Inter dipole matrix
$\bar{\bar{D}}_{intra}$	Intra dipole matrix

e	Electron charge $= 1.602 \times 10^{-19}\,\mathrm{C}$
E_b	Energy barrier
E_a^c	Cubic anisotropy energy
E_dip	Dipolar energy
E_F	Fermi energy
$\hat{e}$	Easy axis direction
ε	Correction factor accounting for spin waves
E_s	Singlet energy
E_t	Triplet energy
E_a^u	Uniaxial anisotropy energy
f	Frequency
f_0	Attempt frequency
$\mathcal{F}$	Free energy
γ	Gyromagnetic factor $= 1.760{,}86 \times 10^{11}\,\mathrm{s^{-1}T^{-1}}$
α	Gilbert damping
$\vec{H}$	Magnetic field
$\mathcal{H}$	Spin Hamiltonian
H_app	Applied magnetic field
H_c	Coercive field
$\vec{H}_\mathrm{dip}$	Dipolar field
$\vec{H}_\mathrm{dip,mc}$	Macro-cell dipolar field
$\mathcal{H}_\mathrm{dmag}$	Magnetostatic energy term in Hamiltonian
$\vec{H}_\mathrm{eff}$	Effective field
H_int	Internal field

$\mathcal{H}_{\mathrm{rad}}$	Spin-independent Hamiltonian
$\mathcal{H}_{\mathrm{spin}}$	Spin-dependent Hamiltonian
I	Electrical current
$\mathbb{1}$	Identity matrix
J	Total angular momentum
j_{e}	Injected current
J_{ex}	Exchange energy constant
J_{ij}	Nearest neighbours exchange integral between site i and j
$\bar{\bar{J}}_{ij}$	Exchange energy tensor
$\bar{\bar{J}}_{ij}^{A}$	Antisymmetric exchange energy tensor
$\bar{\bar{J}}_{ij}^{S}$	Symmetric exchange energy tensor
J_{sd}	*s-d* exchange interaction
k_{B}	Boltzmann constant
K_{c}	Micromagnetic bulk anisotropy energy
K^{c}	Micromagnetic cubic anisotropy energy
k_{c}	Atomistic cubic anisotropy energy constant
K_{eff}	Effective anisotropy energy
K_{i}	Micromagnetic interfacial anisotropy energy
K_{c}	Micromagnetic surface anisotropy energy
K_{u}	Micromagnetic uniaxial anisotropy energy
k_{u}	Atomistic uniaxial anisotropy energy constant
L	Orbital angular momentum
λ_{J}	*s-d* exchange interaction characteristic length
λ_{sdl}	Spin diffusion length

λ_{sf}	Spin flip length
M_{s}	Saturation magnetisation
$\vec{M}$	Magnetisation
m_{e}	Electron mass $= 9.109 \times 10^{-31}\,\mathrm{Kg}$
$\vec{m}_{\mathrm{mc}}$	Macro-cell magnetic moment
m_{ω}	Excitation mode
m_0	Coherent excitation mode
m_1	Vortex excitation mode
m_{-1}	Antivortex excitation mode
$\vec{M}_{\mathrm{p}}$	Direction of spin polarised current
M_{s}	Saturation magnetisation
$\vec{m}$	Spin accumulation
μ	Magnetic moment
μ_0	Permeability of free space $= 4\pi \times 10^{-7}\,\mathrm{T^2 J^{-1} m^3}$
μ_{B}	Bohr magneton $= 9.2740 \times 10^{-24}\,\mathrm{J\,T^{-1}}$
μ_{s}	Magnitude of a spin moment
$N_{\alpha\beta}$	Demagnetisation tensor component $\alpha\beta$
n_{uc}	Number of atoms in the unit cell
n_{mc}	Number of atoms in the macro-cell
P	Contour integral
$\vec{p}_{\mathrm{mc}}$	Position of the centre of a macro-cell
R	Radius
R_{AP}	Electrical resistance of anti-parallel spin configuration
ρ_{M}	Volumetric magnetisation charge density

R_P	Electrical resistance of parallel spin configuration
S	Spin angular momentum
$\vec{S}_i$	Spin vector on site i
σ	Domain wall surface energy density
σ_M	Surface magnetisation charge density
$\vec{\tau}$	Torque
T_c	Curie temperature
U	Coulomb energy
V	Volume
v	Velocity
V_atom	Atomic volume
V_mc	Macro-cell volume
V_uc	Unit cell volume
$\vec{\xi}$	Stochastic field
z	Coordination number
χ_a	Spin component of electronic wave function
Ψ_a	Radial component of electronic wave function

References

[1] A. V. Khvalkovskiy, D. Apalkov, S. Watts, R. Chepulskii, R. S. Beach, A. Ong, X. Tang, A. Driskill-Smith, W. H. Butler, P. B. Visscher, D. Lottis, E. Chen, V. Nikitin, and M. Krounbi, Journal of Physics D: Applied Physics **46**, 139601 (2013).

[2] S. Bhatti, R. Sbiaa, A. Hirohata, H. Ohno, S. Fukami, and S. Piramanayagam, Materials Today **20**, 530 (2017).

[3] B. Dieny, R. B. Goldfarb, and K. J. Lee, in *Introduction to Magnetic Random-Access Memory* (John Wiley & Sons, Inc., 2017).

[4] D. Apalkov, A. Khvalkovskiy, S. Watts, V. Nikitin, X. Tang, D. Lottis, K. Moon, X. Luo, E. Chen, A. Ong, A. Driskill-Smith, and M. Krounbi, J. Emerg. Technol. Comput. Syst. **9** (2013), 10.1145/2463585.2463589.

[5] S. Tehrani, J. M. Slaughter, M. DeHerrera, B. Engel, N. Rizzo, J. Salter, M. Durlam, R. Dave, J. Janesky, B. Butcher, K. Smith, and G. Grynkewich, Proceedings of the IEEE **91**, 703 (2003).

[6] S. Blundell, *Magnetism in condensed matter* (Oxford University Press, 2001).

[7] J. Slaughter, Annual Review of Materials Research **39**, 277 (2009).

[8] W. H. Butler, X.-G. Zhang, T. C. Schulthess, and J. M. MacLaren, Phys. Rev. B **63**, 054416 (2001).

[9] S. M. Thompson, Journal of Physics D: Applied Physics **41**, 093001 (2008).

[10] D. Wang, C. Nordman, J. Daughton, Z. Qian, J. Fink, D. Wang, C. Nordman, J. Daughton, Z. Qian, and J. Fink, IEEE Transactions on Magnetics **40**, 2269 (2004).

[11] S. Bae and N. Thiyagarajah, "Developments in giant magnetoresistance and tunneling magnetoresistance based spintronic devices with perpendicular anisotropy," in *Magnetic Thin Films: Properties, Performance and Applications* (2011) Chap. 4.

[12] J. Mathon and A. Umerski, Phys. Rev. B **63**, 220403 (2001).

[13] X.-G. Zhang and W. H. Butler, Phys. Rev. B **70**, 172407 (2004), 10.1103/PhysRevB.70.172407.

[14] S. Ikeda, J. Hayakawa, Y. M. Lee, F. Matsukura, Y. Ohno, T. Hanyu, and H. Ohno, Electron Devices, IEEE Transactions on **54**, 991 (2007).

[15] S. S. P. Parkin, C. Kaiser, A. Panchula, P. M. Rice, B. Hughes, M. Samant, and S.-H. Yang, Nat Mater **3** (2004).

[16] C. Chappert, A. Fert, and F. N. V. Dau, Nature Materials **6**, 813 (2007).

[17] L. Berger, Phys. Rev. B **54**, 9353 (1996).

[18] J. Slonczewski, J. Magn. Magn. Mater. **159**, L1 (1996).

[19] J. Zabloudil, R. Hammerling, L. Szunyogh, and P. Weinberger, *Springer* (2004).

[20] H. Ebert, D. Ködderitzsch, and J. Minár, Reports on Progress in Physics **74**, 096501 (2011).

[21] O. Eriksson, A. Bergman, L. Bergqvist, and J. Hellsvik, *Atomistic Spin Dynamics: Foundations and Applications* (Oxford University Press, 2017).

[22] R. W. Chantrell, N. Walmsley, J. Gore, and M. Maylin, Phys. Rev. B **63**, 024410 (2000).

[23] "Computer code VAMPIRE 4," (2013).

[24] R. Skomski, *Simple Models of Magnetism* (Oxford University Press, 2008) p. 365.

[25] N. Ashcroft and N. Mermin, *Solid State Physics* (Saunders College, Philadelphia, 1976).

[26] A. Aharoni, *Introduction to the Theory of Ferromagnetism*, International Series of Monogr (Clarendon Press, 2000).

[27] H. Callen and E. Callen, Journal of Physics and Chemistry of Solids **27**, 1271 (1966).

[28] R. E. Rottmayer, S. Batra, D. Buechel, W. A. Challener, J. Hohlfeld, Y. Kubota, L. Li, B. Lu, C. Mihalcea, K. Mountfield, K. Pelhos, C. Peng, T. Rausch, M. A. Seigler, D. Weller, and X. M. Yang, IEEE Transactions on Magnetics **42**, 2417 (2006).

[29] D. A. Garanin, Phys. Rev. B **53**, 11593 (1996).

[30] I. Dzyaloshinsky, Journal of Physics and Chemistry of Solids **4**, 241 (1958).

[31] T. Moriya, Phys. Rev. **120**, 91 (1960).

[32] T. L. Gilbert, IEEE Transactions on Magnetics **40**, 3443 (2004).

[33] L. D. Landau and E. M. Lifshitz, Ukr. J. Phys. **8**, 153 (1935).

[34] M. Fähnle and C. Illg, Journal of Physics: Condensed Matter **23**, 493201 (2011).

[35] W. F. Brown, Phys. Rev. **130**, 1677 (1963).

[36] A. Lyberatos, D. V. Berkov, and R. W. Chantrell, Journal of Physics: Condensed Matter **5**, 8911 (1993).

[37] O. Chubykalo, R. Smirnov-Rueda, J. Gonzalez, M. Wongsam, R. Chantrell, and U. Nowak, Journal of Magnetism and Magnetic Materials **266**, 28 (2003).

[38] J. D. Jackson, *Classical electrodynamics*, 3rd ed. (Wiley, New York, NY, 1999).

[39] "Computer code oommf," .

[40] A. Vansteenkiste, J. Leliaert, M. Dvornik, M. Helsen, F. Garcia-Sanchez, and B. Van Waeyenberge, AIP Advances **4**, 107133 (2014).

[41] A. J. Newell, W. Williams, and D. J. Dunlop, Journal of Geophysical Research **98**, 9551 (1993).

[42] E. Boerner, O. Chubykalo-Fesenko, O. Mryasov, R. Chantrell, and O. Heinonen, IEEE Transactions on Magnetics **41**, 936 (2005).

[43] R. F. L. Evans, W. J. Fan, P. Chureemart, M. O. A. Ellis, T. A. Ostler, and R. W. Chantrell, J. Phys.: Condens. Matter **26**, 103202 (2014).

[44] G. J. Bowden, G. B. G. Stenning, and G. van der Laan, Journal of Physics: Condensed Matter **28**, 066001 (2016).

[45] J. Herbst, Reviews of Modern Physics **63**, 819 (1991).

[46] S. Yuasa, Y. Suzuki, T. Katayama, and K. Ando, Applied Physics Letters **87**, 242503 (2005).

[47] M. Ležaić, P. Mavropoulos, and S. Blügel, Applied Physics Letters **90** (2007), 10.1063/1.2710181.

[48] T. Bose, R. Cuadrado, R. F. L. Evans, R. V. Chepulskii, D. Apalkov, and R. W. Chantrell, Journal of Physics: Condensed Matter **28**, 156003 (2016).

[49] D. Jiles, *Introduction to Magnetism and Magnetic Materials* (1991).

[50] S. Ikeda, K. Miura, H. Yamamoto, K. Mizunuma, H. D. Gan, M. Endo, S. Kanai, J. Hayakawa, F. Matsukura, and H. Ohno, Nature Materials (2010).

[51] A. A. Timopheev, B. M. S. Teixeira, R. C. Sousa, S. Aufret, T. N. Nguyen, L. D. Buda-Prejbeanu, M. Chshiev, N. A. Sobolev, and B. Dieny, Physical Review B **96**, 014412 (2017).

[52] K. Watanabe, B. Jinnai, S. Fukami, H. Sato, and H. Ohno, Nature Communications **9**, 663 (2018), 1712.08774 .

[53] T. Devolder, P.-H. Ducrot, J.-P. Adam, I. Barisic, N. Vernier, J.-V. Kim, B. Ockert, and D. Ravelosona, Applied Physics Letters **102**, 022407 (2013).

[54] S. Kanai, M. Tsujikawa, Y. Miura, M. Shirai, F. Matsukura, and H. Ohno, Applied Physics Letters **105**, 222409 (2014), 10.1063/1.4903296.

[55] S. Peng, M. Wang, H. Yang, L. Zeng, J. Nan, J. Zhou, Y. Zhang, A. Hallal, M. Chshiev, K. L. Wang, Q. Zhang, and W. Zhao, Sci. Rep. **5**, 18173 (2015).

[56] S. Yuasa and D. D. Djayaprawira, Journal of Physics D: Applied Physics **40**, R337 (2007).

[57] Y. S. Choi, K. Tsunekawa, Y. Nagamine, and D. Djayaprawira, Journal of Applied Physics **101**, 013907 (2007), 10.1063/1.2407270.

[58] A. A. Timopheev, R. Sousa, M. Chshiev, T. Nguyen, and B. Dieny, Scientific Reports **6**, 26877 (2016).

[59] H. Sato, P. Chureemart, F. Matsukura, R. W. Chantrell, H. Ohno, and R. F. L. Evans, "Temperature dependent properties of cofeb/mgo thin films: experiments versus simulations (submitted)," (2018).

[60] R. Cuadrado, L. Oroszlány, A. Deák, T. A. Ostler, A. Meo, R. V. Chepulskii, D. Apalkov, R. F. L. Evans, L. Szunyogh, and R. W. Chantrell, Phys. Rev. Applied **9**, 054048 (2018).

[61] H. X. Yang, M. Chshiev, B. Dieny, J. H. Lee, A. Manchon, and K. H. Shin, Phys. Rev. B **84**, 054401 (2011).

[62] I. Turek, S. Blugel, G. Bihlmayer, and P. Weinberger, Czechoslovak Journal of Physics **53**, 81 (2003).

[63] Y. Takeuchi, H. Sato, S. Fukami, F. Matsukura, and H. Ohno, Applied Physics Letters **107**, 152405 (2015), 10.1063/1.4933256.

[64] M.-S. Jeon, K.-S. Chae, D.-Y. Lee, Y. Takemura, S.-E. Lee, T.-H. Shim, and J.-G. Park, Nanoscale **7**, 8142 (2015).

[65] V. B. Naik, H. Meng, and R. Sbiaa, AIP Advances **2**, 042182 (2012), 10.1063/1.4771996.

[66] J. Zhang, C. Franz, M. Czerner, and C. Heiliger, Phys. Rev. B **90**, 184409 (2014).

[67] J. Sinha, M. Hayashi, A. J. Kellock, S. Fukami, M. Yamanouchi, H. Sato, S. Ikeda, S. Mitani, S.-h. Yang, S. S. P. Parkin, and H. Ohno, Applied Physics Letters **102**, 242405 (2013), 10.1063/1.4811269.

[68] A. Kaidatzis, C. Bran, V. Psycharis, M. Vázquez, J. M. García-Martín, and D. Niarchos, Applied Physics Letters **106**, 262401 (2015), 10.1063/1.4923272.

[69] A. Meo, P. Chureemart, S. Wang, R. Chepulskyy, D. Apalkov, R. W. Chantrell, and R. F. L. Evans, Scientific Reports **7**, 16729 (2017).

[70] E. C. Stoner and E. P. Wohlfarth, Philosophical Transactions of the Royal Society A: Mathematical, Physical and Engineering Sciences **240**, 599 (1948).

[71] H. Sato, E. C. I. Enobio, M. Yamanouchi, S. Ikeda, S. Fukami, S. Kanai, F. Matsukura, and H. Ohno, Applied Physics Letters **105**, 062403 (2014), 10.1063/1.4892924.

[72] H. Sato, M. Yamanouchi, K. Miura, S. Ikeda, R. Koizumi, F. Matsukura, and H. Ohno, Magnetics Letters, IEEE **3**, 3000204 (2012).

[73] P. H. Jang, K. Song, S. J. Lee, S. W. Lee, and K. J. Lee, Appl. Phys. Lett. **107** (2015), 10.1063/1.4936089.

[74] J. Sampaio, A. V. Khvalkovskiy, M. Kuteifan, M. Cubukcu, D. Apalkov, V. Lomakin, V. Cros, and N. Reyren, Applied Physics Letters **108**, 112403 (2016).

[75] K. Song and K. J. Lee, J. Appl. Phys. **118**, 10 (2015).

[76] M. P. Sharrock, Journal of Applied Physics **76**, 6413 (1994).

[77] S. K. Piotrowski, M. Bapna, S. D. Oberdick, S. A. Majetich, M. Li, C. L. Chien, R. Ahmed, and R. H. Victora, Phys. Rev. B **94**, 014404 (2016).

[78] L. Breth, D. Suess, C. Vogler, B. Bergmair, M. Fuger, R. Heer, and H. Brueckl, Journal of Applied Physics **112**, 023903 (2012), 10.1063/1.4737413.

[79] J. Kurkijärvi, Physical Review B **6**, 832 (1972).

[80] H. Sato, M. Yamanouchi, K. Miura, S. Ikeda, H. D. Gan, K. Mizunuma, R. Koizumi, F. Matsukura, and H. Ohno, Applied Physics Letters **99**, 042501 (2011), 10.1063/1.3617429.

[81] J. Z. Sun, S. L. Brown, W. Chen, E. A. Delenia, M. C. Gaidis, J. Harms, G. Hu, X. Jiang, R. Kilaru, W. Kula, G. Lauer, L. Q. Liu, S. Murthy, J. Nowak, E. J. O'Sullivan, S. S. P. Parkin, R. P. Robertazzi, P. M. Rice, G. Sandhu, T. Topuria, and D. C. Worledge, Physical Review B **88**, 104426 (2013).

[82] M. Gajek, J. J. Nowak, J. Z. Sun, P. L. Trouilloud, E. J. O'Sullivan, D. W. Abraham, M. C. Gaidis, G. Hu, S. Brown, Y. Zhu, R. P. Robertazzi, W. J. Gallagher, and D. C. Worledge, Applied Physics Letters **100**, 132408 (2012).

[83] E. C. I. Enobio, M. Bersweiler, H. Sato, S. Fukami, and H. Ohno, Japanese Journal of Applied Physics **57**, 04FN08 (2018).

[84] K. Munira and P. B. Visscher, Journal of Applied Physics **117**, 17B710 (2015), 10.1063/1.4908153.

[85] G. D. Chaves-O'Flynn, E. Vanden-Eijnden, D. L. Stein, and A. D. Kent, Journal of Applied Physics **113**, 023912 (2013).

[86] G. D. Chaves-O'Flynn, G. Wolf, J. Z. Sun, and A. D. Kent, Phys. Rev. Applied **4**, 024010 (2015).

[87] P. Asselin, R. F. L. Evans, J. Barker, R. W. Chantrell, R. Yanes, O. Chubykalo-Fesenko, D. Hinzke, and U. Nowak, Phys. Rev. B **82**, 054415 (2010).

[88] Hubert Alex and R. Schäfer, *Magnetic Domains: The Analysis of Magnetic Microstructures*, Vol. 40 (1998) p. 109.

[89] E. Liu, J. Swerts, Y. C. Y. Wu, A. Vaysset, S. Couet, S. Mertens, S. Rao, W. Kim, S. Van Elshocht, J. De Boeck, and G. G. S. Kar, IEEE Transactions on Magnetics , 1 (2018).

[90] D. Hinzke and U. Nowak, Physical Review B **58**, 265 (1998).

[91] D. Hinzke and U. Nowak, Computer Physics Communications **121-122**, 334 (1999).

[92] U. Nowak and D. Hinzke, Journal of Applied Physics **85**, 4337 (1999).

[93] S. Zhang, P. M. Levy, and A. Fert, Phys Rev Lett **88**, 236601 (2002).

[94] D. Ralph and M. Stiles, Journal of Magnetism and Magnetic Materials **320**, 1190 (2008).

[95] P. M. Levy, Journal of Physics D: Applied Physics **35**, 2448 (2002).

[96] Z. Li and S. Zhang, Physical Review B **68**, 024404 (2003).

[97] P. Chureemart, I. D'Amico, and R. W. Chantrell, Journal of Physics C **27**, 146004 (2015).

[98] S. Zhang and Z. Li, Physical Review Letters **93**, 127204 (2004).

[99] C. Burrowes, A. P. Mihai, D. Ravelosona, J.-V. Kim, C. Chappert, L. Vila, A. Marty, Y. Samson, F. Garcia-Sanchez, L. D. Buda-Prejbeanu, I. Tudosa, E. E. Fullerton, and J.-P. Attané, Nature Physics **6**, 17 (2010).

[100] A. Slavin and V. Tiberkevich, IEEE Transactions on Magnetics **45**, 1875 (2009).

[101] T. Taniguchi, S. Yakata, H. Imamura, and Y. Ando, Applied Physics Express **1**, 031302 (2008).

[102] P. B. Visscher, K. Munira, and R. J. Rosati, Arxiv. Cond-Mat , 3 (2016), arXiv:1604.03992 .

[103] P. Chureemart, *Models of spin torque using self-consistent solutions of the magnetisation and spin accumulation*, Ph.D. thesis, University of York (2013).

[104] V. V. Naletov, G. de Loubens, G. Albuquerque, S. Borlenghi, V. Cros, G. Faini, J. Grollier, H. Hurdequint, N. Locatelli, B. Pigeau, A. N. Slavin, V. S. Tiberkevich, C. Ulysse, T. Valet, and O. Klein, Physical Review B **84**, 224423 (2011).

[105] C. Hahn, G. Wolf, B. Kardasz, S. Watts, M. Pinarbasi, and A. D. Kent, Physical Review B **94**, 214432 (2016), 1610.09710 .

[106] T. Devolder, J.-V. Kim, F. Garcia-Sanchez, J. Swerts, W. Kim, S. Couet, G. Kar, and A. Furnemont, Phys. Rev. B **93**, 024420 (2016).

[107] T. Devolder, A. Le Goff, and V. Nikitin, Phys. Rev. B **93**, 224432 (2016).

[108] L. Szunyogh, B. Újfalussy, and P. Weinberger, Phys. Rev. B **51**, 9552 (1995).

[109] J. M. Soler, E. Artacho, J. D. Gale, A. García, J. Junquera, P. Ordejón, and D. Sánchez-Portal, Journal of Physics: Condensed Matter **14**, 2745 (2002).

[110] B. Y. Yavorsky and I. Mertig, Phys. Rev. B **74**, 1 (2006).

[111] L. Rózsa, U. Atxitia, and U. Nowak, Physical Review B **96**, 094436 (2017).